SAPIENZA
UNIVERSITÀ DI ROMA

Numerical Analysis of Radiative Heat Transfer in Rocket Engines

Department of Mechanical and Aerospace Engineering
PhD in Aeronautical and Space Engineering (XXXVIII cycle)

Marco Fabiani
ID number 1755311

Advisor
Prof. Francesco Nasuti

Co-Advisors
Prof. Daniele Bianchi
Dr. Mario Tindaro Migliorino

Academic Year 2024/2025

Thesis defended on 27^{th} January 2026
in front of a Board of Examiners composed by:

Prof. Maurizio Quadrio (chairman)
Prof. Emanuele De Angelis
Prof. Piergluigi Di Lizia

Reviewers:

Prof. Vigor Yang
Prof. Toru Shimada

Numerical Analysis of Radiative Heat Transfer in Rocket Engines
PhD thesis. Sapienza University of Rome

This thesis has been typeset by LaTeX and the Sapthesis class.

Author's email: m.fabiani@uniroma1.it

Per essere creduto non bisogna dire che le menzogne necessarie.
Italo Svevo, La Coscienza di Zeno

Abstract

Thermal radiation represents a fundamental, yet often underestimated or miss-modeled, mode of heat transfer in rocket engines. The extreme thermodynamic conditions encountered in combustion chambers—characterized by high temperatures, pressures, and the presence of radiatively active species and particles—make radiative effects potentially comparable to convective heat fluxes. However, the lack of models validated for rocket engine environments has limited their inclusion in predictive simulations. This thesis addresses this gap through a comprehensive numerical analysis of radiative heat transfer across liquid, hybrid, and solid rockets.

A general framework for radiation modeling was developed, solving the radiative heat transfer equation in absorbing, emitting, and scattering medium with the discrete transfer method. Several spectral and global approaches for gaseous radiative species have been implemented, along with dedicated models for particulate radiation. The solver was coupled to CFD simulations of reactive, turbulent, compressible flows for different propulsion systems.

For liquid rocket engines, the analysis compared several gas radiation models for oxygen–hydrogen and oxygen–methane propellant combinations under chamber conditions up to 100 bar. The results showed the need for radiation models specifically tailored for LRE conditions. Reduced-order WSGG models were developed and validated, offering substantial computational savings while maintaining good accuracy with respect to detailed spectral methods.

For hybrid rocket engines, a detailed investigation of gas and soot radiation was carried out in an oxygen–HTPB motor. Simulations revealed that soot emission can represent a major fraction of the radiative heat flux and significantly affect the fuel regression rate, improving the agreement with experimental data.

For solid rocket motors, radiation from alumina particles was modeled, accounting for absorption, emission, and scattering effects. Results highlighted that scattering anisotropy and particle size distribution strongly influence the wall heat flux, which can locally exceed the convective contribution in the nozzle throat.

Overall, this work bridges the gap between radiative transfer modeling and rocket engine analysis, providing validated tools and physical insight into the role of radiation in propulsion system design.

Contents

List of Figures

List of Tables

Nomenclature

Symbols

$\dot{m}$	mass flow rate, kg/s
$\dot{r}$	fuel regression rate, mm/s
$\hat{\mathbf{n}}$	normal versor
$\hat{\mathbf{s}}$	ray versor
$\mathbf{r}$	position vector
$\mathcal{I}$	radiative intensity
$\mathcal{M}$	molar mass, kg/kmol
c^*	characteristic velocity, m/s
c_p	specific heat at constant pressure, J/(kg·K)
D	diameter, m
f_v	soot volume fraction
G	mass flux, kg/(m^{2}s)
h	enthalpy per unit mass, J/kg
L	length, m
N_p	particle number density, 1/m^3
OF	oxidizer to fuel ratio
p	pressure, Pa
q	heat flux, W/m^2
r	radius, m
s	abscissa along ray, m
T	temperature, K
v	volume, m^3
x	molar fraction/axial coordinate, m
y	mass fraction
Pr	Prandtl number

Constants

σ	Stefan Boltzmann constant, 5.67×10^{-8} W·m^{-2}·K^{-4}
c	Speed of light, 299 792 458 m/s
h	Planck constant, $6.626{\times}10^{-34}$ m^{2}kg/s
k_B	Boltzmann constant, $1.38{\times}10^{-23}$ m^{2}kg/(s^{2}K)

Greek

μ	dynamic viscosity, Pa·s
ρ	density, kg/m^3
τ	transmissivity
ε	surface emissivity

Subscripts

abs	absorption
ad	adiabatic
b	black-body
c	chamber
ox	oxidizer
sca	scattering

Chapter 1

Introduction

Contents

Rocket propulsion has become a relatively mature field in the last few decades [1, 2]. The development of propulsion systems is becoming routine and the cost of new ones is going down, driven by the recent boom of private launcher companies [3]. While most engines currently being developed are based on concept already proven (or at least imagined) decades ago, the unique challenges posed by the high chamber pressure and temperature, together with the need for a lightweight structure, continue to make their design a complex task. Moreover, the increased competitiveness of the launch market and the shift towards reusable engines determine much stricter design requirements. There is therefore a need for the development of comprehensive and predictive modeling tools [4].

Among the challenges faced by the propulsion engineer there is the one of heat transfer. While the combustion gases flow loses to the engine walls only a low percentage of its energy, the power generated by a rocket [1] is so large that even a small fraction is enough to melt or damage the structure. A correct evaluation of the wall heat flux not only allows to avoid an engine RUD (rapid unexpected disassembly) when first tested, but also to design for durability and re-usability, which are key factors in the design of modern liquid propellant engines. Heat transfer inside a rocket is due first and foremost to convection, and several investigations, both numerical and experimental, have been performed to provide tools for its evaluation [5, 6]. However, thermal radiation can be a relevant contribution. In fact,

[1] The power of the jet of the F1 rocket engine (Saturn V first stage) was approximately 8 GW, the rated capacity of the largest electrical plant currently in operation, the three gorges dam in China, is 22.5 GW.

the heat flux emitted by a black body (i.e. a perfect emitter and absorber) can be expressed as

$$q = \sigma T^4$$

where σ is the Stefan-Boltzmann constant. For a typical rocket engine, which has chamber temperatures in the order of 3500 K, this leads to a maximum heat flux of ≈ 8.5 MW/m^2. The high chamber pressure, resulting in high gas density, and the possible presence of particles can result in a combustion products behaviour close to black-body conditions.

Thermal radiation is, however, a complex phenomenon (with an even more complex mathematical description)[2]. Its complexity is due to the fact that radiation is a) directional and b) generally long-range [7]. Thus, conservation of energy cannot be applied over an infinitesimal volume, but must be applied over the entire volume under consideration. This leads to an integral equation in up to seven independent variables (the frequency of radiation, three space coordinates, two coordinates describing the direction of travel of photons, and time). Moreover, radiative properties are usually difficult to measure and often display erratic behavior [8]. For solid materials those normally depend only on a very thin surface layer, which may vary strongly with surface properties and operative conditions. All radiative properties (in particular for gases) may vary strongly with wavelength, adding another independent variable to the governing equation and requiring very fine spectral discretizations, further increasing the computational burden.

For these reasons, and due to the fact that radiation is only one of the many sub-models needed in the simulation of rocket combustion chamber [9], there is a lack of radiation models specifically validated for the high temperature and pressures typical of rocket engines. This thesis aims to provide a comprehensive assessment of the effect of radiation heat transfer in chemical rocket engines, bridging the gap between radiative modeling and rocket engine analysis and design.

This introductory chapter is is organized as follows: Sec. 1.1 briefly presents the issue of heat transfer in rocket engines, Sec. 1.2 introduces the main concepts of thermal radiation and Sec. 1.3 presents the state of the art for what concerns the modeling of thermal radiation in rocket engine thrust chambers.

1.1 Heat transfer in rocket engines

The thrust chambers of rocket engines operate under extremely harsh thermal and mechanical conditions, primarily due to the high temperature and pressure of the combustion gases. These conditions impose stringent design constraints, and to ensure structural integrity and durability cooling systems are required (either active or passive). Predictive modeling of the heat transfer rates to the combustor walls is necessary for an effective design of such systems. Depending on the type of rocket engine, different thermal protection strategies may be possible, which are briefly reviewed in this section.

[2] and an annoying tendency to lack experimental data in rocket engine conditions

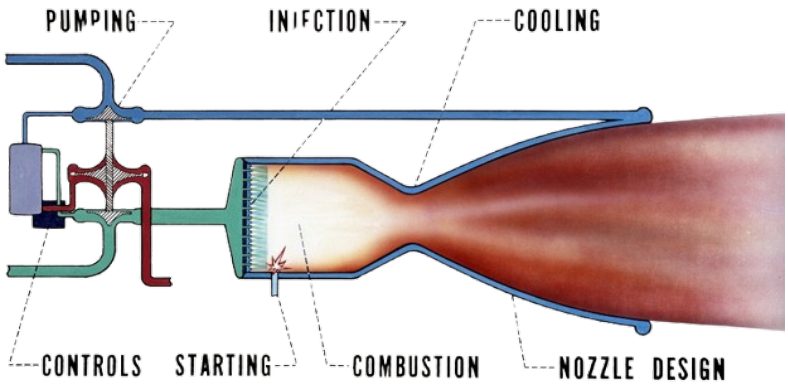

Figure 1.1. Schematic of a liquid rocket engine. Credit: Glenn Research Center, NASA.

Liquid rocket engines

Liquid rocket engines typically employ regenerative cooling, achieved by circulating the fuel through channels integrated into the thrust chamber walls (Fig. 1.1). The system simultaneously provides wall protection and preheats the propellant. The accurate prediction of heat transfer on the hot-gas side is therefore a critical aspect of engine design. It determines the maximum wall temperature and local heat flux and provides the necessary input for evaluating coolant pressure drop, temperature rise, and overall thermal management. The convective heat flux is proportional to the local mass flux, and the heat transfer coefficient may be estimated through the well-known Bartz equation [10]

$$h = \frac{0.026}{D^{0.2}} \left(\frac{c_p \mu^{0.2}}{\mathrm{Pr}^{0.6}} \right) \left(\frac{\dot{m}}{A} \right)^{0.8} \left(\frac{\rho_{am}}{\rho'} \right) \left(\frac{\mu_{am}}{\mu_0} \right)$$

which shows how the thermal loads are maximum at the throat, where the cross-section A is minimum (the subscript 0 refers to stagnation conditions, am to the arithmetic mean temperature between free-stream ($'$) and wall). The radiative heat flux is instead related to the temperature, and is thus expected to be maximum in the cylindrical part of the chamber. A in-depth analysis of radiation heat transfer in LREs is presented in Chapt. 5. Considering the increasing adoption of reusable LREs [11], it is worth recalling that a correct estimation of the heat flux is essential not only for ensuring safe operation, but also to perform a correct estimation of the engine lifetime, mainly related to the thermo-mechanical loads.

Solid rocket motors

Because solid rocket motors (Fig. 1.2) do not employ liquid or gaseous propellants, regenerative cooling is not a viable option; instead, thermal protection relies on ablative systems that sacrifice material to withstand extreme heat loads. Typical ablative materials include graphite, carbon–carbon, and carbon/phenolic composites, chosen for their high thermal resistance and ability to dissipate heat through

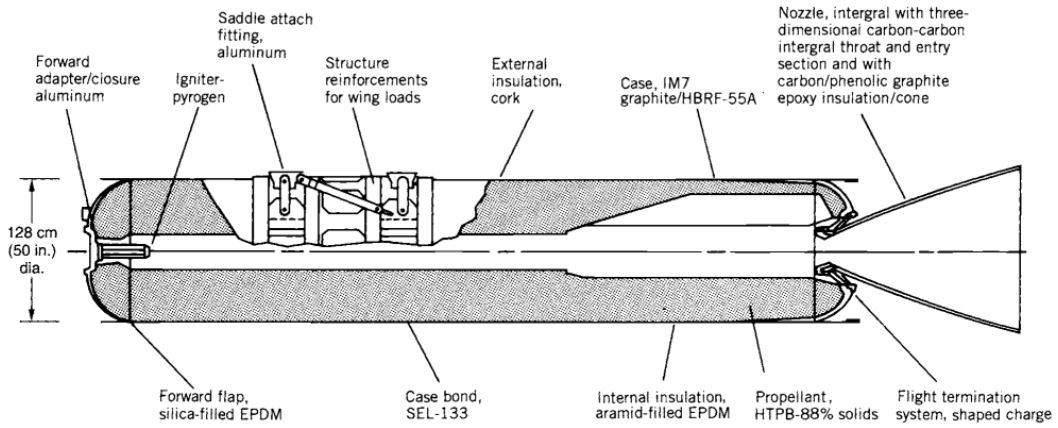

Figure 1.2. Schematic of a solid rocket motor. Image taken from [1].

controlled degradation [12]. However, the severe thermo-mechanical environment inside SRMs—dominated by hot combustion gases laden with alumina particles [13]—makes nozzle erosion an unavoidable challenge. At the high surface temperatures reached during firing, heterogeneous reactions occur between the nozzle material and oxidizing species such as H_2O, OH, and CO_2, leading to chemical erosion [14]. This process causes progressive material recession, most critically at the nozzle throat where heat fluxes are maximized. The enlargement of the throat area reduces chamber pressure and specific impulse, ultimately degrading motor performance over time. For this reason, accurate prediction of heat transfer and its coupling with material response is of central importance in SRM design and reliability. Moreover, accurate prediction of the temperature distribution not only of the ablator surface, but of all nozzle components is a key factor to ensure a correct operation.

Hybrid rocket engines

Hybrid rocket engines (HREs) are propulsion devices employing a solid fuel and a gaseous/liquid oxidizer (Fig. 1.3). The fuel regression rate, which determines the engine's mass flow rate and mixture ratio, is determined by the heat flux to the grain surface

$$\rho_{\text{fuel}}\dot{r} = q_{\text{convective}} + q_{\text{radiative}}$$

which comes from the diffusion flame typical of these engines [16]. A correct determination of the heat loads is thus not only necessary to assess the engine survivability (as in LREs and SRMs), but also to predict thrust and specific impulse. This modeling complexity, together with the typically low regression rates and combustion efficiencies[3], is one of the reasons why HREs have still not flown in orbital flights, although significant steps are being made in that direction. HREs typically employ ablative thermal protection systems as SRMs, although recent

[3]at least without any regression rate and mixing enhancing techniques, such as swirl injection or grain steps [17]

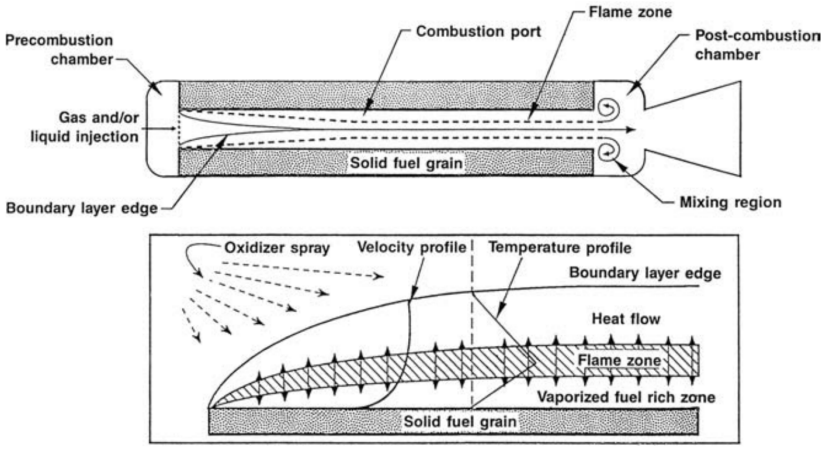

Figure 1.3. Schematic of an hybrid rocket engine. Taken from [15].

works have underlined the potential of regenerative cooling [18].

1.2 Basics of thermal radiation

This section presents the basic concepts of thermal radiation. For a more complete assessment of the topic, the reader is referred to [7].

Thermal radiation is the transfer of energy by electromagnetic waves (or photons), which are emitted by all matter at a temperature above absolute zero. The radiation emitted by a body depends on its temperature and on its emissive properties, which in turn depend on the chemical composition and physical state of the material. The radiation emitted by a black body, i.e. an idealized body that absorbs all incident radiation, is given by Planck's law (Fig. 1.4):

$$\mathcal{I}_{\lambda,b}(T) = \frac{2hc^2}{\lambda^5} \frac{1}{e^{\frac{hc}{n\lambda k_B T}} - 1} \tag{1.1}$$

where h is Planck's constant, c is the speed of light, k_B is Boltzmann's constant, and n is the refractive index (equal to 1 for vacuum and most gases).

A real body, be it a solid surface or a gaseous medium, does not usually behave as a black body, but is characterized by an emissivity ε_λ, such that

$$\mathcal{I}_\lambda(T) = \varepsilon_\lambda \mathcal{I}_{\lambda,b}(T) \tag{1.2}$$

The same reasoning can be applied to the total emissive power (i.e. the spectral intensity integrated over all wavelengths and angles), which is given by:

$$E(T) = \varepsilon E_b(T), \quad E_b(T) = \pi \int_0^\infty I_{\lambda,b}(T) d\lambda = \sigma T^4 \tag{1.3}$$

The "total" emissivity ε is often called the Planck-mean emissivity, being computed as

$$\varepsilon = \frac{\int_0^\infty \varepsilon_\lambda I_{\lambda,b}(T) d\lambda}{\int_0^\infty I_{\lambda,b}(T) d\lambda} \tag{1.4}$$

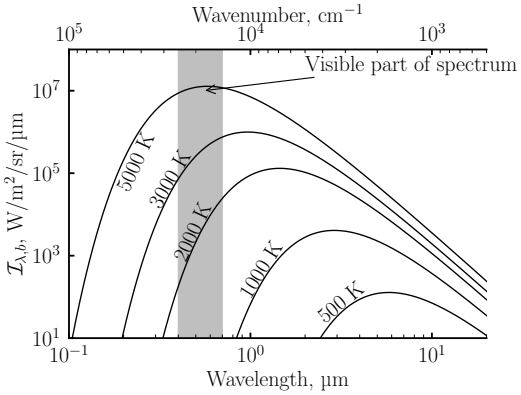

Figure 1.4. Planck function.

namely with an integral over the spectrum weighted with the Planck function.

As shown in Eq. (1.1), the radiation emitted by a black body is a spectral quantity, i.e. it depends on a spectral variable (such as frequency, wavelength, or wavenumber). In radiation heat transfer it is custom to use either the wavenumber η, measured in cm^{-1}, or the wavelength λ, measured in μm. All spectral variables are related one to each other by the following:

$$\eta = \frac{1}{\lambda} = \frac{\nu}{c}, \quad \nu = c\eta = \frac{c}{\lambda} \tag{1.5}$$

Radiation is a directional quantity, being representative of the energy carried by waves/photons traveling in a certain direction. Such propagation vector is usually referred to as a "ray" or line of sight $\hat{\mathbf{s}}$. Along a given ray the spectral radiative intensity $\mathcal{I}_\lambda$, which is the energy flow per unit solid angle and area normal to the ray, varies due to absorption, emission, and scattering. A medium may, in fact, absorb a photon, emit a new one, or change its direction (scattering). The evolution of $\mathcal{I}$ along a line of sight is described by the radiative heat transfer equation

$$\nabla\mathcal{I}_\eta \cdot \hat{\mathbf{s}} = \frac{d\mathcal{I}_\eta}{ds} = \kappa_{\eta,\text{abs}}\mathcal{I}_{\eta,b} - \kappa_{\eta,\text{sca}}\mathcal{I}_{\eta,b} + \frac{\kappa_{\eta,\text{sca}}}{4\pi}\int_{4\pi}\mathcal{I}_\eta(\hat{\mathbf{s}}_i)\Phi_\eta(\hat{\mathbf{s}}_i,\hat{\mathbf{s}})d\Omega_i \tag{1.6}$$

where $\kappa_{\eta,\text{abs}}$ is the absorption coefficient, $\kappa_{\eta,\text{sca}}$ the scattering coefficient, and Φ_η is the scattering function. The first quantifies the probability of a photon to be absorbed or emitted (the two are equal if the medium is a local thermodynamic equilibrium), the second is related to the strength of the scattering phenomenon, while the latter indicates the probability of a photon to be scattered in a given direction.

The formal solution to Eq. (1.6) for a non-scattering medium is

$$\mathcal{I}_\eta(s) = \mathcal{I}_\eta(0)e^{-\tau_\eta} + \int_0^{\tau_\eta}\mathcal{I}_{\eta,b}(\tau_\eta')e^{-(\tau_\eta-\tau_\eta')}d\tau_\eta', \quad \tau_\eta = \int_0^s \kappa_{\eta,\text{abs}}ds \tag{1.7}$$

which is an integro-differential equation in 6 variables (three spatial coordinates, two angular coordinates, and one spectral variables)[4]. Equation (1.7) also points

[4]Since the speed of light is much larger than gas-dynamics velocities, radiation can be considered as steady in the present work, and the dependence from time is not included.

out how radiation is a long-range phenomenon, meaning that the wall heat flux

$$q_\eta = \varepsilon_{\eta,\text{wall}} \left(\int_{4\pi} \mathcal{I}_\eta(\hat{\mathbf{s}}) \hat{\mathbf{n}} \cdot \hat{\mathbf{s}} d\Omega - \mathcal{I}_{\eta,b}(T_\text{wall}) \right) \tag{1.8}$$

may be influenced even by flowfield regions far from the wall. In the above equation, $\varepsilon_{\eta,\text{wall}}$ is the surface emissivity (or emittance) of the wall, which is a spectral and directional quantity. As shown in Fig. 1.5, depending on the material characteristics, surfaces may behave as gray (constant emissivity along the spectrum) or as non-gray, but also as diffuse (no variation of ε with the direction of radiation) or as non-diffuse.

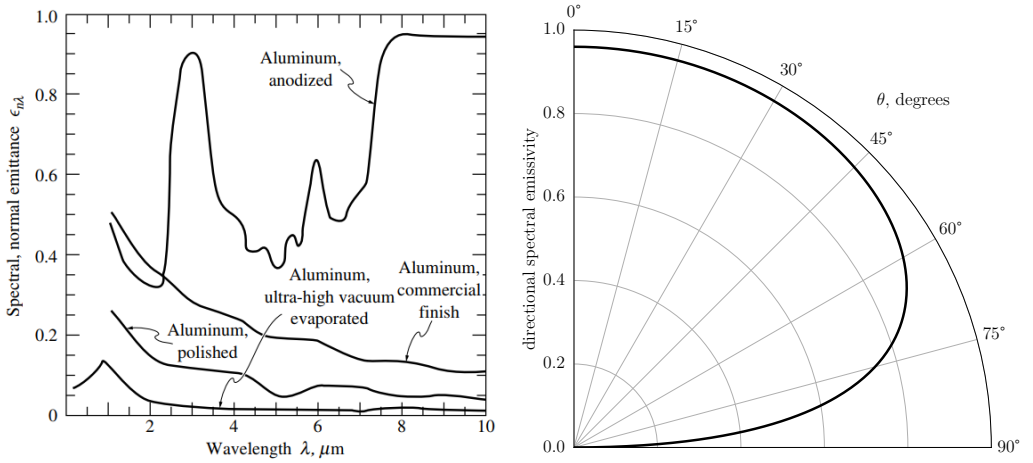

(a) Spectral normal emissivity of Aluminum, taken from [7].

(b) Directional emissivity of a dielectric material.

Figure 1.5. Variation of wall emissivity with wavelength and direction of incident radiation.

The main challenges in solving the RTE come from the spectral dependence of the absorption and scattering coefficients. In fact, emission and absorption of photons by gas molecules result in the change of the molecule energy level. Since by quantum mechanics the energy levels are discrete, molecules can emit photons only with specific intensity, namely at specific frequencies. For the temperature ranges typical of rocket combustion, the energy levels that are most active correspond to changes in the vibrational and rotational states of the molecule. Molecules have however up to tens of millions of possible transitions, resulting in emission spectra that are extremely complex. As an example, Figure 1.6 reports the absorption spectra of the combustion products of oxygen and methane. Each of the peaks in the spectrum is called a "line" and corresponds to a roto-vibrational transition of the molecule. Taking into account the complete spectrum, through so-called "line-by-line" calculations, requires an extremely fine spectral grid and has a large computational cost. To overcome this limitation several reduced-order approaches have been developed, ranging from narrow-band models (spectral approaches with coarser resolution than line by line) to global models (such as the weighted sum of gray gases) which aim to predict a correct total emissivity, but are unable to yield any information on the spectrum. A more detailed discussion of such models is presented in Chapt. 3.

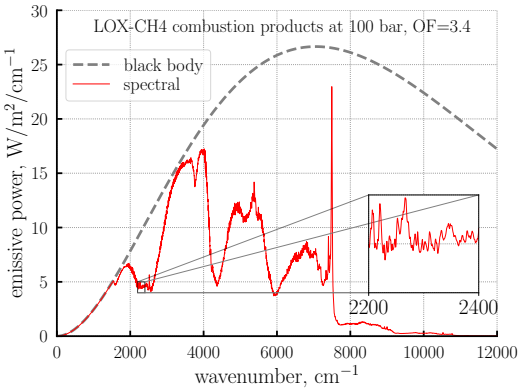

Figure 1.6. Emission spectrum for LOX-LCH4 combustion products.

1.3 Overview of thermal radiation modeling in rocket engines

In this section a review of the state of the art is presented, in order to identify the main challenges in radiation modeling for each of the engines under consideration.

1.3.1 Liquid rocket engines

Radiation heat transfer in liquid rocket engines has been the object of many numerical studies, which have quantified it to account for 2-10% of the total heating power and up to 30% of total heat heat flux in the cylindrical part of the chamber [19]. However, the lack of experimental radiation data and the lack of gas radiation models specifically validated for LRE conditions[5] has lead to a significant scattering between the results presented by various authors. As an example, Fig. 1.7 reports the radiative wall heat fluxes computed by several authors [21–24] for the space shuttle main engine (SSME), which is by far the most studied LRE from the radiation heat transfer standpoint. It can be seen how the predicted peak heat flux ranges from 4 MW/m^2 to approximately 7 MW/m^2, and that also the heat flux profile along the combustion chamber is significantly scattered among the references. Some of the differences among the reported data may be due to the different values of wall emissivity, to the algorithms employed for the integration of the radiative heat transfer equation, to the gas temperature flowfield employed for the radiative calculation, and mostly to the adopted radiative model. In fact, Refs. [21] and [24] both adopted the gray gas approximation, but from different databases, Ref. [22] employed a spectral line based weighted sum of gray gases [25] (curve (a)) and a narrow–band model [26] (curve (b)) and the results of Ref. [23] were obtained with two different weighted sum of gray gases [27, 28] (curves (a) and (b) respectively). However, none of the aforementioned models was validated for temperatures above 3000 K, thus limiting its accuracy in LRE conditions and justifying the scattering in

[5] High-fidelity spectral models are usually valid at high temperatures, but have huge computational cost. Reduced-order models are, instead, calibrated on a small temperature range, usually limited to 2500 K [20], since the main interest in the radiative community has been flames burning air at ambient pressure.

the results.

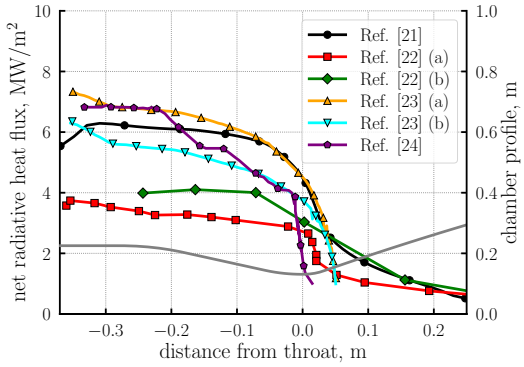

Figure 1.7. Literature data on the radiative heat flux in the SSME.

A few works have also assessed the effect of the radiative source term in the flow energy equation [29–32]. It is in fact known [33] that such coupling effect can have a deep impact in combustion simulations, affecting the maximum flame temperature and species and pollutant concentration. However, the most recent works on the topic [31, 32] have determined that this effect is negligible in rocket engine conditions. In particular, [31] performed coupled simulations on LOX-LH_2 and LOX-LCH_4 thrust chambers, revealing that even multiplying the source term by a factor of 100 lead to negligible changes in the flow temperature. Similarly, unsteady simulations performed on the CVRC (continuously variable resonance chamber) engine by [32], employing a state of the art full-spectrum κ-distribution, showed that the effect of radiation was negligible.

An additional consideration has to be made for engines burning hydrocarbon fuels, where soot may be a key factor from the radiative standpoint. In fact, soot is known to be a strong radiative emitter [7]. However, evaluation of soot concentration and distribution in real engineering applications is extremely challenging, and thus only few authors have tried to estimate soot radiation in LREs. For example, [34] analyzed a single coaxial jet injector of CH_2 and LOX, employing a detailed chemical kinetic approach, showing how the contribution of soot radiation was a significant fraction of the total heat flux. Similar results were obtained by [35] for a LOX - RP1 engine.

1.3.2 Hybrid rocket engines

The effect of radiative heat transfer in HREs has been investigated since the first comprehensive studies on HRE modeling [36], in which radiation was identified as a significant contributor to the energy balance on the fuel surface, particularly at low mass fluxes. Such conclusions were supported by the data of [37], in which radiative heat flux coming from gaseous products and soot particulate was measured in a slab burner at $G < 70$ kg/(m^2·s) to be up to 30% of the total one. Despite the early work of Strand et al. [37], experimental data on radiation heat transfer in HREs remains limited.

Numerical analyses have been performed by several authors [38–49]. Due to the high computational cost of radiation, several works have employed simplified

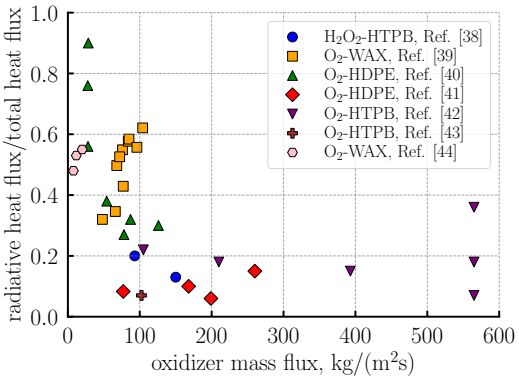

Figure 1.8. Literature data on the radiative share of the total heat flux in HREs.

correlations to include gas and/or soot contributions [41, 43, 46, 47]. Other authors have instead solved the full RTE, including only the gas contribution to radiation (for example [50] employing the gray gas approach and [38] with a weighted sum of gray gases model), showing how the contribution of gas radiation to the overall heat flux could be significant. Soot radiation was included by [48, 51], however without performing a comparison with experimental data and providing inconclusive evidence. The recent work of [52] showed instead that including soot radiation improved the agreement with experimental regression rate data in a GOX-paraffin engine. The available literature data is reported in Fig. 1.8, showing how radiation is expected to have a more relevant role at low mass fluxes.

1.3.3 Solid rocket motors

Modern solid propellants typically contain aluminum, which leads to the formation of alumina particles in the combustion products. These particles act as strong radiative emitters. Moreover, because their size is often comparable to or larger than the radiation wavelength, scattering phenomena may also occur, whereby photons are deflected after interacting with the particles. Although the absorption and scattering coefficients of a particle cloud can be estimated using semi-analytical models (Mie theory), significant challenges remain. These include uncertainties in the actual particle size distribution within the motor, uncertainties in the refractive index of alumina, and the high computational cost associated with detailed spectral radiative transfer calculations accounting for anisotropic scattering. Extensive research has addressed radiative heat transfer from solid rocket plumes [53–56], but a few studies have also focused on radiation within the nozzle itself. Despite the modeling challenges, radiation modeling in SRMs has received significant more attention that LREs or HREs in the literature.

One of the earliest contributions was by Pearce [57], who modeled the nozzle flow as a sequence of homogeneous, isothermal cylinders, and a single-scattering treatment for alumina particles. The study acknowledged the limitation of assuming isotropic scattering, which could underpredict heat flux by approximately 14%.

Building on this, Der and Nelson [58] employed a Monte Carlo method to compute emissivity for an isothermal alumina cloud, using Planck mean properties under a

gray assumption. They modeled anisotropic scattering and showed that isotropic assumptions could underpredict emissivity by over 30% in optically thick cases, though differences diminished at small optical thicknesses.

Dombrovskii [59] examined radiative transfer in divergent conical nozzles with a one-dimensional flowfield and a two-dimensional diffusion approximation for radiation, including a gamma particle size distribution and anisotropic scattering. Scattering from condensed-phase alumina dominated the results, with gas contributions minor, while wall thermal emission strongly influenced particle temperatures and the radiation field.

Coupled flowfield–radiation studies have been performed by [60, 61]. Duval et al. [60] used a two-dimensional flow solution and a one-dimensional radiation model including gas and particle contributions, finding particle radiation dominant. Anisotropic scattering increased predicted wall heat fluxes by about 37% compared to isotropic assumptions, while boundary layers attenuated wall heating. Jung and Brewster [61] coupled CFD with a finite volume radiation solver and compared with a Rosseland diffusion approximation, employing a bimodal particle size distribution. Their analysis highlighted the stronger role of small particles, but the published results were limited and did not report wall heat fluxes.

Further studies integrated radiation into ablation analyses. Previous studies by this research group [62, 63] applied both the Murphy–Kwong [57] and Dombrovsky [64] emissivity correlations, neglecting wall–flow reflections. The work of [65] showed that the radiative heat flux may be larger than the convective one in the convergent part of the nozzle, and that the radiative source term may have a relevant effect in the boundary layer. In the recent works of [66, 67] radiative computations were coupled to CFD simulations of 70-lb BATES motor [68], showing that, while radiation impacted significantly the wall heat flux, the erosion rate was mostly unaffected, being driven by the concentration of oxidizing species at the wall, which is not directly influenced by radiation.

Finally, it should be noted that the calculation of absorption and scattering coefficients, although based on well-established theories, relies on an accurate evaluation of the fundamental radiative properties of the particles, namely their refractive index, which depends on composition, temperature, and surface characteristics. For this reason, numerous experimental correlations are available in the literature for the refractive index of alumina [69], and it has been shown [65] that different models can yield substantially different radiative heat flux predictions. Moreover, when combustion is incomplete, particles are not composed solely of alumina but may also contain un-oxidized aluminum. It has been demonstrated that the refractive index, and hence the radiative properties, are strongly influenced by the oxide fraction of the particle [66, 70].

Experimental data on radiative heat flux in SRMs is scarce. Allport [71] measured radiative heat flux at the throat of a TM-3 nozzle, representing the only known direct measurements of this kind. More recently, Martin et al. [72, 73] reported radiative fluxes in laboratory-scale nozzles, though only in normalized form, precluding validation.

In summary, prior studies agree that alumina particle scattering and emission dominate radiative transfer in solid rocket nozzles, with anisotropy, particle size distributions, and boundary-layer effects all playing critical roles. However, the lack

of quantitative experimental benchmarks continues to constrain model validation.

1.4 Main objectives and thesis overview

The main objective of this investigation is to bridge the gap between radiation modeling and rocket engine analysis and design, developing tools for the estimation of the radiative heat flux and assessing its effect in test cases of practical interest. Despite the extensive literature on radiative heat transfer, its application to the specific environment of rocket engines is still lacking. Specifically, current predictive tools often rely on oversimplified gas property models or neglect the complex interaction between radiation and multiphase flows in solid and hybrid propulsion.

In this context, the present research is driven by two primary objectives. First, the study focuses on quantifying the impact of non-gray spectral behavior on the radiative properties of gases under high-pressure and temperature conditions, assessing how detailed spectral modeling alters the predicted thermal loads compared to traditional gray-gas approximations. Second, the analysis investigates how the spatial and size distribution of the dispersed phase—specifically soot and alumina particles—influences the radiative heat flux distribution within the combustion chambers and nozzles of hybrid and solid rocket motors.

This thesis is divided into two parts. In the first one, the theoretical and numerical framework adopted in this work is discussed. More specifically:

- Chapter 2 briefly presents all the models employed for the numerical simulation of LREs, HREs, and SRMs flowfields, which are the necessary base for radiative heat flux computations.
- Chapter 3 discusses the theoretical and numerical model for thermal radiation, presenting the radiative transfer equation and describing the radiative properties of combustion gases and particles.
- Chapter 4 reports the development and validation of a numerical solver used to compute the radiative heat flux in rocket engine thrust chambers.

The second part of this work presents the results of the investigations. Given that each type of rocket engine comes wit its own peculiarities and challenges, each engine class is discussed in a separate chapter:

- Chapter 5 focuses on liquid rocket engines, assessing which radiation models are suited for combined high-temperature and pressure calculations. Reduced order models are developed to compute both radiative properties of gases and the radiative heat flux at a fraction of the computational cost, and validated through comparison with reference solutions in both oxygen-hydrogen and oxygen-methane test cases.
- Chapter 6 assesses the impact of gas and soot radiation on the fuel regression rate of hybrid rocket engines. Several firing tests of an oxygen-HTPB hybrid rocket are numerically rebuilt, discussing how taking into account radiation can improve the agreement with experimental regression rate data.

- Chapter 7, finally, discusses the effect of particle and gas radiation on the thermal protection systems of solid rocket motors. In particular, the analysis aims to assess the effect of various simplifying assumptions that can be made concerning the radiative properties of the two-phase combustion products, such as isotropic scattering or gray body. Results are obtained in both a 1D test case and a reference SRM nozzle.

Part I

Modeling

Chapter 2

Mathematical model: fluid dynamics

Contents

In this chapters all mathematical and numerical models employed in the CFD simulations are described. Since the main focus of this work is on the radiation heat transfer, and not on the fluid dynamics modeling itself, the description is ketp brief and the interested reader is referred to the relevant references.

2.1 Conservation principles

The fluid dynamics model relies on the turbulent and reactive set of Navier–Stokes equations, expressing mass, momentum and energy conservation within a generic control volume. Chemical reactions are accounted for by using a number of mass conservation equations consistent with the number of species constituting the mixture, as well as by suitably modeling chemical source terms. Turbulence effects are taken into account by using RANS equations, properly closed by an additional equation for turbulent viscosity.

The integral form of the species mass conservation is given by the following scalar equation:

$$\frac{\mathrm{d}}{\mathrm{d}t}\int_V \rho_i \,\mathrm{d}V + \oint_S \rho_i \mathbf{u}\cdot\hat{\mathbf{n}}\mathrm{d}S = -\oint_S \rho_i v_i \,\mathrm{d}S + \int_V \dot{\omega}_i \,\mathrm{d}V \tag{2.1}$$

where $\mathbf{u}$ is the mixture velocity, v_i is the i–th species diffusion velocity, ρ_i is the i–th species density, $\dot{\omega}_i$ is the i–th species chemical production/destruction rate and V is the volume. Notice that by summing up all the species continuity equations, the mass conservation for the gas mixture is obtained:

$$\frac{\mathrm{d}}{\mathrm{d}t}\int_V \rho \,\mathrm{d}V + \oint_S \rho\mathbf{u}\cdot\hat{\mathbf{n}}\mathrm{d}S = 0 \tag{2.2}$$

because of the mixture density definition:

$$\rho = \sum_{i=1}^{N} \rho_i \tag{2.3}$$

as well as the null contributions:

$$\sum_{i=1}^{N} \dot{\omega}_i = 0 \tag{2.4}$$

$$\sum_{i=1}^{N} \rho_i v_i = 0 \tag{2.5}$$

The integral form of the momentum conservation is given by the following vectorial equation:

$$\frac{\mathrm{d}}{\mathrm{d}t}\int_V \rho\mathbf{u}\,\mathrm{d}V + \oint_S (\rho\mathbf{u}\cdot\hat{\mathbf{n}})\mathbf{u}\,\mathrm{d}S = \int_V \rho\mathbf{f}\mathrm{d}V + \oint_S \mathbf{t}\,\mathrm{d}S \tag{2.6}$$

where ρ is the mixture density and $\mathbf{f}$ and $\mathbf{t}$ are the volume and surface forces, respectively. The surface forces vector, in particular, can be expressed as the scalar product between the stress tensor, decomposed in a spherical and a viscous component, and the normal to the surface:

$$t_l = \sigma_{lm} n_m = \left(-p\delta_{lm} + \tau_{lm}\right) n_m \tag{2.7}$$

while the spherical component is related to the mixture pressure, the viscous component of the stress tensor is, in turn, given by the Newton's law:

$$\tau_{lm} = \mu\left(\frac{\partial u_l}{\partial x_m} + \frac{\partial u_m}{\partial x_l} - \frac{2}{3}\frac{\partial u_n}{\partial x_n}\delta_{lm}\right) \tag{2.8}$$

with μ being the mixture dynamic viscosity.

The integral form of the energy conservation is given by the following scalar equation:

$$\frac{\mathrm{d}}{\mathrm{d}t}\int_V \rho e_0 \,\mathrm{d}V + \oint_S (\rho\mathbf{u}\cdot\hat{\mathbf{n}})e_0 \,\mathrm{d}S = \int_V \rho\mathbf{f}\cdot\mathbf{u}\mathrm{d}V + \oint_S \mathbf{t}\cdot\mathbf{u}\,\mathrm{d}S - \oint_S \mathbf{q}\cdot\hat{\mathbf{n}}\,\mathrm{d}S + \int_V \nabla\cdot\mathbf{q}_{\mathrm{rad}}dV \tag{2.9}$$

where e_0 is the mixture internal energy and $\mathbf{q}$ is the heat flux. The heat flux vector, in particular, can be expressed through a diffusive and a convective contribution given by Fourier's law:

$$q_l = \sum_{i=1}^{N} \rho_i u_{i,l} h_i - k \frac{\partial T}{\partial x_l} \tag{2.10}$$

with k being the mixture thermal conductivity and h the entalphy.

2.2 Equation of state

The mixture is assumed to be composed of thermally perfect gases. According to this assumption, mixture pressure p and temperature T are related with each other by the well known equation of state:

$$p = \rho R T \tag{2.11}$$

where the mixture gas constant R is given by:

$$R = \frac{\mathcal{R}}{M} = \sum_{i=1}^{N} y_i R_i = \mathcal{R} \sum_{i=1}^{N} \frac{y_i}{M_i} \tag{2.12}$$

with $\mathcal{R}$ being the universal gas constant, M the mixture molar mass, R_i the i–th species gas constant, M_i the i–th species molar mass and y_i the i–th species mass fraction.

2.3 Thermophysical properties

According to the thermally perfect gas assumption, the single species thermophysical properties are described as a function of temperature only.

Thermodynamics properties of species are described by seventh–order polynomials of temperature using the chemical equilibrium with applications (CEA) database [74] for the relevant coefficients. In particular, constant pressure specific heat $c_{p,i}$, enthalpy h_i and entropy at atmospheric pressure s_i are expressed as polynomials:

$$\frac{c_{p,i}}{R} = \frac{a_1}{T^2} + \frac{a_2}{T} + a_3 + a_4 T + a_5 T^2 + a_6 T^3 + a_7 T^4 \tag{2.13}$$

$$\frac{h_i}{RT} = -\frac{a_1}{T^2} - \frac{a_2}{T} \ln T + a_3 + a_4 \frac{T}{2} + a_5 \frac{T^2}{3} + a_6 \frac{T^3}{4} + a_7 \frac{T^4}{5} + \frac{b_1}{T} \tag{2.14}$$

$$\frac{s_i}{R} = -\frac{a_1}{2T^2} - \frac{a_2}{T} + a_3 \ln T + a_4 T + a_5 \frac{T^2}{2} + a_6 \frac{T^3}{3} + a_7 \frac{T^4}{4} + b_2 \tag{2.15}$$

Mixture thermodynamics properties are then evaluated by:

$$c_p = \sum_{i=1}^{N} y_i c_{p,i} \tag{2.16}$$

$$h = \sum_{i=1}^{N} y_i h_i \tag{2.17}$$

$$s = \sum_{i=1}^{N} y_i s_i \tag{2.18}$$

Transport properties of species are described by fourth–order polynomials of temperature also according to CEA. Molecular viscosity μ_i and thermal conductivity k_i are expressed as:

$$\ln \mu_i = A_\mu \ln T + \frac{B_\mu}{T} + \frac{C_\mu}{T^2} + D_\mu \tag{2.19}$$

$$\ln k_i = A_k \ln T + \frac{B_k}{T} + \frac{C_k}{T^2} + D_k \tag{2.20}$$

The diffusion coefficient D_i is considered to be the same for all species through a constant Schmidt number:

$$D_i = D = \frac{\mu}{\rho S_c} \tag{2.21}$$

Mixture viscosity and thermal conductivity are then derived from Wilke's semi–empirical rule [75]:

$$\mu = \sum_{i=1}^{N} \frac{x_i \mu_i}{\sum_j x_j \phi_{ij}} \tag{2.22}$$

$$k = \sum_{i=1}^{N} \frac{x_i k_i}{\sum_j x_j \phi_{ij}} \tag{2.23}$$

with the ϕ_{ij} coefficients given by:

$$\phi_{ij} = \frac{1}{\sqrt{8}} \left(1 + \frac{M_i}{M_j}\right)^{-1/2} \left[1 + \sqrt{\frac{\mu_i}{\mu_j}} \left(\frac{M_j}{M_i}\right)^{1/4}\right]^2 \tag{2.24}$$

2.4 Chemical source terms

Chemical reactions are modeled according to a finite–rate approach, hence by assuming the transformation of reactants into products species to occur through a sequence of chemical non–equilibrium states. The overall reaction process is then computed through its evolution in time, i.e. the series of intermediate reaction steps.

To account for finite–rate chemistry, the chemical source terms $\dot{\omega}_i$ in Eq. (2.1) are required for each species $i = 1,...,N$. Each reaction $j = 1,...,M$ that involves the i–th species, in particular, contributes to the i–th source term through the relevant reaction rate v_j according to the law of mass action:

$$v_j = k_{j_f} \prod_{i=1}^{N} [\cdot]_i^{\nu_{i_j}^r} - k_{j_b} \prod_{i=1}^{N} [\cdot]_i^{\nu_{i_j}^p} \tag{2.25}$$

where $[\cdot]_i$ is the concentration of the i–th species, ν_{i_j} is the stoichiometric coefficient of the i–th species in the j–th reaction, with superscripts r and p indicating reactants and products, respectively, and k_j is the reaction rate constant relevant to the j–th reaction, with subscripts f and b indicating the forward and backward directions, respectively. Notice that reaction rate constants are expressed with an Arrhenius–type equation:

$$k_j = A_j \, T^{n_j} \exp\left(-\frac{E_{a_j}}{RT}\right) \tag{2.26}$$

where A_j is the pre–exponential factor, n_j the temperature exponent and E_{a_j} the activation energy of the j–th reaction. Once the reaction rates are known, the source terms can be easily evaluated according to:

$$\dot{\omega}_i = M_i \sum_{j=1}^{M} \Delta\nu_{i_j} v_j \tag{2.27}$$

where $\Delta\nu_{i_j}$ is the difference of the stoichiometric coefficients in the reaction direction of the i–th species in the j–th reaction.

2.5 Turbulence closure equation

Turbulence effects, such as mixing enhancement, are modeled by exploiting the property of a turbulent flow to have clean and steady mean properties despite its chaotic change of velocity, tridimensional and irregular vorticity distribution and continuous dependence on initial conditions. Each flow variable ϕ is, in fact, decomposed into an average $\overline{\phi}$ and fluctuating component ϕ', according to:

$$\phi = \overline{\phi} + \phi' = \frac{\overline{\rho\phi}}{\overline{\rho}} + \phi' \tag{2.28}$$

and substituted into the conservation principles to obtain RANS equations. For such averaged equations, the Reynolds stress tensor, which represents the dissipation due to field oscillations, appears unclosed. This point is overcome by expressing the Reynolds stress tensor as a function of averaged variables and, in particular, according to the Boussinesque assumption, as a function of the mean velocity gradient, by analogy with viscous stresses. In this way the problem of unclosed equations is transferred to the description of turbulent viscosity by a suitable model. In this work either the Spalart–Allmaras [76] or the k-ω SST [77] models have being employed.

Spalart Allmaras model

In this model the Reynolds stress tensor is assumed to be related to the strain rate tensor through the turbulent viscosity μ_T:

$$-\rho\overline{u_i' u_j'} = \mu_T S_{ij} \tag{2.29}$$

while the turbulence closure equation is written in terms of an auxiliary intermediate variable $\tilde{\nu}$ defined as:

$$\tilde{\nu} = \frac{\mu_T}{\rho f_{\nu 1}} \tag{2.30}$$

with $f_{\nu 1}$ a damping coefficient. The additional partial differential equation (PDE) for turbulent viscosity computation is given by:

$$\frac{D\tilde{\nu}}{Dt} = b_{prod}(S,\tilde{\nu}) - b_{dest}(\tilde{\nu},d) + \frac{1}{\sigma}[\nabla\cdot((\nu+\tilde{\nu})\nabla\tilde{\nu}) + c_{b2}\nabla\tilde{\nu})^2] \tag{2.31}$$

where the different terms account for production, destruction and diffusion/convection of $\tilde{\nu}$, respectively. The Spalart–Allmaras turbulence model appears suitable for complex internal, external and boundary layer flows, economical for large meshes, simpler

than two equation models with good performances in the case of separation. Once the turbulent viscosity is known, turbulent thermal conductivity k_T and turbulent diffusion D_T are determined from the constant pressure specific heat by assuming constant turbulent Prandtl and Schmidt numbers:

$$k_T = \frac{\rho \nu_T c_p}{P_{rT}} \tag{2.32}$$

$$D_T = \frac{\nu_T}{S_{cT}} \tag{2.33}$$

k-ω SST

The Shear Stress Transport (SST) k–ω combines k–ω by Wilcox in the proximity of walls with k–ε away from walls to achieve independence from farfield boundary conditions. Two transport equations for turbulence kinetic energy k and specific rate of dissipation ω are solved:

$$\frac{\partial(\rho k)}{\partial t} + \frac{\partial(\rho U_j k)}{\partial x_j} = P_k - \beta^* \rho k \omega + \frac{\partial}{\partial x_j}\left[(\mu + \sigma_k \mu_t)\frac{\partial k}{\partial x_j}\right], \tag{2.34}$$

$$\frac{\partial(\rho \omega)}{\partial t} + \frac{\partial(\rho U_j \omega)}{\partial x_j} = \alpha \frac{\omega}{k} P_k - \beta \rho \omega^2 + \frac{\partial}{\partial x_j}\left[(\mu + \sigma_\omega \mu_t)\frac{\partial \omega}{\partial x_j}\right] + 2(1 - F_1)\rho \sigma_{\omega 2} \frac{1}{\omega}\frac{\partial k}{\partial x_j}\frac{\partial \omega}{\partial x_j}. \tag{2.35}$$

and the turbulent viscosity is defined as:

$$\mu_t = \frac{\rho a_1 k}{\max(a_1 \omega,\, S F_2)}, \qquad S = \sqrt{2 S_{ij} S_{ij}}. \tag{2.36}$$

Two blending functions F_1 e F_2 make the transition from k–ω and k–ε equations smooth:

$$F_1 = \tanh\left(\arg_1^4\right), \quad \arg_1 = \min\left[\max\left(\frac{\sqrt{k}}{\beta^* \omega y},\, \frac{500\nu}{y^2 \omega}\right),\, \frac{4\rho \sigma_{\omega 2} k}{CD_{k\omega} y^2}\right] \tag{2.37}$$

$$F_2 = \tanh\left(\arg_2^2\right), \quad \arg_2 = \max\left(\frac{2\sqrt{k}}{\beta^* \omega y},\, \frac{500\nu}{y^2 \omega}\right) \tag{2.38}$$

$$CD_{k\omega} = \max\left(2\rho \sigma_{\omega 2} \frac{1}{\omega}\frac{\partial k}{\partial x_j}\frac{\partial \omega}{\partial x_j},\, 10^{-10}\right) \tag{2.39}$$

All the model coefficients are blended between k–ω values ϕ_1 and k–ε values ϕ_2:

$$\phi = F_1 \phi_1 + (1 - F_1)\phi_2, \tag{2.40}$$

$$\alpha_1 = 5/9, \quad \alpha_2 = 0.44, \quad \beta_1 = 3/40, \quad \beta_2 = 0.0828,$$
$$\beta^* = 0.09, \quad \sigma_{k1} = 0.85, \quad \sigma_{k2} = 1.0, \quad \sigma_{\omega 1} = 0.5, \quad \sigma_{\omega 2} = 0.856,$$
$$a_1 = 0.31.$$

In Eq. (2.34) P_k is the production limiter

$$P_k = \min\left(\tau_{ij}\frac{\partial U_i}{\partial x_j},\, 10\beta^* \rho k \omega\right), \qquad \tau_{ij} = 2\mu_t S_{ij} - \tfrac{2}{3}\rho k \delta_{ij}. \tag{2.41}$$

2.6 Numerical method

The adopted in–house RANS solver is developed to treat three–dimensional, turbulent, compressible, multi–component and reacting flows. The interaction between turbulence and chemical kinetics is computed according to a laminar flame model. The solver adopts a second order accurate in space finite-volume Godunov formulation [78]. To allow second order accuracy in space, a linear cell reconstruction of flow variables is carried out by using the value in the considered cell and those in the contiguous ones. The HLLC Riemann solver is used [79]. This allows to evaluate variables at cell interfaces and associated fluxes to compute the evolution in time. Time integration is based on the Strang operator–splitting technique [80], with convective and diffusive terms integrated by a second–order Runge–Kutta scheme, whereas for the chemical source term a stiff ordinary differential equation (ODE) implicit integrator is used [81]. The solver has been verified against experimental data in very different operating conditions and applications [82–85].

2.7 Gas–surface interaction boundary conditions

Two special boundary conditions are adopted for the simulation of fuel grains in hybrid rockets and ablative thermal protection systems. The model solves mass and energy balances at the interface between the gas and the solid phases, which, together with gas–phase combustion and surface chemical models, yield a coupled gas–surface solution. The surface mass and energy balances are connected with the CFD solver because of the presence of gradients which involve the knowledge of variables both at interface and inside the flow field.

2.7.1 HRE fuel grains

In this work only HTPB fuel grains are considered. Since HTPB is a pyrolizing fuel [86], the fuel regression rate $\dot{r}$ is computed from the wall temperature T_{wall} through an Arrhenius equation

$$\dot{r} = A \exp\left(-E_a/(\mathcal{R}T_{\text{wall}})\right) \tag{2.42}$$

where $\mathcal{R}$ is the universal gas constant. At the fuel surface, mass and energy balance equations are solved, leading to the following equation

$$\rho_{\text{fuel}}\dot{r}\left[\Delta h_p + c_{\text{fuel}}\left(T_{\text{wall}} - T_{\text{fuel,initial}}\right)\right] = q_{\text{convective}} + q_{\text{radiative}} \tag{2.43}$$

which is solved for the unknown wall temperature T_{wall}. The Arrhenius and solid fuel parameters (specific heat c_{fuel}, heat of pyrolisis Δh_p, density ρ_{fuel}) are taken from [83, 86] and reported in Table 2.1.

Table 2.1. Solid fuel data [83].

c_{fuel} (J/(kg · K))	$T_{\text{fuel},initial}$ (K)	Δh_p (MJ/kg)	ρ_{fuel} (kg/m^3)
1632	298.15	1.1	960

2.7.2 Ablative materials

In this work (Sec. 7.3) carbon-phenolic thermal protection systems are considered. The gas-surface interaction model solves the mass and energy balances and takes into account the heterogeneous chemical reactions at the nozzle surface, the rate of diffusion of the species through the boundary layer, and the ablation species and pyrolysis gas injection in the boundary layer. The total mass flux at the wall is given by the sum of two contributions

$$\rho_v \dot{r} = \dot{m}_{\text{char}} + \dot{m}_{pg} \tag{2.44}$$

where v is the virgin material and pg are the pyrolysis gases. The ablation mass flux of carbon due to the surface heterogeneous reactions is modeled with a semi-global heterogeneous reaction mechanism for non-porous graphite (C_s) oxidation [87] consisting of five reactions (Table 2.2).

Table 2.2. Heterogeneous rate constants and reaction order of carbon with H_2O, CO_2, OH, O, and O_2 [87].

$C_s + H_2O$	$\rightarrow$	$CO + H_2$
$C_s + CO_2$	$\rightarrow$	$2CO$
$C_s + OH$	$\rightarrow$	$CO + H$
$C_s + O$	$\rightarrow$	CO
$C_s + \frac{1}{2}O_2$	$\rightarrow$	CO

The pyrolysis gas contribution is computed from the virgin material and char densities

$$\frac{\dot{m}_{pg}}{\dot{m}_{\text{char}}} = \left(\frac{\rho_v}{\rho_{\text{char}}} - 1 \right) \tag{2.45}$$

assuming that the pyrolysis gases are in equilibrium conditions. Further details on the model can be found in [88].

2.8 Condensed phase modeling: AL_2O_3 particles

Two-phase computations are employed for solid rocket motors simulations. The gaseous phase is described by means of the compressible Navier-Stokes equations, while the alumina particles are modeled via a pressureless Eulerian approach [89]. The total number of particles is decomposed into a certain number of groups, each with its own characteristic diameter and set of equations. As the flow is assumed to be dilute (i.e. the volume fraction of the alumina particles is negligible when compared to the gaseous phase), only gas-particle interactions are modeled whereas any coupling among the particle groups is neglected.

The governing equations for the gaseous ($_g$) and condensed phases ($_p$) are respectively reported in Eqs.2.46 and 2.47:

$$\frac{\partial(\rho_g)}{\partial t} + \nabla \cdot (\rho_g \mathbf{u}_g) = -\nabla \cdot \mathbf{j}_i \tag{2.46a}$$

$$\frac{\partial(\rho_g \mathbf{u}_g)}{\partial t} + \nabla \cdot (\rho_g \mathbf{u}_g \mathbf{u}_g) = \nabla \cdot \mathbf{S} - \sum_{k=1}^{N_k} \mathbf{F}_{d,k} \tag{2.46b}$$

$$\frac{\partial(\rho E_g)}{\partial t} + \nabla \cdot (\rho_g E_g \mathbf{u}_g) = \nabla \cdot (\mathbf{u}_g \cdot \mathbf{S}) - \nabla \cdot \mathbf{q} - \sum_{k=1}^{N_k} (\mathbf{F}_{d,k} \cdot \mathbf{u}_{p,k} - Q_{c,k}) \tag{2.46c}$$

$$\frac{\partial(\rho_{p,k})}{\partial t} + \nabla \cdot (\rho_{p,k} \mathbf{u}_{p,k}) = 0 \tag{2.47a}$$

$$\frac{\partial(\rho_{p,k} \mathbf{u}_{p,k})}{\partial t} + \nabla \cdot (\rho_{p,k} \mathbf{u}_{p,k} \mathbf{u}_{p,k}) = \mathbf{F}_{d,k} \qquad (k = 1, \ldots, N_\mathrm{k}) \tag{2.47b}$$

$$\frac{\partial(\rho E_{p,k})}{\partial t} + \nabla \cdot (\rho_{p,k} E_{p,k} \mathbf{u}_{p,k}) = \mathbf{F}_{d,k} \cdot \mathbf{u}_{p,k} + Q_{c,k} \tag{2.47c}$$

where the term $E_g = e_g + \mathbf{u}^2/2$ represents the total energy per unit mass of the gaseous phase, which is the sum of the internal energy $e_g = \Delta e_\mathrm{f}^\circ + \int_{T^0}^{T} c_v \, dT$ and the kinetic energy. The same expression holds also for the condensed phase, nevertheless in this case the internal energy is a function of constant specific heat, c_s. Subscript k refers to the k^{th} particle group. Particles are assumed as spherical and a monokinetic closure is employed. Concerning the gaseous set of equations, the quantities reported under the divergence sign on the right-hand side of Eq.2.46 can be expressed as:

$$\begin{aligned}
\mathbf{j}_i &= -\left(\frac{\mu}{\rho Sc} + \frac{\mu_\mathrm{T}}{\rho Sc_\mathrm{T}}\right) \nabla y_i \\
\mathbf{S} &= -p\mathbf{I} - (\mu + \mu_\mathrm{T}) \left\{ \frac{2}{3} (\nabla \cdot \mathbf{u}_g)\mathbf{I} + \left[\nabla \mathbf{u}_g + (\nabla \mathbf{u}_g)^\mathrm{T} \right] \right\} \\
\mathbf{q} &= -\left(k + \frac{\mu_\mathrm{T}}{Pr_\mathrm{T}} c_p\right) \nabla T_g + \sum_{k=1}^{N_g} \left(\Delta h_\mathrm{f}^\circ + \int_{T^0}^{T} c_p \, dT \right) \mathbf{j}_i
\end{aligned} \tag{2.48}$$

which stand for the species diffusion vector, the stress tensor, and the heat flux vector, respectively.

Several formulas can be used to determine the two-way source terms. In general, they are related to the number of particles per unit of volume, written as:

$$N_{p,k} = \frac{6\rho_{p,k}}{\pi \, \rho_{Al_2O_3} \, D_{p,k}^3} \tag{2.49}$$

where $\rho_{Al_2O_3}$ represents the alumina density and $D_{p,k}$ the diameter characterizing each group of particles. For what concerns the drag force, the classical law for a cloud of N_p particles, assumed valid for a single group of particles, reads (hereafter the k subscript is omitted for simplicity):

$$\mathbf{F}_d = \frac{1}{8} \pi \rho_g D_p^2 N_p C_d \, (\mathbf{u}_g - \mathbf{u}_p) \, |\mathbf{u}_g - \mathbf{u}_p| \tag{2.50}$$

with the drag coefficient, C_d, evaluated accordingly with the formulation derived by Henderson [90]. Convection is taken into account through the following relation:

$$Q_c = \pi k D_p N_p (T_g - T_p) Nu \tag{2.51}$$

As well as for the drag coefficient, gases rarefaction is taken into for the mathematical formulation of the Nusselt number, Nu. In this spirit, Kavanau and Drake expression is employed [91].

2.9 Condensed phase modeling: soot

Modeling soot formation and oxidation in combustion systems remains a major challenge due to the complex interplay of chemical kinetics, transport phenomena, and particle dynamics. Detailed soot models typically involve large reaction mechanisms and the solution of population balance equations, leading to prohibitive computational costs when coupled with multidimensional CFD solvers. Moreover, the scarcity of experimental data under practical operating conditions, such as those encountered in hybrid rocket engines, makes the calibration and validation of such detailed models highly uncertain. For these reasons, a simplified soot model based on a single transport–reaction equation for the soot mass fraction y_{soot}, assuming spherical particles of constant diameter, is adopted in this work:

$$\frac{\partial \rho y_{\text{soot}}}{\partial t} + \nabla \cdot (\rho \mathbf{v} y_{\text{soot}}) = \dot{\omega}_{\text{soot}} \tag{2.52}$$

No diffusive phenomena are taken into consideration. Soot particles are considered as spherical with a diameter $D_{\text{soot}} = 30$ nm and a soot density of 1800 kg/m^3 [48].

For the soot source term two different models are tested. The first one is a global soot model [44, 92] based on the local mixture fraction ξ

$$\dot{\omega}_{\text{soot}} = \dot{\omega}_{\text{soot,form}} - \dot{\omega}_{s,\text{ox}} \tag{2.53}$$

$$\dot{\omega}_{\text{soot,form}} = A_f \rho^2 \left(\frac{\xi - \xi_{st}}{1 - \xi_{st}} \right) T^{2.25} \exp\left(-T_a/T\right) \tag{2.54}$$

$$\dot{\omega}_{\text{soot,ox}} = A_o [O_2] T^{1/2} \exp\left(-E_a/(\mathcal{R}T)\right) \rho y_{\text{soot}} \frac{6 f_v}{D_{\text{soot}}} \tag{2.55}$$

The first term accounts for soot formation from precursors, while the second for soot oxidation due to molecular oxygen. It is also assumed that the formation term is active only for $\xi \in [\xi_{so}, \xi_c]$ and that the oxidation term is active for $\xi \in [0, \xi_{so}]$. The mixture fraction where soot formation starts ξ_c is computed as 2.5 the stoichiometric value ξ_{st}, while ξ_{so} is computed for a generic C_xH_y hydrocarbon as

$$\xi_{so} = \frac{(C/O)_c}{(C/O)_c + \left(\frac{1}{\xi_{st}} - 1\right) / \left(2 + \frac{1}{2}\frac{y}{x}\right)} \tag{2.56}$$

where $(C/O)_c$ is the critical carbon to oxygen ratio for soot production, taken as 0.6 [44]. All constants (A_f, T_a, A_o, E_a) are taken from [44], where the model has been

employed by [44] to assess the effect of soot radiation in oxygen-paraffin wax hybrid rockets.

The second soot model is the *Leung* model from [93], which considers acetylene C_2H_2 as soot precursor species

$$\dot{\omega}_{\text{soot}} = \mathcal{M}_{\text{soot}} \left(\dot{\omega}_{\text{soot,nucleation}} + \dot{\omega}_{\text{soot,growth}} - \dot{\omega}_{\text{soot,ox}} \right) \tag{2.57}$$

$$\dot{\omega}_{\text{soot,nucleation}} = 1 \times 10^4 \exp(-21100/T) \left[C_2H_2 \right] \tag{2.58}$$

$$\dot{\omega}_{\text{soot,growth}} = 6 \times 10^3 \exp(-12100/T) \left[C_2H_2 \right] \sqrt{A_{\text{soot}}} \tag{2.59}$$

$$\dot{\omega}_{\text{soot,ox}} = 1 \times 10^4 T^{0.5} \exp(-19680/T) \left[O_2 \right] A_{\text{soot}} \tag{2.60}$$

where $\mathcal{M}_{\text{soot}}$ is the soot molar mass (12 kg/kmol) and A_{soot} is the soot surface area per unit volume $A_{\text{soot}} = 6 f_v / D_{\text{soot}}$. The first term accounts for soot nucleation, the second for soot surface growth, and the third for soot oxidation.

Chapter 3

Mathematical model: radiative heat transfer

Contents

This chapter presents the mathematical description of radiation heat transfer in a participating medium, describing the radiative transfer equation (Sec. 3.1), and the optical properties of gases (Sec. 3.2) and particles (Sec. 3.3). The description will be kept brief, and the reader is again referred to the relevant literature.

3.1 Radiative transfer equation

The fundamental quantity of radiation heat transfer is the spectral intensity $\mathcal{I}_\eta(\mathbf{r}, \hat{\mathbf{s}})$, defined as energy per unit area per unit time per unit solid angle per unit wavenumber, traveling at position $\mathbf{r}$ in direction $\hat{\mathbf{s}}$. Making an energy balance on a pencil of rays

(accounting for emission, absorption, out-scattering and in-scattering) leads to the transient spectral radiative transfer equation (RTE)

$$\frac{1}{c}\frac{\partial \mathcal{I}_\eta}{\partial t} + \hat{\mathbf{s}}\cdot\nabla\mathcal{I}_\eta = j_\eta - \kappa_{\mathrm{abs},\eta}\mathcal{I}_\eta - \kappa_{\mathrm{sca},\eta}\mathcal{I}_\eta + \frac{\kappa_{\mathrm{sca},\eta}}{4\pi}\int_{4\pi}\mathcal{I}_\eta(\hat{\mathbf{s}}_i)\,\Phi_\eta(\hat{\mathbf{s}}_i,\hat{\mathbf{s}})\,d\Omega_i, \quad (3.1)$$

where c is the speed of light, $\kappa_{\mathrm{abs},\eta}$ is the absorption coefficient, $\kappa_{\mathrm{sca},\eta}$ the scattering coefficient, j_η the emission coefficient, and $\Phi_\eta(\hat{\mathbf{s}}_i,\hat{\mathbf{s}})$ the scattering phase function describing the probability of redirection from $\hat{\mathbf{s}}_i$ into $\hat{\mathbf{s}}$.

Under local thermodynamic equilibrium the emission coefficient is related to the blackbody spectral intensity $\mathcal{I}_{b,\eta}(T)$ by $j_\eta = \kappa_{\mathrm{abs},\eta}\mathcal{I}_{b,\eta}$. Introducing the extinction (or total attenuation) coefficient $\beta_\eta = \kappa_{\mathrm{abs},\eta} + \kappa_{\mathrm{sca},\eta}$ and neglecting the transient term gives the quasi–steady spectral RTE

$$\hat{\mathbf{s}}\cdot\nabla\mathcal{I}_\eta = \kappa_{\mathrm{abs},\eta}\mathcal{I}_{b,\eta} - \beta_\eta\mathcal{I}_\eta + \frac{\kappa_{\mathrm{sca},\eta}}{4\pi}\int_{4\pi}\mathcal{I}_\eta(\hat{\mathbf{s}}_i)\,\Phi_\eta(\hat{\mathbf{s}}_i,\hat{\mathbf{s}})\,d\Omega_i. \quad (3.2)$$

This spectral integro-differential equation explicitly shows that: absorption removes intensity (term $-\kappa_{\mathrm{abs},\eta}\mathcal{I}_\eta$ of $-\beta_\eta\mathcal{I}_\eta$), emission adds intensity (term $\kappa_{\mathrm{abs},\eta}\mathcal{I}_{b,\eta}$), and scattering removes and redistributes intensity (terms with $\kappa_{\mathrm{sca},\eta}$ and Φ_η). The scattering phase function Φ_η quantifies the probability of a photon traveling in direction $\hat{\mathbf{s}}_i$ to be scattered in direction $\hat{\mathbf{s}}$, and is such that

$$\frac{1}{4\pi}\int_{4\pi}\Phi_\eta(\hat{\mathbf{s}}_i,\hat{\mathbf{s}})d\Omega = 1 \quad (3.3)$$

It is common to re-write the RTE introducing the source function S_η

$$S_\eta(\mathbf{r},\hat{\mathbf{s}}) \;=\; (1-\omega_\eta)\,\mathcal{I}_{b,\eta} \;+\; \frac{\omega_\eta}{4\pi}\int_{4\pi}\mathcal{I}_\eta(\hat{\mathbf{s}}_i)\,\Phi_\eta(\hat{\mathbf{s}}_i,\hat{\mathbf{s}})\,d\Omega_i. \quad (3.4)$$

where $\omega_\eta = \kappa_{\mathrm{sca},\eta}/(\kappa_{\mathrm{abs},\eta}+\kappa_{\mathrm{sca},\eta})$ is the scattering albedo. Adopting as variable the optical distance τ_η defined by $d\tau_\eta = \beta_\eta\,ds$ along the ray, the RTE along the ray becomes

$$\frac{d\mathcal{I}_\eta}{d\tau_\eta} + \mathcal{I}_\eta = S_\eta(\tau_\eta,\hat{\mathbf{s}}). \quad (3.5)$$

If the source function S_η is known (or approximated), the linear first-order equation (3.5) admits the following solution along a ray from a boundary point at $\tau_\eta = 0$ to the interior point at τ_η:

$$\mathcal{I}_\eta(\tau_\eta,\hat{\mathbf{s}}) = \mathcal{I}_\eta(0,\hat{\mathbf{s}})\,e^{-\tau_\eta} + \int_0^{\tau_\eta} S_\eta(\tau'_\eta,\hat{\mathbf{s}})\,e^{-(\tau_\eta-\tau'_\eta)}\,d\tau'_\eta. \quad (3.6)$$

Equivalently, written in spatial form with explicit extinction β_η and wall intensity $\mathcal{I}_{\mathrm{wall},\eta}$

$$\mathcal{I}_\eta(\mathbf{r},\hat{\mathbf{s}}) = \mathcal{I}_{\mathrm{wall},\eta}(\mathbf{r}_{\mathrm{wall}},\hat{\mathbf{s}})\exp\Big(-\int_0^s\beta_\eta\,ds'\Big) + \int_0^s S_\eta(\mathbf{r}',\hat{\mathbf{s}})\exp\Big(-\int_{s'}^s\beta_\eta\,ds''\Big)\,\beta_\eta\,ds', \quad (3.7)$$

where $s = |\mathbf{r}-\mathbf{r}_{\mathrm{wall}}|$ and $\mathbf{r}_{\mathrm{wall}}$ is the wall point along the ray.

3.1.1 Boundary condition for a diffuse surface

For an opaque surface that emits and reflects diffusely, the outgoing intensity is independent of direction. For a surface point $\mathbf{r}_{\text{wall}}$ with normal $\hat{\mathbf{n}}$, emissivity $\varepsilon(\mathbf{r}_{\text{wall}})$ and diffuse reflectivity $\rho(\mathbf{r}_{\text{wall}})$ the boundary condition is

$$\mathcal{I}_\eta(\mathbf{r}_{\text{wall}}, \hat{\mathbf{s}}) \;=\; \varepsilon(\mathbf{r}_{\text{wall}})\, \mathcal{I}_{b,\eta}(T_w) \;+\; \frac{\rho(\mathbf{r}_{\text{wall}})}{\pi} \int_{\hat{\mathbf{n}}\cdot\hat{\mathbf{s}}'<0} \mathcal{I}_\eta(\mathbf{r}_{\text{wall}}, \hat{\mathbf{s}}')\, |\hat{\mathbf{n}} \cdot \hat{\mathbf{s}}'|\, d\Omega', \tag{3.8}$$

valid for $\hat{\mathbf{n}} \cdot \hat{\mathbf{s}} > 0$ (outgoing directions). The black surface is the special case $\rho = 0$, $\varepsilon_{\text{wall}} = 1$, so $\mathcal{I}_\eta(\mathbf{r}_{\text{wall}}, \hat{\mathbf{s}}) = \mathcal{I}_{b,\eta}(T_{\text{wall}})$.

3.1.2 Spectral radiative heat flux and its divergence

The spectral radiative heat flux vector is the first angular moment of the intensity

$$\mathbf{q}_\eta(\mathbf{r}) \;=\; \int_{4\pi} \mathcal{I}_\eta(\mathbf{r}, \hat{\mathbf{s}})\, \hat{\mathbf{s}}\, d\Omega, \tag{3.9}$$

and the total radiative flux is $\mathbf{q} = \displaystyle\int_0^\infty \mathbf{q}_\eta \, d\eta$. The heat flux on a boundary surface can instead be computed as

$$q_{\text{wall}} = \int_{4\pi} \mathcal{I}_\eta(\hat{n} \cdot \hat{s}) d\Omega \tag{3.10}$$

where $\hat{n}$ is the normal to the wall.

Integrating the steady RTE (3.2) over all solid angles yields the spectral balance for the divergence of the radiative flux:

$$\begin{aligned} \nabla \cdot \mathbf{q}_\eta &= \int_{4\pi} \hat{\mathbf{s}} \cdot \nabla \mathcal{I}_\eta \, d\Omega = 4\pi\kappa_{\text{abs},\eta}\mathcal{I}_{b,\eta} - \kappa_{\text{abs},\eta} \int_{4\pi} \mathcal{I}_\eta \, d\Omega \\ &= \kappa_{\text{abs},\eta}(4\pi\mathcal{I}_{b,\eta} - G_\eta), \end{aligned} \tag{3.11}$$

where $G_\eta(\mathbf{r}) \equiv \displaystyle\int_{4\pi} \mathcal{I}_\eta(\mathbf{r}, \hat{\mathbf{s}})\, d\Omega$ is the spectral incident radiation. Notably, scattering does not appear explicitly in (3.11) because scattering redistributes intensity but does not change local spectral energy content. Integrating (3.11) over wavenumber gives the divergence of the total radiative flux,

$$\nabla \cdot \mathbf{q} = \int_0^\infty \kappa_\eta (4\pi\mathcal{I}_{b,\eta} - G_\eta)\, d\eta. \tag{3.12}$$

3.1.3 Numerical solution methods for the RTE

The spectral radiative transfer equation (3.2) is a six-dimensional problem (three spatial coordinates, two angular coordinates, and one spectral coordinate). Its solution in practical configurations requires numerical approximations in both spatial and angular domains. Over the years, several families of solvers have been developed, differing in their angular discretization strategy, computational cost, and accuracy. The most widely used approaches are briefly summarized below, and the reader is

referred to [7] further details.

The P_N (Spherical Harmonics) method. The P_N method expands the intensity $I_\eta(\hat{\mathbf{s}})$ into a series of spherical harmonics up to order N. This converts the integro-differential RTE into a set of coupled partial differential equations for the expansion coefficients. The lowest-order case, P_1, corresponds to the diffusion approximation, valid in optically thick media. Increasing N improves angular resolution but significantly increases computational cost and may lead to unphysical oscillations ("ray effects") near discontinuities. P_N methods are attractive for nearly isotropic radiation fields and are often used in reactor physics and participating media with high optical thickness.

Discrete Ordinates Method (DOM). In the DOM, the angular domain is discretized into a finite number of discrete directions $\hat{\mathbf{s}}_m$ with associated weights w_m. The RTE is then solved for each ordinate, typically using a finite-volume or finite-difference scheme in space. The DOM can capture strong directional effects and anisotropic scattering with moderate computational cost. However, it suffers from "ray effects" in optically thin or highly collimated fields, where radiation travels preferentially along the discrete ordinate directions. Despite this, DOM remains the most widely implemented solver in coupled CFD–radiation applications due to its robustness and ease of integration with structured grids.

Finite Volume Method (FVM) for radiation. The FVM for radiation integrates the RTE over both control volumes and solid angles, leading to a balance equation for the average intensity within each spatial and angular cell. It preserves energy conservation by construction and naturally aligns with the finite-volume framework used in CFD solvers. The FVM typically uses a limited number of discrete control angles (similar to DOM) but avoids some of the ray-effect issues through angular averaging. Accuracy depends on the chosen angular and spatial resolution.

Discrete Transfer Method (DTM). The DTM simplifies the angular dependence by tracing a finite number of representative rays through the domain. Along each ray, the RTE is integrated analytically using the formal solution (3.7). This approach is computationally efficient for geometrically complex domains and optically thin media, where scattering is weak or neglected. However, the computational cost for scattering-dominated problems becomes high, and the overall conservation of energy can be ensured only by using fine angular and spacial grids.

Monte Carlo (MC) method. The MC method simulates the random trajectories of a large number of energy bundles ("photons"), following probabilistic rules for emission, absorption, scattering, and reflection. It provides a statistically exact solution of the RTE, independent of geometry or optical properties, and naturally handles anisotropic and spectral effects. Its major drawbacks are high computational cost and statistical noise, which require large numbers of samples for converged results. MC methods are therefore mainly used as reference solutions for model validation or in simplified geometries.

In this work the DTM approach is employed. This choice is motivated by previous

work [94, 95] and by the high accuracy of the method. An extensive description of the numerical solver is presented in Chap. 4.

3.2 Radiative properties of gas molecules

Gas molecules exhibit a strong non–gray behaviour, meaning that the absorption coefficient shows significant variations across the spectrum. In fact, when a molecule interacts with a photon, its energy state may either increase (if the photon is absorbed) or decrease (if the photon is emitted). Scattering by gas molecules can usually be neglected. Since quantum mechanics postulates that energy levels are discrete or quantized, only photons with a certain energy or frequency may be absorbed or emitted, resulting in the spectra of molecules showing a strong line structure. Such lines usually suffer from broadening effects, which make the absorption and emission spectrum of molecular gases continuous, although wildly oscillating. For this reason, one has either to resort to high–fidelity models, which try to resolve the spectrum and come at a huge computational cost, or to reduced order models, which however may have limited application ranges. In the following subsections all the models employed in this work are briefly described.

3.2.1 Line by line

The line–by–line (LBL) approach [7] computes the absorption coefficient[1] as the sum of the contributions from all lines of all participating species

$$\kappa_\eta = \sum_{\text{species}} \kappa_{\eta,i_s} \tag{3.13}$$

$$\kappa_{\eta,i_s} = \sum_{\text{lines}} \kappa_{\eta,i} = \mathcal{N} x_{i_s} \sum_{\text{lines}} \mathcal{S}_i \phi(\eta) \tag{3.14}$$

where the sum extends over all lines whose intensity $\mathcal{S}_i$ is larger than a threshold $\mathcal{S}_{\text{cut}}$. Equation (3.14) also shows that the total absorption coefficient is the sum of the ones of each participating species, weighted with their molar fraction. The location of the spectral lines, their intensity $\mathcal{S}$, and other relevant parameters are available in high–resolution spectral databases, realized with a combination of *ab initio* calculations and spectroscopic measurements.

In this work the HITEMP 2010 spectral database has been employed [96], which is the most comprehensive and accurate spectroscopic database for H_2O and CO_2 molecules [97], and has successfully been compared with high temperature spectra of water vapor and carbon dioxide (e.g. up to 2900 K for H_2O and 1950 K for CO_2 in [96]). Water vapor data is reported as reliable up to 4000 K, although validation at very high temperatures is hindered by the lack of experimental data [96]. For high temperature carbon dioxide calculations also the CDSD-4000 database is available [98]. However, it was not adopted in this work, due to the high computational cost resulting from its large number of lines. Nonetheless, it will be shown in Sec. 5.2.2 how CO_2 impacts the total emissivity of the combustion products by less than 10% in most relevant conditions, thus limiting the effect of its LBL database choice.

[1] the abs pedix will be dropped in this section for the sake of simplicity

The calculation of the spectral absorption coefficient from the line information contained in the aforementioned spectroscopic databases requires, however, accounting for various line broadening mechanisms, which make the line absorption coefficient $\kappa_{\eta,i}$ not truly monochromatic, but spread over a finite range of wavenumbers. Such range is quantified by the cut off half width η_{trunc}, such that each line is broadened up to η_{trunc} cm^{-1} from its center. The broadening of the absorption coefficient is described by the line shape function $\phi(\eta)$, whose shape depends on the physical phenomenon causing the broadening. The most relevant ones are collision between molecules (which induces the so-called *Lorentz* broadening) and the *Doppler* effect, which are often considered together (the combined line shape takes the name of *Voigt* profile). It has been shown that, for high pressure conditions, collisional broadening is by far the most important mechanism [7]. However, the *Lorentz* profile does not manage to take into account the line mixing effects typical of high–pressure conditions [99]. Alternative profiles, such as the *pseudoLorentz* one, have been proposed, showing excellent agreement with experimental data up to 100 bar [99]. Nevertheless, LBL calculations for LOX-H_2 and LOX-CH_4 combustion products in typical LRE conditions (up to 300 bar and 4000 K) revealed that the effect of the line model on the total emissivity is less than 2%. For this reason, and because the *pseudoLorentz* profile is not validated for the temperature range typical of LREs, the *Voigt* model was employed in the calculations. Additional discussions on the selection of the spectral parameters employed in the calculations are presented in Sec. 5.1 and 5.2.

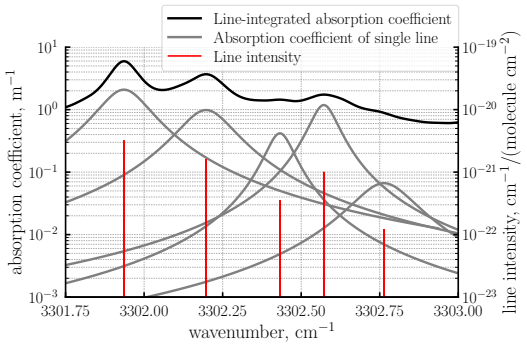

Figure 3.1. Spectral absorption coefficient for water vapor diluted in air at 3600 K and 1 bar ($x_{H_2O} = 0.8$).

An example of spectrally resolved absorption coefficient computed with the LBL approach is reported in Fig. 3.1, which shows the line intensities, line absorption coefficients, and total absorption coefficient for a mixture containing water vapor diluted in air ($x_{H_2O} = 0.8$) at 3600 K and 1 bar. In the small considered range, spanning from 3301.75 cm^{-1} to 3300 cm^{-1}, the HITEMP database lists 12254 lines, but only a selection is reported for the sake of clarity, together with their *Lorentz*–broadened absorption coefficient. Figure 3.1 shows how LBL computations require to take into account a very large amount of lines, which is in the order 10^7 for high temperature applications, through a very fine spectral discretization, resulting in high memory requirements and large computational times and making it an impractical approach for engineering computations. LBL computations performed in this work

have been performed employing the RADIS package [100], and have been employed as benchmark to assess the performance of models with lower computational cost.

3.2.2 Statistical narrow band

In narrow-band models spectral integration is conducted over narrow bands, typically spanning a few tens of cm^{-1}, to compute the average emissivity or transmissivity of the band. This allows to significantly reduce the computational cost, while at the same time retaining the main features of the spectrum (see Fig. 3.2). The main drawback of narrow–band models is that they do not yield, at least in their standard formulation, the absorption coefficient, but the column transmissivity, which is expressed as

$$\tau = \exp\left[-\frac{\overline{\beta}}{\pi}\left(\sqrt{1+\frac{2\pi x p L \overline{\kappa}}{\overline{\beta}}}-1\right)\right] \tag{3.15}$$

where $\overline{\kappa}$ is the mean line intensity to line spacing ratio in a band and $\overline{\beta}$ is the ratio between the average line Lorentz half–width and the mean line spacing. For mixtures containing multiple participating species, the total transmissivity is computed as the product of the ones of the single species [101], and for non-homogeneous conditions the Curtis-Godson approximation is employed [102]. The narrow–band model adopted in this work is the statistical narrow band (SNB) model of [101], with a narrow band width of 25 cm^{-1}, with 450 spectral intervals covering the range 25-11250 cm^{-1}. The model contains data for mixtures of H_2O, CO_2, CO, and CH_4 up to 5000 K (2000 K for methane), covering all the temperatures of interest in this work. It is based on LBL calculations performed with the HITEMP-2010 database for H_2O, CO and with CDSD-4000 for CO_2. The model coefficients do not depend explicitly on pressure, and SNB results have shown to compare well with LBL calculations up to 1000 cm· atm [101]. It will be shown in Sec. 5.1.2 and 5.2.2 how the model is in good agreement with LBL calculations up to 300 bar.

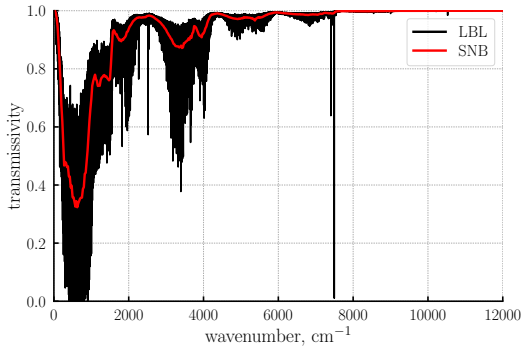

Figure 3.2. Spectral transmittance for water vapor at 3600 K and 1 bar ($x_{H_2O} = 0.8$) computed with the LBL and SNB models.

Working with the transmissivity, instead of the absorption coefficient, is not always compatible with standard RTE solvers, thus making the use of narrow band models in test cases of practical interest uncommon. It is however possible to perform

a simplification if $2\pi x L p\overline{\kappa}/\overline{\beta} << 1$ (weak absorption limit). Under this hypothesis Eq. (3.15) becomes simply

$$\tau = \exp\left(-xpL\overline{\kappa}\right) \tag{3.16}$$

To quantify the error induced by the weak absorption limit approximation (SNBW) with respect to the full SNB, Fig. 3.3 compares the emissivities computed by both approaches for two mixtures, one containing water vapor ($x_{H_2O} = 0.67$, representative of oxygen–hydrogen combustion products at $OF = 6$) and one containing combustion products of oxygen and methane at $OF = 3.4$ ($x_{H_2O} = 0.49, x_{CO_2} = 0.13, x_{CO} = 0.178$). It can be seen that the error remains below 2% for typical combustion chamber conditions (temperature and pressure above 2000 K and 20 bar, respectively) for all path lengths. On the other hand, larger errors are introduced at lower pressures and temperatures, such as the ones obtained in the divergent part of a nozzle. Similar conclusions were obtained by [60].

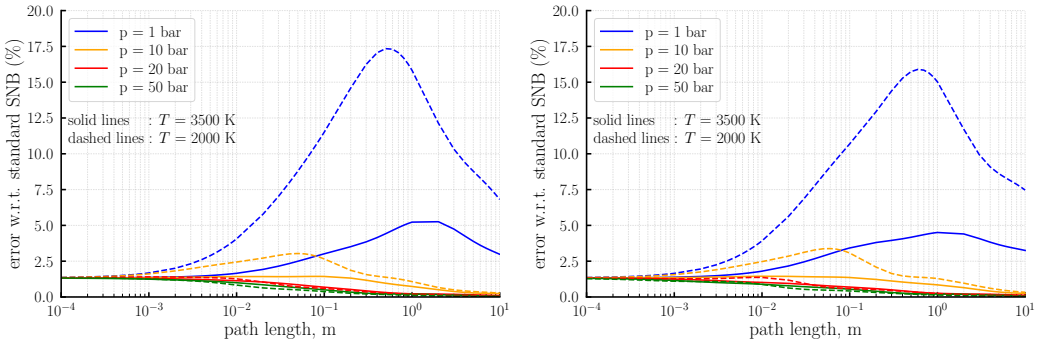

(a) Oxygen–hydrogen combustion products. (b) Oxygen–methane combustion products.

Figure 3.3. Percentage error of the emissivity calculated with SNBW with respect to SNB model at different temperature and pressures. Error is calculated as $(\varepsilon_{SNBW} - \varepsilon_{SNB})/\varepsilon_{SNB}$.

3.2.3 Weighted sum of gray gases

The weighted sum of gray gases (WSGG) is a global model, meaning that it does not aim to represent the real emission spectrum, but only to yield a correct total emissivity [103]. In this approach it is assumed that a non–gray gas can be modeled as the combination of N_g fictitious gray gases, such that

$$\mathcal{I} = \sum_{i_g=0}^{N_g} a_{i_g} \left[\mathcal{I}(0) + \mathcal{I}_b \left(1 - e^{-\kappa_{i_g} L}\right)\right] \tag{3.17}$$

where a_{i_g} and κ_{i_g} are the weights and absorption coefficients of the i_g^{th} gray gas, usually expressed as functions of temperature, pressure and mixture composition. It is custom to take $\kappa_0 = 0$, to allow for transparency windows, and to compute $a_0 = 1 - \sum_{i_g=1}^{N_g} a_{i_g}$. WSGG models are extremely common in engineering applications, since it has been shown that they can yield very good results even with only 3 or 4 gray gases. However, being a_{i_g} and κ_{i_g} obtained by fitting emissivity data obtained

with LBL or SNB models, each WSGG model comes with its own validity range, and no WSGG model validated at the high temperatures and pressures typical of LREs is currently available in the literature. For this reason, new WSGGs for mixtures containing H_2O and H_2O–CO_2 will be obtained in Sec. 5.1 and 5.2.

3.2.4 Spectral line based WSGG

The spectral line based weighted sum of gray gases (SLW) is a global radiation model whose formulation is quite similar to the WSGG one [104]. In fact, while in the WSGG κ_{i_g} and a_{i_g} are simply coefficients fitted to obtain a given total emissivity, in the SLW the absorption coefficient is partitioned in a set of intervals $\tilde{\kappa}_{i_g}$, and it is recognized that the gray gas weight a_{i_g} is the fraction of the blackbody energy contained in the spectral regions where the absorption coefficient is between $\tilde{\kappa}_{i_g}$ and $\tilde{\kappa}_{i_g+1}$. In practice, once the set of $\tilde{\kappa}_{i_g}$ is defined, the gray gas weights are computed from LBL databases as

$$a_{i_g} = \frac{\int_{\Delta_{i_g}} \mathcal{I}_{b,\eta} d\eta}{\mathcal{I}_b}, \quad \Delta_{i_g} = \{\eta : \tilde{\kappa}_{i_g-1} < \kappa < \tilde{\kappa}_{i_g}\} \tag{3.18}$$

The solution of Eq. (3.18) can be extremely computational intensive, and its application to test cases of practical interest requires the use of tabulated values of the so–called Absorption Line Distribution Function (ALBDF), which are available for H_2O, CO_2 and CO for $T \in [300, 3000]$ K and $p \in [0.1, 50]$ atm [105].

3.2.5 Gray gas approximation

In the gray gas (GG) approximation the RTE is simplified as

$$\mathcal{I} = \mathcal{I}_0 e^{-\kappa_P L} + \mathcal{I}_b (1 - e^{-\kappa_P L}) \tag{3.19}$$

where κ_P is the Planck-Mean absorption coefficient, defined as

$$\kappa_P = \frac{\int_0^\infty \kappa_\eta \mathcal{I}_{b,\eta} d\eta}{\mathcal{I}_b} \tag{3.20}$$

The gray gas approximation allows to greatly reduce the computational cost of radiative calculations, since it replaces the millions of spectral points needed for LBL calculations with a single value. However, this comes with a loss of accuracy, especially for optically thick media [106]. The gray gas absorption coefficients used in this work are taken from [101].

3.3 Radiative properties of particles

Particles are known to emit, absorb, and scatter radiation [107, 108]. Their radiative properties are complex functions of their composition, shape, surface properties, temperature, and of wavelength. We shall limit ourselves to clouds of spherical particles, for which an extended semi-analytical theory (called Mie theory) is available. A thorough description of its mathematical framework is outside the scope of this

work[2], and the reader is referred to Chapter 4 of [109] for further details. Only the most important elements of the theory are reported in this section.

3.3.1 Mie theory for spherical particles

For spherical particles of diameter D and complex refractive index $m = n - ik$ embedded in a nonabsorbing medium of unitary refractive index, the interaction with monochromatic radiation of wavelength λ can be described by an expansion in spherical harmonics of a plane electromagnetic wave. From such expansion one can compute the spectral scattering, extinction, and absorption efficiencies

$$Q_{\mathrm{sca},\lambda} = \frac{2}{x^2} \sum_{n=1}^{\infty} (2n+1) \left(|a_n|^2 + |b_n|^2 \right), \tag{3.21}$$

$$Q_{\mathrm{ext},\lambda} = \frac{2}{x^2} \sum_{n=1}^{\infty} (2n+1) \Re(a_n + b_n), \tag{3.22}$$

$$Q_{\mathrm{abs},\lambda} = Q_{\mathrm{ext},\lambda} - Q_{\mathrm{sca},\lambda}. \tag{3.23}$$

a_n and b_n are the Mie coefficients, computed as

$$a_n = \frac{m\psi_n(mx)\psi_n'(x) - \psi_n(x)\psi_n'(mx)}{m\psi_n(mx)\xi_n'(x) - \xi_n(x)\psi_n'(mx)}, \tag{3.24}$$

$$b_n = \frac{\psi_n(mx)\psi_n'(x) - m\psi_n(x)\psi_n'(mx)}{\psi_n(mx)\xi_n'(x) - m\xi_n(x)\psi_n'(mx)}, \tag{3.25}$$

where ψ_n and ξ_n are Riccati–Bessel functions and primes denote derivatives with respect to their arguments. x is the dimensionless size parameter, defined as

$$x = \frac{\pi D}{\lambda} \tag{3.26}$$

The scattering function can be computed as

$$\Phi_\lambda(\theta) = \frac{2}{x^2 Q_{\mathrm{sca},\lambda}} \left(|S_1(\theta)|^2 + |S_2(\theta)|^2 \right). \tag{3.27}$$

where the amplitude function S are

$$S_1(\theta) = \sum_{n=1}^{\infty} \frac{2n+1}{n(n+1)} \left[a_n \pi_n(\cos\theta) + b_n \tau_n(\cos\theta) \right], \tag{3.28}$$

$$S_2(\theta) = \sum_{n=1}^{\infty} \frac{2n+1}{n(n+1)} \left[a_n \tau_n(\cos\theta) + b_n \pi_n(\cos\theta) \right]. \tag{3.29}$$

The gray efficiencies can be computed integrating over wavelength

$$Q_{\mathrm{abs}}(T, D) = \int_0^{\infty} Q_{\mathrm{abs},\lambda}(D)\, f(\lambda, T)\, d\lambda, \tag{3.30}$$

$$Q_{\mathrm{sca}}(T, D) = \int_0^{\infty} Q_{\mathrm{sca},\lambda}(D)\, f(\lambda, T)\, d\lambda, \tag{3.31}$$

where $f(\lambda, T)$ is the normalized Planck spectral distribution. The refractive indices $n(\lambda, T)$ and $k(\lambda, T)$ are generally obtained from tabulated optical data or empirical correlations for the specific particle material.

[2] and quite mathematically involved

3.3.2 Radiative properties of particle clouds

When many particles are present, the medium behaves as a two-phase participating system in which radiation undergoes multiple absorption and scattering events. The overall (macroscopic) radiative properties depend on the individual particle efficiencies, the particle number density N_p, and the particle size distribution function $g(D)$. The absorption and scattering coefficients of a particle cloud are given by

$$\kappa_{\text{abs}} = N_p \int_0^\infty C_{\text{abs}}(D) \frac{\partial g(D)}{\partial D}\, dD = N_p \int_0^\infty \frac{\pi D^2}{4} Q_{\text{abs}}(D) \frac{\partial g(D)}{\partial D}\, dD, \tag{3.32}$$

$$\kappa_{\text{sca}} = N_p \int_0^\infty C_{\text{sca}}(D) \frac{\partial g(D)}{\partial D}\, dD = N_p \int_0^\infty \frac{\pi D^2}{4} Q_{\text{sca}}(D) \frac{\partial g(D)}{\partial D}\, dD. \tag{3.33}$$

where C is the absorption/scattering cross-section. The particle number density is related to the particle mass fraction Y_p, the mixture density ρ_m, and the particle material density ρ_p through

$$N_p = \frac{\rho_m Y_p}{\rho_p \bar{V}}, \qquad \bar{V} = \int_0^\infty \frac{\pi D^3}{6} \frac{\partial g(D)}{\partial D}\, dD, \tag{3.34}$$

where $\bar{V}$ is the mean particle volume.

The effective scattering phase function of the cloud is obtained by averaging the single-particle phase function over the particle size distribution:

$$\Phi(\theta) = \frac{N_p \int_0^\infty \frac{\pi D^2}{4} Q_{\text{sca}}(D)\, \Phi(D,\theta)\, \frac{\partial g(D)}{\partial D} dD}{\kappa_{\text{sca}}}. \tag{3.35}$$

These macroscopic quantities κ_{abs}, κ_{sca}, and $\Phi(\theta)$ are the parameters required in the radiative transfer equation to describe absorption, emission, and scattering by a dispersed phase.

In many practical applications, the particle size distribution is represented by a log-normal function, characterized by a geometric mean diameter D_g and a standard deviation σ_g. The optical behavior of the ensemble is strongly influenced by the relative contribution of small and large particles, as well as by the angular dependence of scattering, which is typically forward-peaked for large particles.

3.3.3 Rayleigh approximation for small particles

When the particle size is much smaller than the wavelength of incident radiation ($x = \pi D/\lambda \ll 1$), Mie theory reduces to the *Rayleigh scattering regime*. In this limit, the absorption and scattering efficiencies can be expressed in closed form as [109]:

$$Q_{\text{abs},\lambda} = 4x\, \Im\left(\frac{m^2-1}{m^2+2}\right), \tag{3.36}$$

$$Q_{\text{sca},\lambda} = \frac{8}{3} x^4 \left|\frac{m^2-1}{m^2+2}\right|^2. \tag{3.37}$$

Scattering in this regime is isotropic, with the phase function $\Phi(\theta) = 1$. The x^4 dependence of Q_{sca} indicates that scattering rapidly decreases as particle size

diminishes, whereas absorption remains proportional to x. Consequently, very small particles predominantly absorb and emit radiation rather than scatter it.

Although the Rayleigh approximation is valid only for particles with $x \ll 1$, it offers significant physical insight and serves as a computationally efficient alternative when the particle size distribution is dominated by submicron particles.

3.4 Refractive index models

The radiative properties of a particle are determined by its refractive index, which is typically obtained from experimental data. This section briefly presents the refractive index models employed in this work.

Alumina particles

Concerning alumina particles, which are strong radiative emitters in solid rocket motors, several correlations are available for both the real and imaginary part. An extended review of all available models is reported in [65, 69, 110] and is outside the scope of this work. In this work (Chap. 7) the *Farmer* [54] is employed for the real part of the refractive index

$$n = 1.75 \cos(6\lambda) \tag{3.38}$$

where the constant 6 has the units of $^\circ/\mu m$, and the *Plastinin* correlation for the imaginary part [111]

$$k = 0.023 \frac{\lambda}{n} \exp\left(-\frac{7200}{\lambda^* T}\right), \quad \frac{1}{\lambda^*} = 0.6916 \left(\frac{12890}{T} - 2.232\right) \tag{3.39}$$

Soot

As for alumina particles, many models and correlations are available for the radiative properties of soot. Its refractive index is influenced by several factors, such as the hydrogen content (the higher the H/C ratio the lower the absorption coefficient), and the soot morphology, which depends on the specific operating conditions were soot is generated. For an extended review the reader is referred to [7, 112, 113]. In this work (Sec. 6.2.2) the Chang and Charalampopoulos correlation [114] is employed

$$n = 1.8111 + 0.1263 \ln(\lambda) + 0.0270 \ln^2(\lambda) + 0.0417 \ln^3(\lambda) \tag{3.40}$$

$$k = 0.5821 + 0.1213 \ln(\lambda) + 0.2309 \ln^2(\lambda) - 0.0100 \ln^3(\lambda) \tag{3.41}$$

valid for $\lambda \in [0.4, 30]$ μm.

Chapter 4

Discrete transfer method algorithm

Contents

The discrete transfer method algorithm presented in this chapter closely follows the original formulation by [115]. The method is based on the discretization of the radiative field into a finite number of representative rays, or beams, which are traced between the boundaries of the enclosure and through the participating medium. The radiative transfer equation is then solved along these predefined directions to determine the intensity distribution, from which the volumetric radiative source terms required by the energy equation are obtained. The model maintains an explicit representation of the underlying physical processes while avoiding excessive mathematical abstraction, and has proven particularly suitable for engineering applications involving complex reacting flows and radiating media. This chapter presents the ray tracing and RTE integration algorithms for all adopted models, code verification results are reported in Appendix A1.

4.1 Spatial and angular discretization

The algorithm has been specifically formulated for structured grids, since those are employed by the CFD solvers employed in this work. A generic grid is reported as an example in Fig. 4.1. For the evaluation of the wall heat flux rays are traced from the centers of the boundary faces (red squares), while for the radiative source term they are traced from the cell centers (black squares). Concerning the wall points, the solid angle to be discretized corresponds to an half-sphere directed inward towards the enclosure. In order to ensure that the same angular discretization is employed for all faces, regardless of their orientation, a local reference frame $\{f\}$ is established,

centered in the face center and with an orthonormal basis $[\hat{\boldsymbol{\tau}}, \hat{\mathbf{b}}, \hat{\mathbf{n}}]$, where $\hat{\mathbf{n}}$ is the face normal directed inward, $\hat{\boldsymbol{\tau}}$ is the versor directed along the main face direction and $\hat{\mathbf{b}}$ is computed as the cross product of $\hat{\mathbf{n}}$ and $\hat{\boldsymbol{\tau}}$ (see Fig. 4.2).

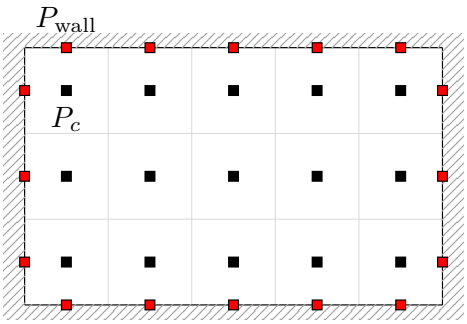

Figure 4.1. Grid example.

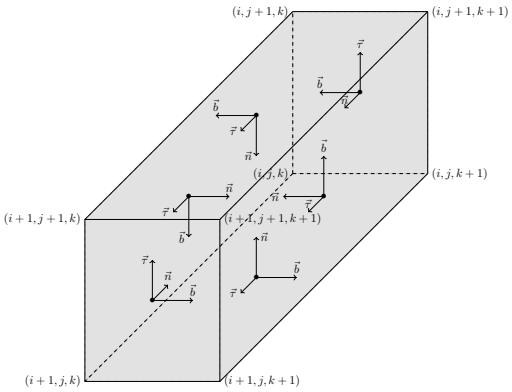

Figure 4.2. Reference frames of cell faces.

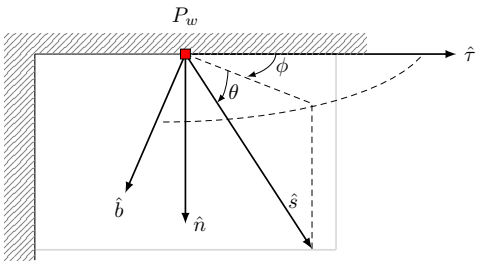

Figure 4.3. Spherical coordinate system.

In the local reference frame two polar coordinates (θ, ϕ) are defined, with $\theta \in [0, \pi/2]$ taken from the $\hat{\boldsymbol{\tau}} - \hat{\mathbf{b}}$ plane and $\phi \in [0, 2\pi]$ taken anticlockwise around $\hat{\mathbf{n}}$ (see Fig. 4.3). The angular coordinates are discretized in N_r directions, divided in $N_\phi = 2\sqrt{N_r}$ and $N_\theta = \frac{1}{2}\sqrt{N_r}$. This discretization ensures that

$$\Delta\phi = \frac{2\pi}{N_\phi} = \Delta\theta = \frac{\pi}{2N_\theta} = \frac{\pi}{\sqrt{N_r}} \tag{4.1}$$

Once the number of directions has been chosen, an angular grid is computed as follows

$$\theta_{i_\theta} = \frac{\pi}{4N_\theta} + (i_\theta - 1)\Delta\theta \tag{4.2}$$

$$\phi_{i_\phi} = \frac{\pi}{N_\phi} + (i_\phi - 1)\Delta\phi \tag{4.3}$$

For each direction (i_θ, i_ϕ) the ray versor $\hat{\mathbf{s}}$ can be expressed in the local frame[1] as

$$ {}^{f}\hat{\mathbf{s}}_{i_\phi, i_\theta} = \begin{bmatrix} \cos(\theta_{i_\theta}) \cos(\phi_{i_\phi}) \\ \cos(\theta_{i_\theta}) \sin(\phi_{i_\phi}) \\ \sin(\theta_{i_\theta}) \end{bmatrix} \tag{4.4} $$

To obtain the ray in the cartesian frame the transformation matrix ${}_fR = \left[\hat{\boldsymbol{\tau}}, \hat{\mathbf{b}}, \hat{\mathbf{n}}\right]$ is introduced, and the cartesian components of $\hat{\mathbf{s}}$ are obtained as

$$ \hat{\mathbf{s}} = {}_fR^{f}\hat{\mathbf{s}} $$

For the evaluation of the radiative source term rays are traced from the cell centers. In this case there is no need to define a local reference frame, and $\theta \in [-\pi/2, \pi/2]$ is taken from the $x-y$ plane and $\phi \in [0, 2\pi]$ is around the z axis.

4.2 Ray tracing procedure

Once the ray starting point $\mathbf{P}_{\text{wall}}$ and its direction $\hat{\mathbf{s}}$ have been selected, the ray is traced in the CFD grid until another intersection with the enclosure is found. Figure 4.4 reports an example of ray tracing with four rays on the same reference grid of Fig. 4.1.

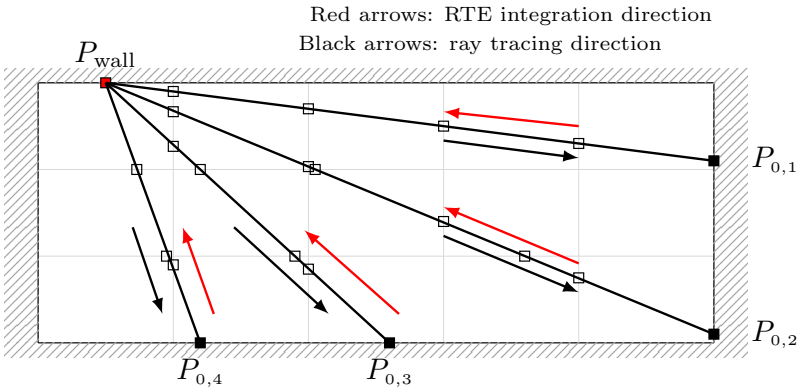

Figure 4.4. Example of ray tracing procedure.

Starting from the initial cell, we look for the intersection between the line $r : \mathbf{P}_0 + \hat{\mathbf{s}}t$ (where $\mathbf{P}_0$ is a generic starting point) and the planes containing the cell faces. To do so, for each of the 6 cell faces we solve the equation

$$ \hat{\mathbf{n}}_f \times (\mathbf{P} - \mathbf{P}_c) = 0 \tag{4.5} $$

where $\mathbf{P}_c$ is the face center, $\hat{\mathbf{n}}_f$ is the face normal, and $\mathbf{P} = \mathbf{P}_0 + \hat{\mathbf{s}}t$ is the intersection point. The above equation can be solved in terms of the abscissa t, leading to

$$ t = \frac{\hat{\mathbf{n}} \cdot (\mathbf{P}_c - \mathbf{P}_0)}{\hat{\mathbf{n}} \cdot \hat{\mathbf{s}}} \tag{4.6} $$

[1]Concerning vectors and reference frames, the following notation is employed: ${}^{f}\vec{P}$ represents a vector written in coordinate system $\{f\}$, and if the leading superscript is omitted it is implied that the vector is written in the cartesian reference frame. Subscripts are employed to identify rotation matrices, for example ${}_fR$ is the rotation matrix from reference $\{f\}$ to the cartesian one.

To check if the intersection **P** lies inside the 4 vertexes of the face the sum of the angles between **P** and each pair of the vertexes is computed. If the sum is 2π the intersection is inside the face, otherwise **P** is outside (Fig. 4.5). Once the intersection has been found, the ray exiting point becomes the entry point in the next cell and the procedure is repeated.

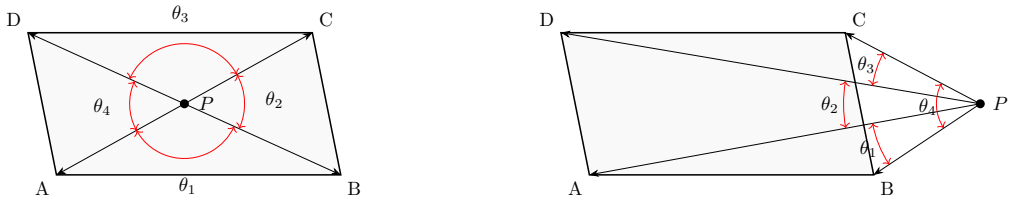

(a) $\sum_{i=1}^{4} \theta_i = 2\pi \Rightarrow P$ inside

(b) $\sum_{i=1}^{4} \theta_i < 2\pi \Rightarrow P$ outside

Figure 4.5. Determination of intersection between ray and cell face.

4.2.1 Boundary conditions

When the ray encounters a boundary face, the tracing procedure is stopped only if the boundary corresponds to a physical wall or to an inlet/outlet conditions. However, it is common to employ symmetry and periodic boundary conditions, especially to reduce the computational cost. For these cases, special procedures are applied.

Specular

If the ray encounters a face for wich a simmetry boundary condition is specified (Fig. 4.6), the ray is reflected, according to

$$\hat{\mathbf{s}}^{\text{new}} = \hat{\mathbf{s}}^{\text{old}} - 2(\hat{\mathbf{s}}^{\text{old}} \cdot \hat{\mathbf{n}}_f)\hat{\mathbf{n}}_f \tag{4.7}$$

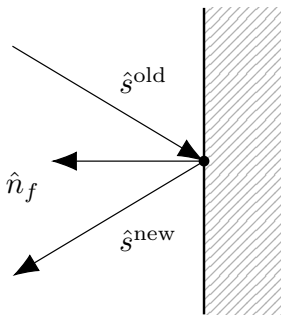

Figure 4.6. Symmetry boundary condition.

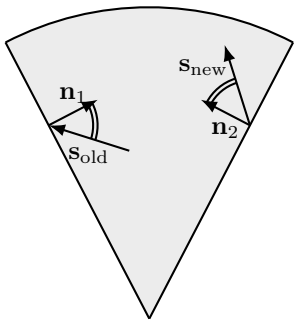

Figure 4.7. Wedge boundary condition.

Wedge

In 2D-axisymmetric simulations it is customary to adopt a computational setup made of a wedge of small aperture angle. When the ray encounters one of the lateral faces of the wedge, a rotation of the ray and a translation of its application point have to be performed. As shown in Fig. 4.7 for a planar case, the ray is rotated such that the angle with the face normal is preserved.

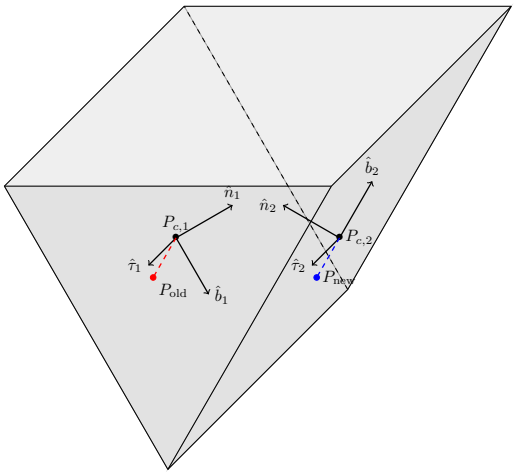

Figure 4.8. Translation of application point for wedge boundary condition.

In a generic case (see Fig. 4.8), the ray rotation is performed employing the face reference frames defined in the previous section. The impinging ray $\hat{\mathbf{s}}^{\text{old}}$ is expressed in the local reference frame of the inlet face (face 1 in the Fig. 4.7)

$$ {}^1\hat{\mathbf{s}}^{old} = {}_1R^{-1}\hat{\mathbf{s}}^{\text{old}} $$

In an axisymmetric configuration the local reference frames of faces 1 and 2 are such that ${}^2\hat{\mathbf{s}}^{\text{new}}$ can be expressed inverting the sign of the n and b components

$$ {}^2\hat{\mathbf{s}}^{\text{new}} = \begin{bmatrix} {}^1s_\tau^{\text{old}} \\ -{}^1s_b^{\text{old}} \\ -{}^1s_n^{\text{old}} \end{bmatrix} $$

Finally, the new ray in the cartesian reference frame is obtained as

$$ \hat{\mathbf{s}}^{\text{new}} = {}_2R^2\hat{\mathbf{s}}^{\text{new}} $$

Concerning the application point, first of all the position vector of the impinging point P_{old} in the local reference frame, measured from the face center, is computed

$$ {}^1\mathbf{P}_{\text{old}} = {}_1R^{-1}(\mathbf{P}_{\text{old}} - P_{c,1}) $$

The new application point, expressed in the reference frame of face 2, can be computed inverting the sign of the second component of ${}_1P^{\text{old}}$

$$ {}^2\mathbf{P}_{\text{new}} = \begin{bmatrix} {}^1P_{\text{old},\tau} \\ -{}^1P_{\text{old},b} \\ 0 \end{bmatrix} $$

To go back to cartesian coordinates a final roto-translation is performed

$$\mathbf{P}_{\text{new}} = \mathbf{P}_{c,2} + {}_2R^2\mathbf{P}_{\text{new}}$$

4.3 RTE integration

Once the ray tracing procedure is completed the RTE needs to be integrated on the ray. In order to do so, the length of each segment traveled by the ray and the radiative properties in the respective cell have to be stored into memory. The RTE is then integrated backwards (see Fig. 4.4) along the ray. Depending on the spectral model, the discretized RTE is written in different forms, which are reported in this section for the sake of completeness.

Spectral RTE (LBL/SNBW)

If the adopted spectral model is such that the absorption coefficient is defined, the following recursive form is employed (for isotropically scattering medium)

$$\mathcal{I}_\eta^{i+1} = \mathcal{I}_\eta^i e^{-\beta_\eta \Delta s^i} + S^i \left(1 - e^{-\beta_\eta \Delta s^i}\right) \tag{4.8}$$

As reported in Sec. 3.1, $\beta_\eta = \kappa_{\text{abs},\eta} + \kappa_{\text{sca},\eta}$ is the extinction coefficient and the source function S is

$$S^i = \frac{\mathcal{I}_{b,\eta} + \omega_\eta/(4\pi) G_\eta}{1 + \omega_\eta} \tag{4.9}$$

where $\omega_\eta = \kappa_{\text{sca},\eta}/(\kappa_{\text{abs},\eta} + \kappa_{\text{sca},\eta})$ is the scattering albedo and

$$G_\eta = \int_\Omega \mathcal{I}_\eta d\Omega$$

it the impinging intensity. The index i goes from 0 to the number of steps along the ray and Δs is the path traveled by the ray inside a cell.

The initial intensity $\mathcal{I}_\eta^0$ is computed assuming gray and diffuse walls as

$$\mathcal{I}_{\eta,\text{wall}} = \varepsilon_{\text{wall}} \mathcal{I}_{b,\eta} - (1 - \varepsilon_{\text{wall}}) q_\eta^{\text{imp}}/\pi \tag{4.10}$$

where q_η^{imp} is the incident wall radiative heat flux.

Gray gas

For the gray gas model the RTE form is the same, but the mean–Planck properties are employed instead of the spectral ones.

SLW/WSGG

For the WSGG class of models the RTE has to be modified to include the gray gas weights a_{i_g}. For the sake of simplicity only the non-scattering form is reported:

$$\mathcal{I}_{i_g}^{i+1} = \mathcal{I}_{i_g}^i e^{-\kappa_{\text{abs},i_g} \Delta s^i} + S^i \left(1 - e^{-\kappa_{\text{abs},i_g} \Delta s^i}\right) \tag{4.11}$$

where

$$S^i = a_{i_g} \mathcal{I}_b \tag{4.12}$$

Also the boundary condition is slightly modified in

$$\mathcal{I}_{i_g,\text{wall}} = \varepsilon_{\text{wall}} a_{i_g} \mathcal{I}_b - (1 - \varepsilon_{\text{wall}}) q_{i_g}^{\text{imp}} / \pi \tag{4.13}$$

SNB

For the SNB model the RTE has to be recast in its integral form, since the model yields the transmissivity and not the absorption coefficient. The integral form of the spectral RTE can be expressed as

$$\mathcal{I}_\eta(L) = \mathcal{I}_\eta(0)\tau_\eta(0 \to L) + \int_0^L - \left[\frac{d\tau_\eta(0 \to s')}{ds'}\right] \mathcal{I}_{b,\eta} ds'$$

where $\tau_\eta(0 \to s)$ is the transmissivity of the medium between $s = 0$ and $s = L$

$$\tau_\eta(0 \to s) = \exp\left[-\int_0^s \kappa_{\text{abs},\eta}(s'') ds''\right]$$

When using a narrow-band model, one computes the integral intensity as

$$\mathcal{I}(L) = \sum_{n=1}^{N_b} \overline{\mathcal{I}}_n(s)$$

where N_b is the number of bands in which the spectrum is divided and the $\overline{()}$ symbol indicates the average over the n^{th} narrow band

$$\overline{\mathcal{I}}_n = \frac{1}{\eta_{2,n} - \eta_{1,n}} \int_{\eta_{1,n}}^{\eta_{2,n}} \mathcal{I}_\eta d\eta$$

The integral form of the RTE for the average spectral intensity can be obtained averaging the spectral equation

$$\bar{\mathcal{I}}_n(L) = \overline{\mathcal{I}_\eta(0)\tau_\eta(0 \to L)} + \int_0^L - \overline{\left[\frac{d\tau_\eta(0 \to s')}{ds'}\right] \mathcal{I}_{b,\eta}} ds'$$

The main challenge in solving the above equation is the fact that the average transmissivity $\overline{\tau}$ does not appear alone, but always multiplied by a spectral intensity. To avoid taking into account the correlation between intensity and transmissivity, it can be recognized that $\mathcal{I}_{b,\eta}$ is a smooth function of the frequency, and therefore

$$\overline{a\mathcal{I}_{b,\eta}} \approx \overline{a}\,\overline{I\mathcal{I}}_{b,\eta}$$

where a is a generic function of the wavenumber. If we assume also that the intensity at the start of the column is due only to wall emission, then $\mathcal{I}_\eta(0) = \mathcal{I}_{b,\text{wall},\eta}$ and the same reasoning can be applied, obtaining

$$\overline{\mathcal{I}}_n(L) = \overline{\mathcal{I}}_{w,\eta} \overline{\tau_\eta(0 \to L)} + \int_0^L - \left[\frac{d\overline{\tau_\eta(0 \to s')}}{ds'}\right] \overline{\mathcal{I}}_{b\eta} ds'$$

where the averaging operator has been moved inside the derivative. The integral can be approximated as a sum over all the N column segments (each assumed homogeneous and isothermal)

$$\overline{\mathcal{I}}_n(L) = \overline{\mathcal{I}}_{w,\eta}\overline{\tau_\eta(0 \to L)} + \sum_{k=0}^{N} - \left[\frac{d\overline{\tau_\eta(0 \to s)\tau}_n}{ds'}\right]\Bigg|_{s'=s^k} \overline{\mathcal{I}}^k_{b\eta}$$

and use a finite difference scheme to approximate the derivative of the trasmissivity

$$\overline{\mathcal{I}}_n(L) = \overline{\mathcal{I}}_{w,\eta}\overline{\tau_\eta(0 \to L)} + \sum_{k=0}^{N} \left(\overline{\tau_\eta(0 \to L_{k-1/2})} - \overline{\tau_\eta(0 \to L_{k+1/2})}\right) \overline{\mathcal{I}}^k_{b\eta} \tag{4.14}$$

where we have employed the $i \pm 1/2$ notation to identify the boundaries between segments, being the trasmissivity a nodal quantity. Equation (4.14) is the one employed in the DTM tool.

Concerning the column transmissivity, it has to be recalled that the classical SNB expression

$$\tau_\eta(s' \to s) = \exp\left[-\frac{\beta_\eta}{\pi}\left(\sqrt{1 + \frac{2\pi u \kappa_\eta}{\beta_\eta}} - 1\right)\right], \quad u = \int_{s'}^{s} x_i p ds''$$

is valid for an isothermal and homogeneous column with a single participating species. In any practical combustion application one has to deal with multiple species and non-homogeneous media. The former challenge is solved computing the total transmissivity as the product of the one of the single species, while to overcome the latter it is custom to resort to the Curtis-Godson approximation [102]. This model keeps the SNB formulation unchanged, but substitutes κ and β with equivalent parameters

$$\kappa_{\text{eq}} = \frac{1}{u}\int_{s'}^{s} x_i p \kappa ds''$$

$$\beta_{\text{eq}} = \frac{1}{u\kappa_{\text{eq}}}\int_{s'}^{s} x_i p \kappa \beta ds''$$

4.4 Numerical implementation of the DTM

The following algorithm summarizes the main computational steps of DTM as implemented in the present work. The procedure closely follows the theoretical framework described in the previous sections: for each boundary face, a set of discrete directions (ϕ, θ) is defined according to the chosen angular resolution, and rays are traced through the computational domain to evaluate the radiative intensity field $\mathcal{I}$ by integrating the RTE along each path. The resulting wall heat flux q_{wall} and the volumetric radiative source terms $\dot{Q}_{\text{rad}}$ are then assembled from the directional intensities. For brevity, the internal details of the ray tracing and RTE integration routines are omitted here, while their mathematical formulation is provided in the previous sections.

The algorithm for the computation of $\nabla \cdot q$ is not reported for the sake of brevity, since it is very similar to the one for the heat transfer calculations and the angular grid differences have already been underlined in Sec. 4.1.

Due to the high computational cost associated with grid size and number of rays or spectral bands, the DTM solver was parallelized using the `OpenMP` framework. In principle, three different levels of parallelization can be adopted: (i) domain-based, where each computational block or subset of cells is handled by a separate thread; (ii) spectral-based, where different wavelength bands are processed in parallel; and (iii) ray-based, where the integration of each discrete direction is performed independently. In the present implementation, the third approach was chosen, since each ray can be traced and integrated independently of the others, with no data dependency or communication overhead. This strategy provides good scalability with the number of available threads, as the computational workload is evenly distributed among the rays. Only a reduction operation is required at the end of the parallel region to assemble the total wall flux and source terms. This design allows the DTM solver to efficiently exploit shared-memory architectures.

Algorithm 1: Discrete Transfer Method for Radiative Heat Flux Computation

Input: Temperature, species and pressure fields from CFD.
Output: Radiative wall heat flux q_{wall}.

Initialization:
Set $q_{\text{wall}} = 0$.
Define angular discretization $\{(\phi_{i_\phi}, \theta_{i_\theta})\}$ for N_r rays.

foreach *block in the domain* **do**
  foreach *boundary face* f **do**
    Compute local-to-global rotation matrix ${}_fR$.
    Identify wall point $\mathbf{P}_{\text{wall}}$ at the center of face f.
    foreach *direction* $(\phi_{i_\phi}, \theta_{i_\theta})$ **do**
      Compute ray direction in Cartesian frame:
      $\hat{\mathbf{s}} = {}_fR\,[\cos\theta_{i_\theta}\cos\phi_{i_\phi},\ \cos\theta_{i_\theta}\sin\phi_{i_\phi},\ \sin\theta_{i_\theta}]^T$.
      Trace the ray starting from $\mathbf{P}_{\text{wall}}$ through the domain, storing all traversed cells and segment lengths Δs^i.
      Integrate the RTE backward along the ray to obtain the impinging intensity $\mathcal{I}(\hat{\mathbf{s}}, \mathbf{P}_w)$.
      Update the wall heat flux on face f:

$$q_{\text{wall}} \mathrel{+}= \mathcal{I}(\hat{\mathbf{s}}, \mathbf{P}_{\text{wall}}) \cos(\theta_{i_\theta})\, \Delta\Omega$$

      where $\Delta\Omega$ is the solid angle weight of the ray.
    end
  end
end

Post-processing:
Average q_{wall} over all directions and, if applicable, spectral bands.

An example of parallel scalability is shown in Fig. 4.9 for an Intel(R) Xeon(R) W-2265 CPU. The test case is the same of Sec. A1.1. The normalized CPU time decreases nearly inversely with the number of threads up to 12, indicating good parallel efficiency across the physical cores. Beyond this point, performance saturates as the code enters the hyper-threading regime, where threads share computational

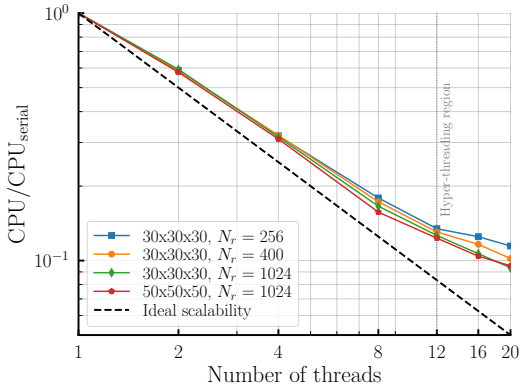

Figure 4.9. Scalability test on a Intel(R) Xeon(R) W-2265 CPU @ 3.50GHz.

resources on the same core, leading to reduced scalability. Overall, the results demonstrate efficient OpenMP parallelization up to the limit of physical cores.

Part II

Results

Chapter 5

Liquid rocket engines

This chapter demonstrates the critical role of non-gray gas radiation in LREs by comparing high-fidelity spectral models with reduced approaches. Two tailored WSGG models, specifically optimized for LOX/LH_2 and LOX/LCH_4 combustion products, are developed and validated. Furthermore, a simplified 1D modeling approach is introduced, enabling an accurate estimation of radiative heat loads at a significantly lower computational cost compared to full multi-dimensional simulations, thus providing a practical tool for preliminary design and parametric studies.

Contents

In this chapter the issue of gas radiation modeling in LREs is thoroughly discussed, with the aim of proposing a set of computationally effective models that can be employed for the evaluation of the radiative wall heat flux. Although solid particles are strong radiation emitters and carbon particles are known to contribute significantly to the radiative heat load in oxygen–hydrocarbon engines [34, 35], radiation by soot is not considered here since the main issues with soot modeling are not

linked to its radiative properties but rather to the quantification of its concentration and are outside the scope of this work.

In Section 5.1 high-fidelity spectral approaches (such as line-by-line and statistical narrow-band) are adopted to compute total emissivities of LOX-LH_2 combustion products, and a weighted sum of gray gas model specifically tailored for high temperatures and pressures is subsequently obtained. The results are also compared to the ones yielded by the SLW model, the gray gas approach, and two WSGGs taken from the literature [116, 117], to underline the effect of the model calibration range on the computed emissivities. Moreover, the radiation models of popular tools employed by the industry for engine preliminary design, such as EcosimPro [118] and RPA [119], are also included in the comparison. The new WSGG model is then applied to full engine test cases employing the discrete transfer method. In Section 5.2 the same procedure is applied to LOX-LCH_4 combustion products, with the derivation of a WSGG model for H_2O-CO_2 mixtures, readily applicable also to other propellant combinations with hydrocarbon fuels. Finally, Sec. 5.3 presents the development a reduced order model for the estimation of the radiative heat flux in LREs, coupling quasi-1D chemical equilibrium computations, the WSGG models derived in Sec. 5.1 and 5.2, and semi-analytical expressions for radiation heat flux in planar and axisymmetric geometries.

5.1 Radiation modeling in oxygen–hydrogen engines

The goal of this section is to assess the performance of the gas radiation models described in Chapt. 3, to develop a new WSGG specifically tailored for oxygen–hydrogen LREs and to assess its capabilities on relevant test cases. A specific section is dedicated to this propellant combination due to the fact that its combustion products contain only one radiative participating species, H_2O, while any mixture resulting from hydrocarbon combustion should take into account also CO_2 and CO.

5.1.1 Effect of participating species

Typical LOX-LH_2 combustion products are mainly composed by H_2O, H_2, O_2 and OH, which account for more than 95% of the total molar mass. Among them H_2 and O_2 can typically be considered as transparent, since symmetric molecules do not usually participate to radiation heat transfer [7], and OH is a weaker radiator than H_2O and has a much lower molar fraction. As an example, Fig. 5.1 reports the absorption coefficients, already multiplied by pressure and molar fraction, for H_2O and OH as the equilibrium combustion products of oxygen and hydrogen at 100 bar and $OF = 6$ as given by NASA CEA [74], showing clearly how the contribution by OH is negligible when compared to the one of H_2O. For this reason, while OH radiation is often employed for diagnostic purposes [120], it is not relevant from the heat transfer standpoint, and radiative computations in oxygen–hydrogen engines can be performed considering H_2O as only participating species.

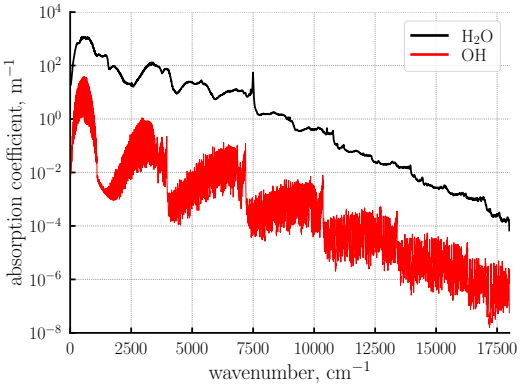

Figure 5.1. Absorption coefficients for oxygen–hydrogen combustion products at 100 bar and $OF = 6$ ($T = 3523.79$ K, $x_{H_2O} = 0.673$, $x_{OH} = 4.21 \times 10^{-2}$).

5.1.2 Total emissivity comparison

In this section a parametric analysis has been performed in order to evaluate the total emissivity of LOX-LH_2 combustion products for different lengths, pressures, and mixture ratios and to assess the predictive capabilities of the models. LBL solutions are employed as reference, given that accurate measurements of emissivity in the temperature and pressure range typical of LREs are not available. As stated in Sec. 3.2.1, the calculations are performed with the HITEMP 2010 database and the *Voigt* line profile. A line cut off threshold of $1{\times}10^{-28}$ cm^{-1}/(molecule $\cdot$ cm^{-2}) has been chosen, after performing a convergence analysis in the temperature range of interest. The line truncation width η_{trunc} may show a dependence on pressure and temperature, as shown in [97, 121], and general cut-off criteria are provided in [121] for both H_2O and CO_2. For the sake of simplicity, a fixed cut off half width $\eta_{\text{trunc}} = 1500$ cm^{-1}, chosen after performing a convergence analysis at both high and low pressure (10 bar, 300 bar) and temperatures (300 K, 4000 K), has been used in this work.

The mixture equilibrium compositions and temperatures have been evaluated with the NASA CEA code [74] for 5 values of pressure (20, 50, 100, 200 and 300 bar), two values of length (0.1 and 1 m), and 20 values of equivalence ratio ($OF_{\text{stoichiometric}}/OF$) equispaced between 0.1 and 2. Figure 5.2 reports the emissivity computed for various pressure path lengths and oxidizer to fuel ratios with the LBL and SNB models. It can be seen that the two models are in extremely good agreement, with a maximum deviation of $\approx$2%. This confirms that the SNB model may be employed as a reference solution for LRE applications. Figure 5.2 also shows how the emissivity increases with the optical thickness of the medium, and thus with pressure and length, and decreases with temperature (the maximum temperature is reached around stoichiometric conditions).

Based on the aforementioned results, the SNB model is adopted as reference, and the performance of several simplified models available in the literature are tested:

- SLW model [105], calibrated for $T \in [300, 3000]$ K and $p \in [0.1, 50]$ atm.
- Two WSGGs taken from the literature, chosen because of their relatively wide

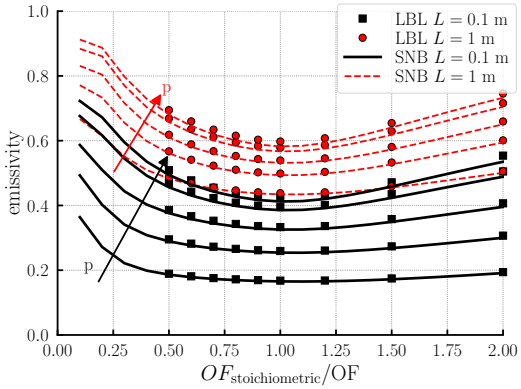

Figure 5.2. Comparison of LBL and SNB emissivities for $p = 20, 50, 100, 200, 300$ bar.

range of application, reported in Table 5.1 (to the author's knowledge, no WSGG currently available in the literature has a calibration range wide enough to cover the high pressure and temperatures typical of LRE conditions).

Table 5.1. Validity range of selected WSGG models.

Model	T (K)	x_{H_2O}/x_{CO_2}	p or pL	Ref.
Shan	500-2500	0.125-4	1-30 (bar)	[116]
Bordbar	500-2400	0-∞	0.01-60 (atm · m)	[117]

- Gray gas model, with mean Planck absorption coefficient computed from the SNB data [101].

- Engineering correlations:

  – The *Barrere* model, employed in the EcosimPro/ESPSS framework for LRE design [118] and originally from [122]

$$q_{H_2O} = 4.07(px_{H_2O})^{0.8} L_{\text{eff}}^{0.6} \left[\left(\frac{T_{\text{ad,wall}}}{100} \right)^3 - \left(\frac{T_{\text{wall}}}{100} \right)^3 \right] \tag{5.1}$$

$$q_{CO_2} = 4.07 \left(px_{CO_2} L_{\text{eff}} \right)^{0.33} \left[\left(\frac{T_{\text{ad,wall}}}{100} \right)^{3.5} - \left(\frac{T_{\text{wall}}}{100} \right)^{3.5} \right] \tag{5.2}$$

  where L_{eff} is an effective length, representative of the mean line of sight of the combustion chamber, and $T_{\text{ad,wall}}$ is the adiabatic wall temperature. The total radiative heat flux is computed as the sum of the two contributions and the emissivity can be evaluated as $\varepsilon = q(T_{\text{wall}} = 0)/(\sigma T^4)$. Similar expressions available in the literature, such as the ones reported in [123], are not considered here.

  – The wide–band model implemented in the RPA design code, which yields the total emissivity for mixtures containing H_2O, CO_2, CO (and other

species if needed)

$$\varepsilon = \sum_{\text{molecules}} \sum_{\text{bands}} \beta_j \left[1 - \exp\left(-\kappa_{i,j} p x_j L\right)\right] \frac{\mathcal{I}_{\Delta\eta_{i,j}}}{\sigma T^4} \qquad (5.3)$$
$$j = 1, .., N_{\text{molecules}},\ i = 1, .., N_{\text{bands}}$$

where $\mathcal{I}_{\Delta\eta_{i,j}}$ is the integral of the black–body Planck function over the width $\Delta\eta$ of band j of molecule i and $\kappa_{i,j}$, β_j and $\Delta\eta_j$ are tabulated values.

The emissivities are compared in Fig. 5.3(a) for two different pressure path lengths. For the low pressure case, both SLW and WSGG are able to closely follow the SNB emissivity as long as the mixture temperature is inside their validity range (3000 K for SLW, 2400 K for *Bordbar* and 2500 K for *Shan*), but lead to significant errors at higher temperatures which, however, are the ones obtained at OF values of practical interest. For the high pressure case, a similar behavior is shown by the SLW and *Bordbar* models. The *Shan* WSGG shows instead a good agreement with SNB data for 300 bar and near-stoichiometric conditions, despite pressure and temperature are both outside their respective range (1-30 bar, 500-2500 K). This is due to error cancellation caused by underestimation of ε for $p > 30$ bar and overestimation of ε for $T > 2500$ K. This shows how the application to LRE conditions of models not specifically obtained for high temperatures and pressures can lead to a substantial error in the estimation of the combustion products emissivity. In both cases the gray gas approximation yields values which are much higher than the SNB ones, especially for higher pressures. This is consistent with the fact that the error induced by the gray gas approximation is small for optically thin conditions, due to the low importance of absorption, which is captured by the spectral models. Similar conclusions can be drawn by Fig. 5.3(b), which compares the emissivities for all the points of the test matrix. It can be seen that none of the tested models yield satisfactory results, with errors consistently higher than 30% in many cases. It must be noted that the wide band approach offers a good agreement with the narrow band one, with the exception of optically thick conditions, where it underpredicts the emissivity. For what concerns the *Barrere* model, its performance is quite poor, with predicted emissivities exceeding 1. These results remark that models requiring calibration need to be employed only in the very specific range where they were obtained.

Given that none of the reduced models tested here offers satisfactory results, and because the computational cost of the SNB model in practical test cases can be substantial, a novel WSGG has been obtained, adopting the following formulation (similar to the one reported in [117])

$$\varepsilon = \sum_{i_g=1}^{N_g=4} a_{i_g}(T) \left[1 - \exp\left(-\kappa_{i_g} x_{\mathrm{H_2O}} p / p_0 L\right)\right]$$
$$a_{i_g}(T) = c_{0,i_g} + c_{1,i_g}\left(\frac{T}{T_{\text{ref}}}\right) + c_{2,i_g}\left(\frac{T}{T_{\text{ref}}}\right)^2 + c_{3,i_g}\left(\frac{T}{T_{\text{ref}}}\right)^3 \qquad (5.4)$$

where $p_0 = 1$ bar and $T_{\text{ref}} = 2400$ K. The value of the reference temperature was chosen, as done in [116], to optimize the goodness of the polynomial fit. The a_{i_g} and

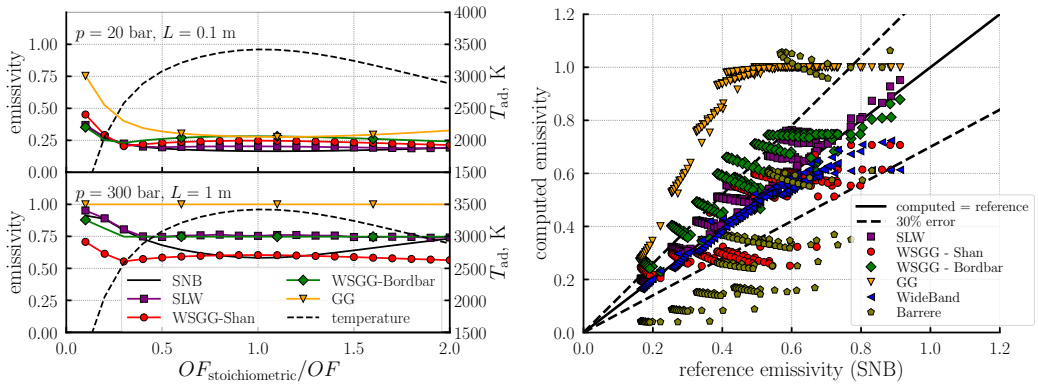

(a) (b)

Figure 5.3. Performance of models available in the literature versus SNB.

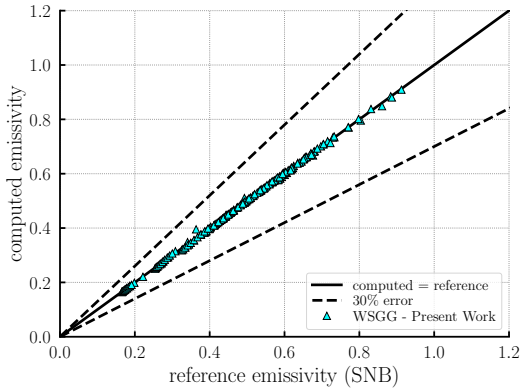

Figure 5.4. Performance of new WSGG model versus SNB.

κ_{i_g} coefficients have been fitted on SNB emissivities obtained for temperatures from 1500 K to 4000 K, pressures from 1 bar to 300 bar, H_2O molar fractions ranging from 0.1 to 1.0, lengths from 10^{-4} m to 1 m. The coefficients have been optimized to reduce the error in typical combustion chamber conditions and are reported in Appendix A2. It has been chosen to limit the temperature and pressure range in order to be able to increase the model performance without the need for additional terms in the polynomials.

The emissivities predicted by the new WSGG are compared with the SNB ones in Fig. 5.4, with a mean absolute percentage error of 0.6%.

5.1.3 Application to LRE thrust chambers

In this section the gas radiation models discussed above are applied to LRE test cases. The main goal of this analysis is the assessment of the errors induced by the global radiation models (WSGG, SLW, gray gas) and by the weak absorption limit approximation of the SNB model (SNBW, Eq. (3.16)) in practical scenarios.

Two oxygen–hydrogen engines are selected, the SSME and the DLR subscale combustion chamber model “E" [124] (which will be referred to as BKE). Details on

the test cases are reported in Table 5.2. For both combustion chambers reference CFD solutions previously obtained by the authors are available and described in [21, 125]. The numerical approach is based on axisymmetric RANS simulations, with finite-rate chemistry and the Spalart-Allmaras turbulence model. It is thoroughly described in [21, 125] and its details are not repeated here for the sake of brevity, since no coupling with the CFD computations has been performed. In fact, as shown in [31], the temperature flowfield of LREs is not significantly influenced by the coupling with the radiative source term. Both combustion chambers are simulated neglecting the details of the injector plate, and injecting equilibrium combustion products over the entire entrance section (an approach that will be referred to as CPI, combustion product injection). While this simplifying assumption leads to an overestimation of both convective and radiative heat transfer in the first part of the chamber, it is deemed acceptable here, since the main goal of this work is assess the performance of the discussed models. Moreover, it has been shown in [82, 125, 126] how the adopted approach yields satisfactory results sufficiently far from the injection plate and at the nozzle throat, which is usually the most critical region from the heat transfer standpoint.

Table 5.2. Oxygen–hydrogen test case data.

Test case	throat radius, cm	length[a], cm	pressure, bar	OF	T_{wall}, K
SSME	13.1	10	208.74	6	754
BKE	1.65	26.0	116.2	6	450-750

[a]Only the cylindrical part of the chamber is considered.

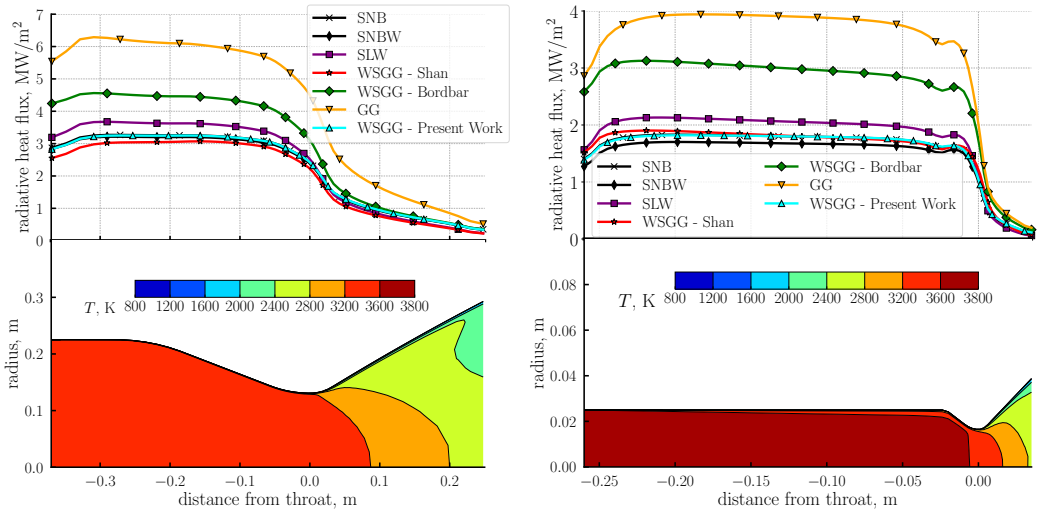

(a) SSME.

(b) BKE.

Figure 5.5. Comparison of gas radiation models on oxygen–hydrogen test cases.

For both test cases the DTM algorithm is employed with $N_r = 256$ and $\varepsilon_{\text{wall}} = 0.7$. The SNB model is here considered as reference, as done in the previous section, since LBL calculations have a huge computational cost, and, as shown in Fig. 5.2, they

are in very good agreement with SNB ones. The results are reported in Fig. 5.5. For what concerns the SNBW approach, in both test cases a very good agreement with the full SNB is retained. On the other hand, the gray gas approximation significantly overestimates the heat flux, as shown in the emissivity comparison of Fig. 5.3. Among the global models, the one with validation range closest to LRE conditions is the SLW, which overestimates the peak heat flux by 16.5% and 12.4% in the BKE and SSME respectively. The *Bordbar* WSGG also predicts a higher heat flux, with an error on the peak value of 70.9% (BKE) and 39.5% (SSME). The *Shan* model shows instead good performance in both test cases, despite being calibrated up to 2500 K and 30 bar. Such results are consistent with the behavior reported in Fig. 5.3(a), namely that for high pressure path lengths and $OF/OF_{\text{stoichiometric}} = 0.75$ (valid for both BKE and SMME) the *Shan* WSGG is in good accordance with spectral emissivities. However, this does not ensure predictive capabilities of the model for generic LRE conditions. In fact, for the same OF, but lower pressure path length, the emissivity is overestimated by 25% (Fig. 5.3(a)). Finally, the WSGG proposed in this work closely follows the SNB results, with a deviation on the peak heat flux of 0.54 % and 0.6% for the BKE and SSME cases respectively. On the basis of this analysis, it can deduced that the application of a global radiation model (WSGG or SLW) not explicitly validated for LRE conditions to LRE test cases can yield heat fluxes significantly different from the ones obtained with spectral models. Some of the models existing in the literature may show an agreement with high fidelity approaches, but not with enough consistency to allow their use reliably for generic LRE conditions.

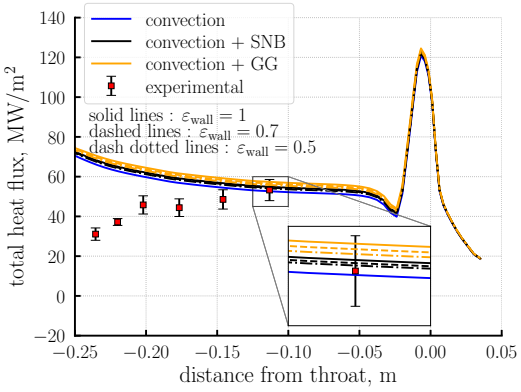

Figure 5.6. Comparison of numerical and experimental data for the BKE test case.

Additional considerations may be done comparing the total computed heat flux with the experimental data which is available for the BKE test case, reported in Fig. 5.6. Three values of wall emissivity are considered (0.5, 0.7, and 1) to cover the expected range for the emissivity of oxidized metals that make up the surface material [31]. The aim of this discussion is not to validate the proposed models, but to provide the elements for a more quantitative analysis of the effect of the choice of the radiative heat transfer model on the overall heat flux. In fact, thorough validation of any radiative heat transfer model can be performed only with custom measurements, either of emissivity in lab conditions or of radiative heat flux on

representative test cases. Such measurements are unfortunately not available in the literature for LRE conditions. The results of Fig. 5.6 show that although the radiative share of the overall heat flux is small, such that the convective contribution alone is inside the experimental error band at the end of the cylindrical part of the chamber, the gray gas radiation, especially with high wall emissivity, is likely overestimated, shifting the total heat flux almost outside the error band, while all SNB results are extremely close to the experimental data. The simplifying assumptions of the CFD simulations employed here, in particular those regarding the modeling of the injector plate, lead to an heat flux profile which is significantly different from the experimental one in the first part of the chamber. However, such differences are expected and are the outcome of a precise modeling choice, which aims at reducing the computational complexity of the domain. It has been shown in [82, 126, 127] how the approach employed here yields reasonable results far from the injection zone for both the convective and radiative heat fluxes. Moreover, a detailed discussion of the effects of the injection plate modeling on the radiative heat flux profile is outside the scope of this work, and the interested reader is referred to [126].

Finally, it may be of interest to compare the computational cost of the various algorithms. For this analysis the SSME test case with black walls was selected and all simulations were performed on a single Intel(R) Xeon(R) W-2265 CPU @ 3.50GHz. The results are reported in Table 5.3. The reference CFD grid was made of 50×45 cells and the heat flux was computed for all boundary points with 256 rays. The computational cost is mostly driven by the ray tracing procedure and, in minor part, by the spectral integration of the RTE. For this analysis, ray tracing is not repeated for each spectral point, allowing to compare only the portion of the computational cost due to the spectral integration.

The gray gas approximation has the lowest computational cost, since no spectral integration is performed. The WSGG and SNBW models increase the computational time since the RTE has to be integrated for each gray gas or spectral band (4 gray gases for WSGG and 450 bands for SNB and SNBW). The full SNB approach leads to a significant increase of computational time, since it does not allow to precompute and store the values of absorption coefficients, but it requires to recompute the transmissivity for each ray traversing a cell.

Table 5.3. Comparison of CPU times for the SSME test case with black walls.

Model	SNB	SNBW	WSGG	GG
CPU time (s)	1739.59	83.77	4.46	3.55
$\frac{\text{CPUtime}}{\text{CPUtime(GG)}}$	490.02	23.56	1.256	-

5.2 Radiation modeling in oxygen–methane engines

In this section the same procedure of Sec. 5.1 is applied to the oxygen-methane propellant combination. It has been chosen to dedicate a section to this propellant combination because of the large number of new LOX-LCH$_4$ LREs being currently

developed [128–130] and because its results can be easily extended to other propellant combinations comprising H_2O, CO_2 and CO among its combustion products.

5.2.1 Effect of participating species

Before analyzing the performance of the various models in the prediction of the propellant emissivity, it is useful to assess the relative importance of the three main radiating species present in oxygen–hydrocarbon combustion, namely water vapor, carbon dioxide, and carbon monoxide (as discussed before OH is neglected). Figure 5.7(a) reports the LBL spectrum of LOX-LCH_4 combustion products at 100 bar and $OF = 3.4$. The equilibrium conditions, according to CEA, are $T_{ad} = 3598.3$ K, with the following main radiating species molar fractions $x_{H_2O} = 0.408$, $x_{CO_2} = 0.263$ and $x_{CO} = 0.229$. It can be seen how the resulting spectrum is mainly driven by water vapor, with a smaller contribution given by CO_2 and CO. A convergence analysis on the line cut off threshold and the cut off width has been repeated, and the same values used for H_2O calculations have been employed (Sec. 5.1.2). Furthermore, as done for hydrogen-oxygen engines, all LBL calculations are performed with the *Voigt* profile, because of the negligible effect of the collisional line profile on the total emissivity. A more extensive comparison is performed in Fig. 5.7(b), where 200 total emissivities of LOX-LCH_4 combustion products are computed with the SNB model in the range $p \in [20, 300]$ bar, $OF_{\text{stoichiometric}}/OF \in [0.1, 2]$, $L \in [0.1, 1]$ m, taking into account different combinations of radiating species. The reference values are the ones obtained considering H_2O, CO_2 and CO. The results show that carbon monoxide may be safely neglected and also that a reasonable error is introduced by taking into account only H_2O. On the basis of this analysis, the results reported in the following sections will be obtained neglecting the presence of carbon monoxide, except that for the LBL ones.

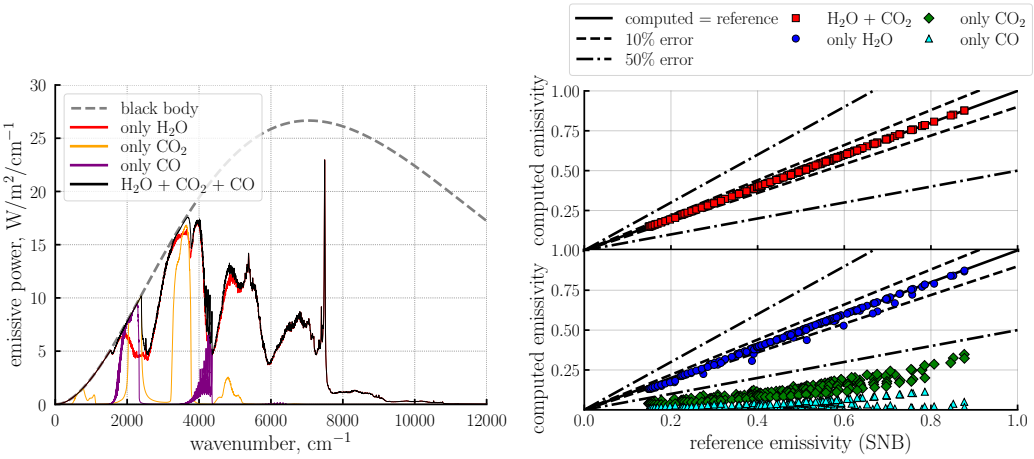

(a) Spectrum of LOX-LCH_4 combustion products for $p = 100$ bar, $OF = 3.4$ and $L = 0.5$ m.

(b) Effect of radiating species on total emissivity of LOX-LCH_4 combustion products.

Figure 5.7. Effect of radiating species of LOX-LCH_4 emission.

5.2.2 Total emissivity comparison

As done for oxygen–hydrogen engines, LBL and SNB emissivities are compared in Fig. 5.8, showing once more a good agreement for all tested conditions.

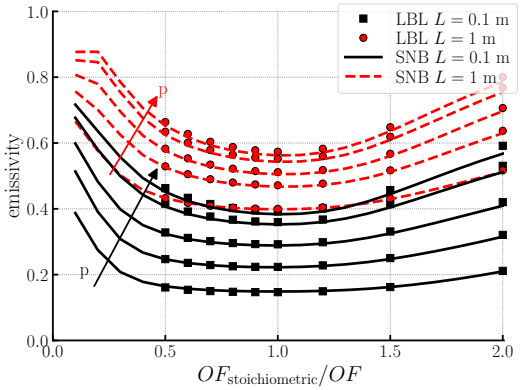

Figure 5.8. Comparison of LBL and SNB emissivites for LOX-LCH$_4$ combustion products.

The performances of all available models are reported in Fig. 5.9(a). It can be seen once more how the GG approach is unable to yield reliable results, significantly overestimating the emissivity. The *Shan* and *Bordbar* models show a better agreement with SNB results, but are still significantly scattered. The *Barrere* model confirms its poor performance, and the wide-band one yields worse results than for oxygen–hydrogen engines, suggesting how there may be a misrepresentation of the radiative contribution by CO_2. Given that none of the available reduced–order models yields satisfactory results, a new WSGG model is proposed, adopting the following formulation (following [116])

$$\begin{aligned} \varepsilon &= \sum_{i_g=1}^{N_g=4} a_{i_g}(T, Mr)\left[1 - \exp\left(-\kappa_{i_g}(Mr)(x_{\mathrm{H_2O}} + x_{\mathrm{CO_2}})p/p_0 L\right)\right] \\ a_{i_g}(T) &= c_{0,i_g} + c_{1,i_g}\left(\frac{T}{T_{\mathrm{ref}}}\right) + c_{2,i_g}\left(\frac{T}{T_{\mathrm{ref}}}\right)^2 + c_{3,i_g}\left(\frac{T}{T_{\mathrm{ref}}}\right)^3 \end{aligned} \tag{5.5}$$

where $p_0 = 1$ bar and $T_{\mathrm{ref}} = 2300$ K. In order to take into account the dependence from $x_{\mathrm{H_2O}}$ and $x_{\mathrm{CO_2}}$, different fits have been obtained for $Mr = x_{\mathrm{H_2O}}/x_{\mathrm{CO_2}} = 0.125, 0.25, 0.5, 0.75, 1, 2, 2.5, 3, 4, 6, 8$, in order to cover all possible OF values in the range of interest. The coefficients have been fitted on SNB emissivities for pressures from 1 to 300 bar, temperatures from 1000 K to 4000 K and lengths from 10^{-4} to 1 m, and are reported in Appendix A2. The results of Fig. 5.9(b) show that the proposed WSGG yields emissivity in very good agreement with the reference results, with a mean absolute percentage error 0.98% in typical combustion chamber conditions.

5.2.3 Application to LRE thrust chambers

The SNB, SNBW, SLW, WSGG, and GG models are now applied to two test cases, a high performance engine (HPE) inspired to the Raptor engine [131] and the LOX-

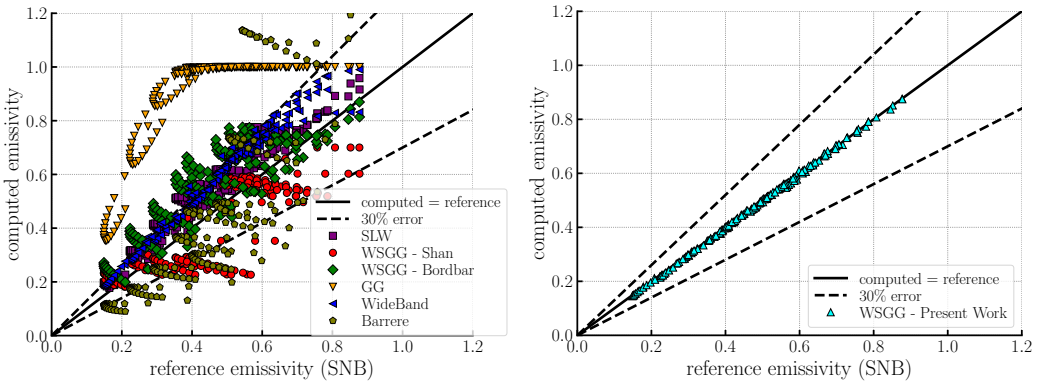

(a) Models available in the literature.

(b) New WSGG.

Figure 5.9. Models performance versus SNB.

CH_4 DLR subscale combustion chamber model "B" (BKB) [125]. Relevant engine data is reported in Table 5.4. Both engines have been previously analyzed by the authors, with the same numerical approach described in Sec. 5.1.3.

Table 5.4. Oxygen–methane test case data.

Test case	throat radius, cm	length[a], cm	pressure, bar	OF	T_{wall}, K
HPE	22.16	10	250	3.6	900
BKB	2.5	25.0	10.0	3.34	400-418

[a]Only the cylindrical part of the chamber is considered.

The radiative wall heat fluxes are reported in Fig. 5.10 for both test cases, together with their temperature flowfield. Results are obtained with $N_r = 256$ and $\varepsilon_{\text{wall}} = 0.7$. The SNBW, GG, SLW, and *Bordbar* models behave qualitatively the same as in the LOX-H2 test cases of Sec. 5.1.3, always overestimating the heat flux. In the HPE test case the peak heat flux is overestimated by 0.11%, 37.28%, 52.60%, 110.58%, and 11.58% by the SNBW, SLW, *Bordbar*, gray gas, and *Shan*, respectively. The WSGG proposed in this work has an excellent agreement with the SNB results in both test cases. The *Shan* WSGG, which showed good performance in the oxygen-hydrogen cases, overestimates the SNB heat flux for the BKB test case of approximately 90%. Two reasons can be identified. First, the model coefficients are tabulated for fixed values of the ratio of the molar concentrations of H_2O and CO_2, which do not coincide exactly with the conditions found in the combustion chamber. However, this is not enough to explain the large overestimation. The second and most important reason is the larger degree of radial non-uniformity of the temperature flowfield with respect to the other test cases. In fact, the relatively low pressure (10 bar) and wall temperature (400 K) produce a large thermal boundary layer. *Shan*'s model, which is in agreement with the spectral results only for combined high temperature and pressure, does not correctly take into account the reduction in heat flux induced by the cool layer close to the wall.

Experimental heat flux results are also available for the BKB test case, and are

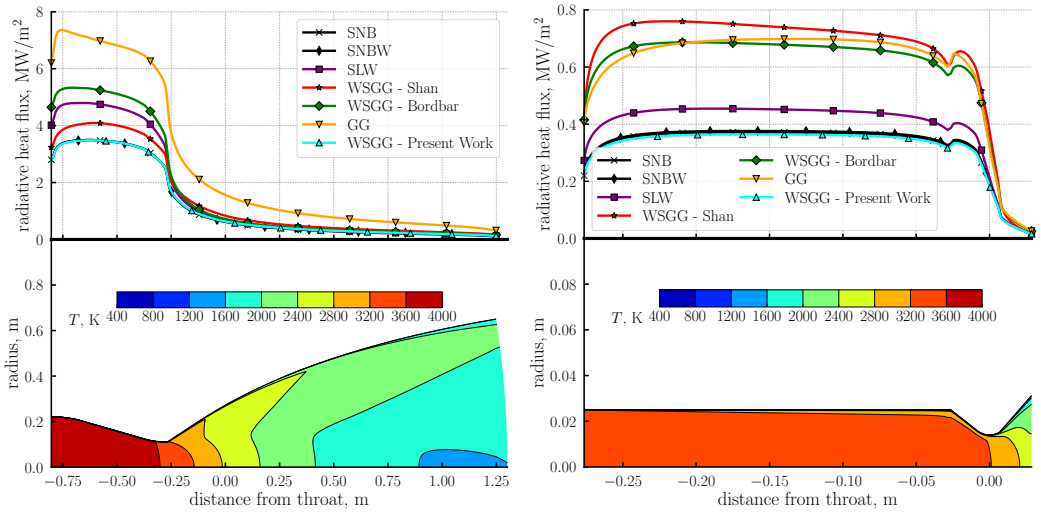

(a) HPE. (b) BKB.

Figure 5.10. Comparison of gas radiation models on oxygen–methane test cases.

compared with the total numerical heat flux in Fig. 5.11. The same caveats of the Sec. 5.1.3 apply: the relatively low radiative share of the total heat flux and the uncertainties in the modeling of the injection plate do not allow to perform a complete validation of the proposed models. Rather, the results can still be used to assess the effect of the gas radiation model on the overall heat flux. It can be seen how the total heat flux at the end of the cylindrical portion of the chamber with the SNB approach is in extremely good agreement with the experimental data, while the GG results are almost outside of the experimental error band.

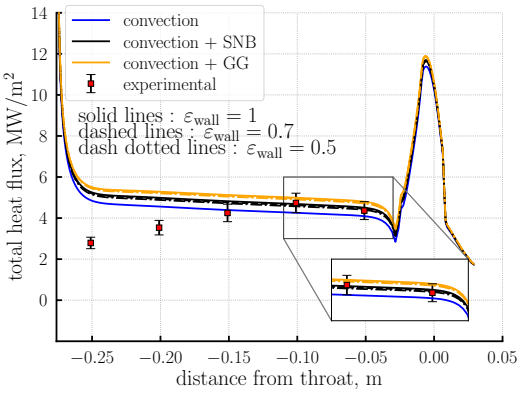

Figure 5.11. Comparison of numerical and experimental data for the BKB test case.

5.3 Reduced-order modeling

Aim of this section is to bridge the gap between radiative calculations and parametric LRE design, developing a reduced order model for the estimation of the radiative

heat flux. For all emissivity computations the WSGG model developed in Sec. 5.2.2 is employed.

5.3.1 Test cases

Two oxygen–methane test cases are considered in this section. The first one is a seven-element lab-scale thrust chamber described in [132] (referred to as TUM), while the second one is the HPE engine inspired by the Space X Raptor 1 [131] employed also in Sec. 5.2.3. Details of the two test cases are reported in Tab. 5.5 (the details of the HPE test case are repeated for the sake of completeness).

Table 5.5. Test case data.

Test case	throat radius, cm	length[a], cm	pressure, bar	OF	T_{wall}, K
HPE	22.16	10	250	3.6	900
TUM	4.75	34.4	18.3	2.65	300-418

[a]Only the cylindrical part of the chamber is considered.

For both engines a reference CFD computation has been performed [126, 131], employing an in-house RANS solver for turbulent, reactive flow [125], assuming for the sake of simplicity a uniform injection of combustion products through the whole injection plate area (CPI approach), as also done in Sections 5.1.3 and 5.2.3.

The temperature flowfields for both test cases are reported in Fig. 5.12, together with the radiative heat fluxes computed with the DTM algorithm and $\varepsilon_{\text{wall}}$=1. Significant differences can be noted between the two heat flux profiles. First of all the peak value is almost one order of magnitude higher in the large-scale engine than in the lab scale one (≈ 5 MW/m^2 vs ≈ 0.4 MW/m^2). This is due to the different OF, chamber pressure and size of the test cases. In fact, the large-scale engine not only has a higher chamber temperature, but is also significantly more optically thick, resulting in a higher radiative heat flux. However, the qualitative profile heat flux profile is similar for both cases, retaining three main features:

1. As soon as the combustion products expand in the nozzle a sudden drop in heat flux is present, due to the decreasing temperature.

2. In the cylindrical part of the chamber and in the first part of the convergent is heat flux is almost constant.

3. The heat flux increases sharply in the immediate vicinity of the injection plate.

The analysis of the features will lead the derivation of the reduced model in the next section.

5.3.2 Model derivation

The model takes as input the nozzle profile, the propellant combination and the injection temperatures, the chamber pressure, the OF, the wall emissivity, and the wall temperature. For each nozzle section a chemical equilibrium calculation employing the NASA CEA code [74] is performed, retrieving temperature, pressure,

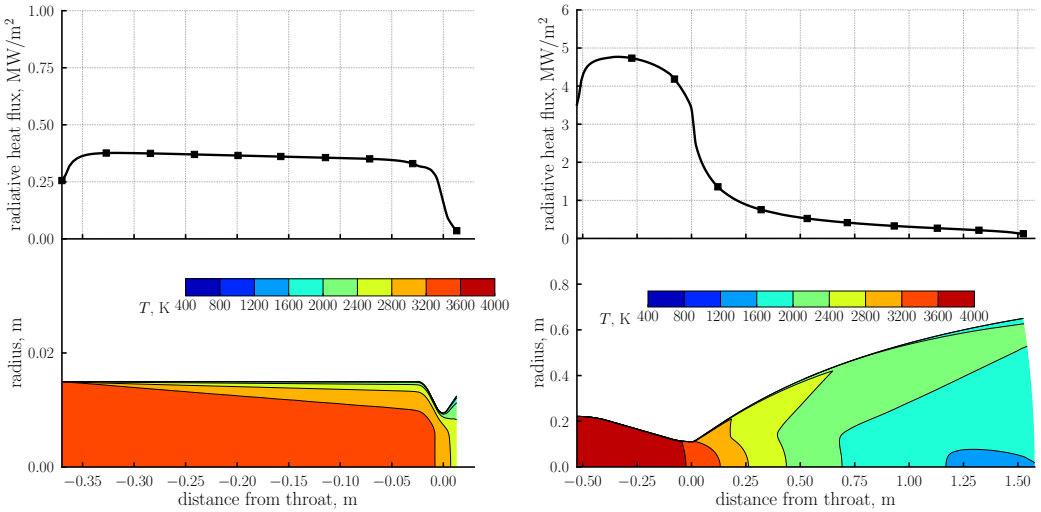

(a) TUM. (b) HPE.

Figure 5.12. Temperature flowfields and radiative heat flux ($\varepsilon_{\text{wall}} = 1$).

and composition. Employing the CEA results, radiative properties of the gases (ε, κ_{i_g}, a_{i_g}) are computed. To compute the emissivity the local nozzle diameter is used as length. To take into account the nozzle expansion process, a first heat flux is computed as

$$q_1(x) = \sigma\varepsilon(x)T^4(x) \tag{5.6}$$

This equation takes into account the fact that gaseous media are rarely close to black-body conditions, and thus employing only $\sigma T^4(x)$ to evaluate q would lead to a significant overestimation. As reported in Fig. 5.13, Eq. (5.6) is able to reproduce quite faithfully the heat flux decrease in the nozzle. However, the model fails to account for the edge effects near the injection plate. To do so, we employ the analytical expression for the heat flux in a homogeneous cylinder, which is derived in Appendix A3. Employing Eq. (A3.9), and using an absorption coefficient $\kappa = -\ln(1-\varepsilon)/(2R(x))$ we update the heat flux as

$$q_2(x) = \sigma T^4(x) f_{\text{cyl}}(x, \kappa, L, R(x)) \tag{5.7}$$

where f_{cyl} consists of the three integrals of Eq. (A3.9) and L is the thrust chamber length. Looking at Fig. 5.13 it can be seen how the analytical expression allows for a good agreement with the reference results.

Until know we have concerned ourselves solely with black walls ($\varepsilon_{\text{wall}} = 1$). This is, however, a strong simplifying assumption, since the emissivity of metals or thermal barrier coatings is seldom that high [133, 134]. For example, Ref. [31] reports values for the emissivity of oxidized copper between 0.4 and 0.9, depending on the temperature. Figure 5.14 shows how the net peak wall heat flux decreases almost linearly with wall emissivity. It can be seen that for the large scale engine the decrease is more pronounced than the one of the lab scale engine. This is due

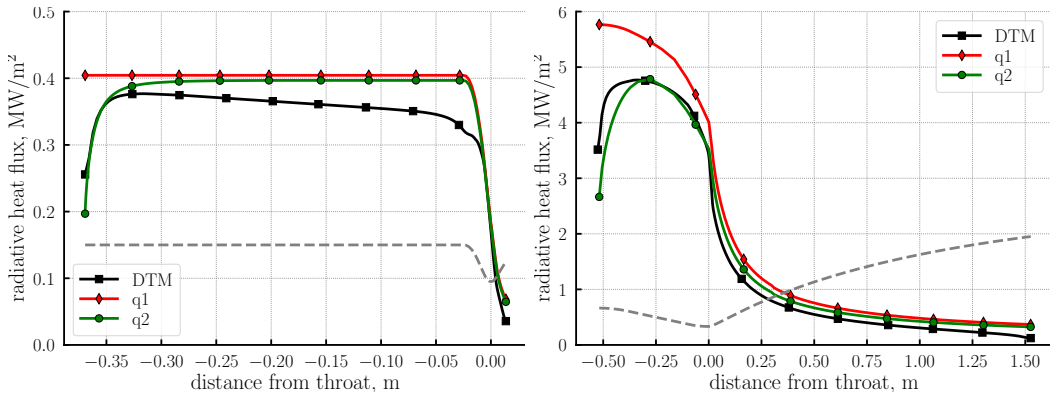

(a) TUM. (b) HPE.

Figure 5.13. Comparison of different 1D models and reference results ($\varepsilon_{\text{wall}} = 1$).

to the fact that at large scale (optically thick) the impinging heat flux is almost constant, and thus the net one is

$$q_{\text{net}} \approx \varepsilon_{\text{wall}} q_{\text{imp}}$$

However, if the medium is optically thin, such as in the lab scale engine, the impinging heat flux increases with diminishing wall emissivity, leading to a reduced decrease of q_{net}. Moreover, as reported in Fig. 5.14, the variation of the heat flux with wall emissivity is affected by the adopted spectral model.

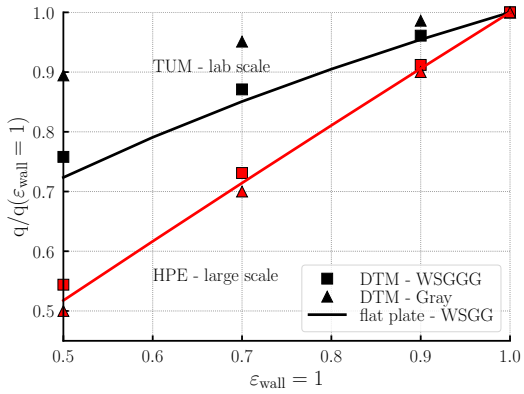

Figure 5.14. Effect of wall emissivity on peak wall heat flux.

To correctly take into account the effect of wall emissivity we employ a mono-dimensional formulation, imagining to substitute the cylinder with two parallel plates at distance $2R$. This allows us to employ the analytical expression for the heat flux between two parallel plates separated by an homogeneous medium [7]. Such expression, rearranged for the WSGG model, reads

$$q_{\text{plate}} = \sum_{i_g=0}^{N_g} q_{i_g} = \sigma(T^4 - T_{\text{wall}}^4) \sum_{i_g=0}^{N_g} \frac{-2a_{i_g}\left[E_3(\tau_{i_g}) - 1/2\right]}{1 + \left(\frac{1}{\varepsilon_{\text{wall}}} - 1\right)\left[1 - 2E_3(\tau_{i_g})\right]} \tag{5.8}$$

where $\tau_{i_g} = \kappa_{i_g} 2R(x)$, and $E_3(z)$ is the exponential integral of order 3

$$E_3(z) = \int_1^\infty e^{-zt} \frac{dt}{t^3} \tag{5.9}$$

Thanks to Eq. (5.8) we can compute a scaling factor to take into account the wall emissivity

$$f_{\varepsilon_{\text{wall}}} = \frac{q_{\text{plate}}(\varepsilon_{\text{wall}})}{q_{\text{plate}}(\varepsilon_{\text{wall}} = 1)} \tag{5.10}$$

represented by the solid lines of Fig. 5.14, which match quite well the DTM results. Finally, the net heat flux is evaluated as

(5.11)

where we have included also the term accounting for wall emission, which is however usually negligible, being $T^4_{\text{wall}} << T^4$. The comparison with the reference solutions in Fig. 5.15 shows how the proposed 1D model is able to match the heat flux results with sufficient precision.

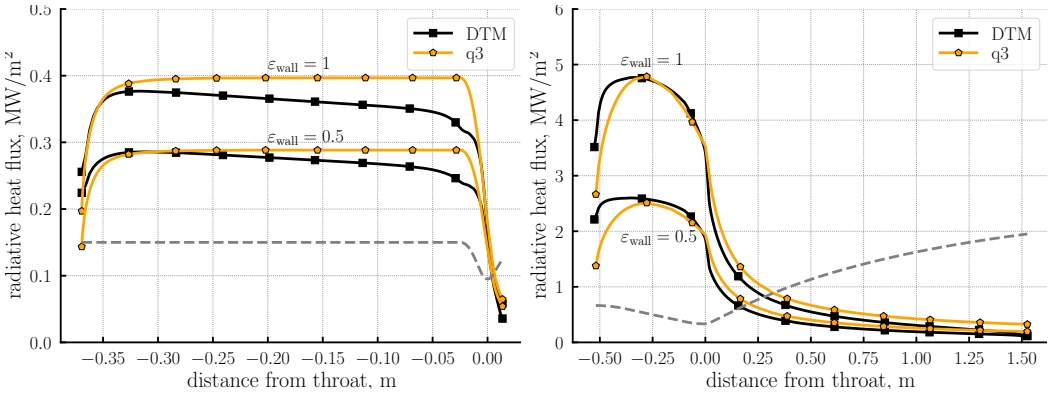

(a) TUM. (b) HPE.

Figure 5.15. Comparison of 1D and DTM results.

5.3.3 Injection effects

The results obtained in the previous section have been based on reference DTM solutions obtained assuming injection of fully burned combustion products on the entire injection plate. In real-life scenarios, depending on the specific injector arrangement, a flame development region will be present in the proximity of the injection plate, lowering the heat flux near the injectors.

For the lab-scale test case, a CFD solution taking into account the injection plate configuration is available [126], where the central injector is kept unchanged, whereas the six peripheral injectors are replaced with an equivalent annular injector to retain axial symmetry. Such approach, named axisymmetric propellant injection (API) has shown to compare well with experimental heat flux data [126, 127]. The temperature flowfield in Fig. 5.16 shows how a mixing equivalent to the CPI simulation is retained

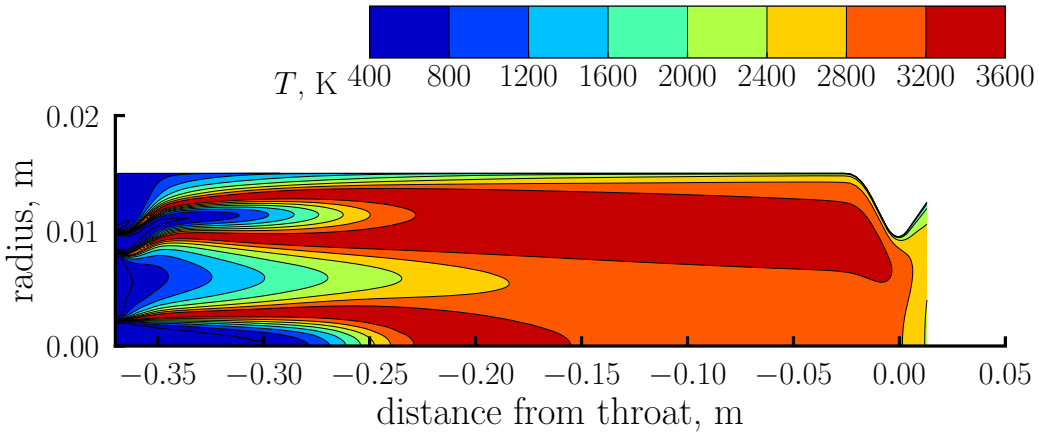

Figure 5.16. TUM flowfield with API simulation.

only quite far from the injection plate. This is consistent with the adopted coaxial injectors and with the relatively large injector spacing.

The radiative heat fluxes computed with the DTM algorithm from the API flowfield are shown in Fig. 5.17, showing how the heat flux value at the end of the chamber is comparable to the one of the CPI flowfield, while significant differences are present near the injection plate. Consistently with the temperature flowfield, the heat flux starts from a near-zero value and reaches a plateau only for $x > 0.2$ m. Considering that different injector types or spacings will result in different development lengths, it is not possible to derive an effective 1D model without employing some CFD or experimental data as reference. For example, one could compute the radiative heat flux with Eq. (5.11), employing for each abscissa the average temperature computed from the API flowfield instead of the one provided by CEA. As shown in Fig. 5.17, the results match satisfactorily the reference data, proving how the only information needed to estimate the radiative heat flux is a reasonable average temperature profile, which may be obtained from CFD analysis or previous expertise.

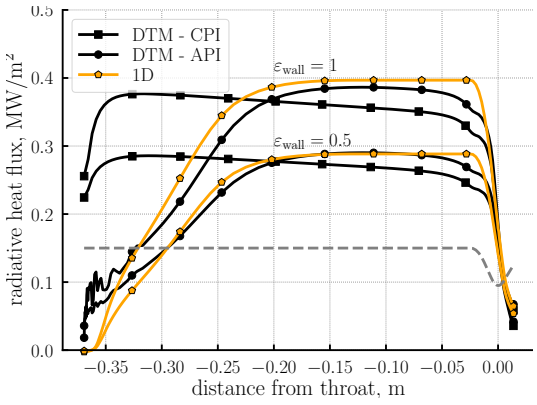

Figure 5.17. Radiative heat flux computed with CPI, API, and 1D approach.

5.3.4 Effect of propellant combination

In the previous sections we have analyzed only oxygen–methane test cases. However, the 1D model may be employed to any propellant combination, given its general formulation. Figure 5.18(a) compares the emissivities and heat fluxes computed employing chemical equilibrium calculations and the WSGG model for several propellant combinations. Almost all propellant combinations yield heat fluxes very close one to each other and close to 5 MW/m^2 near stoichiometric conditions, with the exception of the H_2O_2-RP1 combination. In fact, despite the very high emissivity, due to the high water vapour content (see Fig. 5.18(b)), the low adiabatic flame temperature does not allow to exceed the 3 MW/m^2 of heat flux. The fact that the other propellant combinations yield similar heat fluxes is due to the combined effect of different composition and flame temperature.

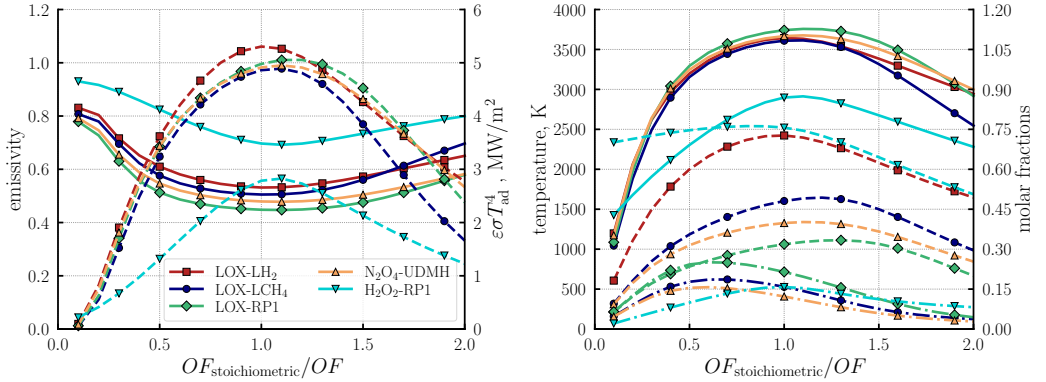

(a) Emissivity (solid lines) and heat flux (dashed lines).

(b) Adiabatic flame temperature (solid lines) and composition (dashed lines H_2O, dash-dotted lines CO_2).

Figure 5.18. Comparison of radiative properties of combustion products of several propellant combinations ($p_c = 100$ bar, $L = 1$ m).

5.4 Concluding remarks

The numerical analysis of radiative heat transfer in LREs has led to the following observations. The radiative flux is governed by the emission of H_2O and CO_2, with peak values located at the end of the cylindrical part of the combustion chamber. The comparison of gas property models indicates that gray-gas assumptions do not adequately represent the spectral characteristics of combustion products. The development of tailored WSGG models provides a computationally efficient alternative to more complex spectral models, while maintaining a level of accuracy suitable for engineering applications. Furthermore, the 1D modeling approach developed in this study provides a tool for the rapid estimation of heat loads, showing a degree of consistency with multi-dimensional solvers that justifies its use in the preliminary design phase.

Chapter 6

Hybrid rocket engines

This chapter investigates radiative heat transfer in hybrid rocket engines, taking into account the contributions from both gas and soot particles. Firing tests of a GOX-HPTB engine are numerically rebuilt, revealing how the radiative heat flux yielded by the gas phase may increase the regression rate up to 13%. In fuel rich conditions, soot radiation is identified as a key cotributor. A global soot model based on C_2H_2 as precursor is employed, obtaining a good prediction of regression rates at $OF \approx 1$.

Contents

This chapter aims to assess the role of thermal radiation in the internal ballistics of hybrid rocket engines, focusing on the regression rate increase induced by the combined gas and soot radiation. Unlike the previous chapter, where a reduced-order model was introduced for generic liquid rocket engine applications, the present analysis focuses on a single HRE, for which a detailed reconstruction of several firing tests is carried out.

The decision to concentrate on one specific configuration is motivated by two reasons. First, our goal is to develop a methodology that can be systematically applied to other hybrid systems: an in-depth analysis allows us to validate such approach. Second, the performance and behavior of HREs are strongly dependent on design features such as injector type (axial, swirl), prechamber and postchamber geometry, fuel grain layout (single-port, multi-port, helical, etc.), and the nature of the fuel itself (liquefying or pyrolyzing). Because of this strong configuration dependence, deriving general conclusions would require an extensive comparative analysis across many different designs, which is beyond the scope of this chapter.

Instead, the focus here is on demonstrating the methodology in a representative case study.

6.1 Numerical setup

The test case analyzed in this chapter is a 1 kN class HRE burning gaseous oxygen and HTPB [135], shown in Fig. 6.1. Nine firing tests are analyzed, reported in Table 6.1. They have been selected because of the relatively large span of G_{ox} and OF, allowing to assess the effect of radiation for varying operating conditions. Moreover, HTPB is known to produce soot in fuel rich conditions, and is thus a good candidate for radiative heat transfer studies. The tests are divided in three triplets depending on the G_{ox} range: low G_{ox} (tests 1-3), medium G_{ox} (tests 4-6), and high G_{ox} (test 7-9). For each triplet a test with small, medium, and large port diameter respectively is performed.

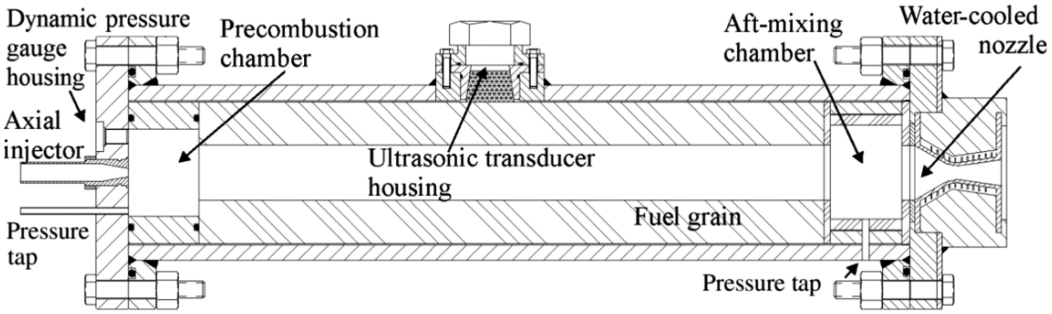

Figure 6.1. Schematic of the laboratory-scale hybrid engine. Image taken from [83].

Table 6.1. Firing test average results.

Test	t_b, s	G_{ox}, kg/(m$^2\cdot$ s)	$\bar{D}_{\text{average}}$, mm	$\bar{\dot{r}}$, mm/s	$\bar{p}_c$, atm	OF
1	12.9	39.7 ± 2.3	28.7	0.56 ± 0.031	3.9	0.95 ± 0.05
2	29.3	55.0 ± 1.9	40.8	0.66 ± 0.020	10.2	1.58 ± 0.03
3	41.9	59.8 ± 1.5	53.9	0.77 ± 0.024	18.6	1.90 ± 0.02
4	8.4	128.9 ± 6.9	29.3	0.92 ± 0.068	11.3	1.89 ± 0.12
5	12.4	145.4 ± 5.8	35.5	1.13 ± 0.059	17.7	2.09 ± 0.09
6	17.3	180.3 ± 5.6	43.3	1.26 ± 0.049	31.0	2.81 ± 0.08
7	4.1	210.6 ± 13.4	26.4	1.19 ± 0.166	14.4	2.13 ± 0.27
8	8.1	219.1 ± 9.9	32.8	1.39 ± 0.103	22.6	2.35 ± 0.15
9	11.9	225.4 ± 7.6	40.4	1.60 ± 0.082	33.1	2.59 ± 0.11

The computational setup employed for all simulations is reported in Fig. 6.2. It is composed by a pre-chamber ($0 < x < x_1$), a fuel grain ($x_1 < x < x_2$), an aft mixing chamber ($x_2 < x < x_3$) and a nozzle ($x_3 < x < L$). The prechamber, fuel grain, and postchamber are respectively 65 mm, 570 mm and 75 mm long. The throat radius is 8 mm (being the nozzle water cooled no erosion was present) and the nozzle expansion ratio is 2.6. The pre-chamber and post-chamber radii are taken

equal to the one of the fuel grain. Such simplifying assumption allows to reduce the computational cost of the simulation, and it has been shown by [50, 83] that the effect of the cavities on the computed regression rate and chamber pressure is small. The injector is simulated as an inlet with imposed mass flow rate (taken as equal to the average experimental value) and temperature (300 K), all solid walls except for the fuel grain are considered isothermal at 1000 K, and at the nozzle exit, being the flow supersonic, an extrapolation boundary condition is employed. On the axis and lateral faces of the computational setup symmetry conditions are enforced. A structured computational grid is employed (Fig. 6.3), composed of 10080 volumes, with clustering near the injector, at the walls and at the nozzle throat to ensure a correct resolution of the mixing layer, boundary layer and subsonic-supersonic transition respectively.

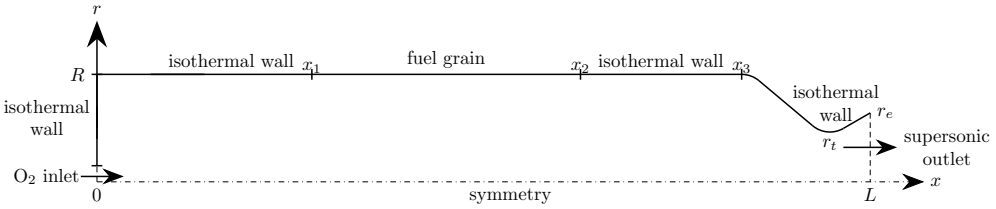

Figure 6.2. Computational setup.

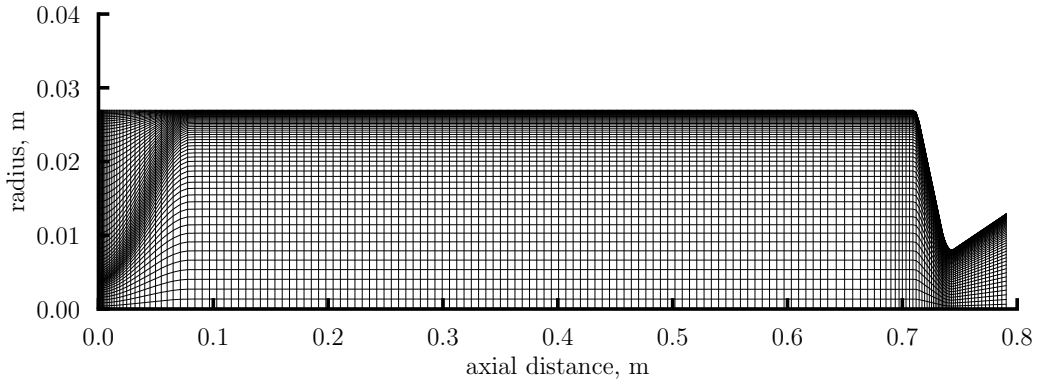

Figure 6.3. Computational grid for test 6.

The adopted turbulence model is k-ω SST and a skeletal chemical mechanism for C_4H_6 combustion comprising 20 species and 54 reactions is adopted [136]. The mechanism has been chosen since it was obtained specifically for HRE conditions from computational singular perturbation (CSP) based simplification of a detailed mechanism comprising 561 species and 2538 reactions [137]. Moreover, C_2H_2, needed for soot computations, was one of the target species employed in the mechanism simplification.

6.1.1 Grid convergence analysis

A grid convergence analysis has been carried out on test 9, since it is the one with highest G_{ox}. A coarse and fine grid have been considered, obtained halving and doubling, respectively, the number of axial and radial volumes with respect to the medium grid shown in the previous section. The results show that the computed regression rate and chamber pressures are in close agreement between the medium and fine grids (see Table 6.2). Moreover, the values of the non-dimensional wall distance y^+, shown in Fig. 6.4, ensure a good resolution of the boundary layer above the fuel grain. On the basis of these results the medium grid was employed for all simulations.

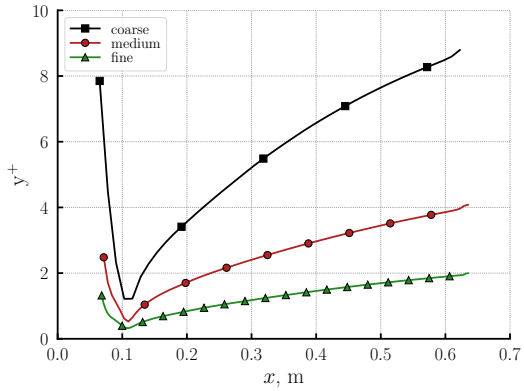

Figure 6.4. Non-dimensional wall distance on fuel grain.

Table 6.2. Meshes considered for the grid refinement study.

	Coarse	Medium	Fine
Mesh	84×30	168×60	336×120
Number of control volumes	2520	10080	40320
Maximum cell height on grain (μm)	21.4	10.7	5.35
Maximum y^+ on grain	8.93	4.05	1.98
$\dot{r}/\dot{r}_{\text{fine}}$	1.057	0.9998	-
$p_c/p_{c,\text{fine}}$	0.979	0.991	-

A grid convergence analysis has been performed also on the number of rays of the radiative heat transfer solver, taking into account three values for the number of rays $N_r = 144, 256$ and 400. The average computed radiative heat flux on the fuel grain decreases by 1.57% moving from 144 rays to 256, and only by 0.18% increasing the number of rays to 400 from 256. For this reason, $N_r = 256$ was employed in all calculations.

6.2 Results

For each firing test a single simulation at the average diameter has been performed. In fact, it has been shown in [50] how such approach leads to a reasonable agreement

with the experimental data, without the need for resource-intensive shape change computations. The temperature flowfields are shown in Fig. 6.5. A good degree of mixing is achieved in all test cases, with the exception of test 1, whose extremely fuel rich conditions result in a significant stratification of the flow. The flame is always anchored at the injector, except that for test 7, where the recirculation zone is not wide enough to ensure an anchoring point.

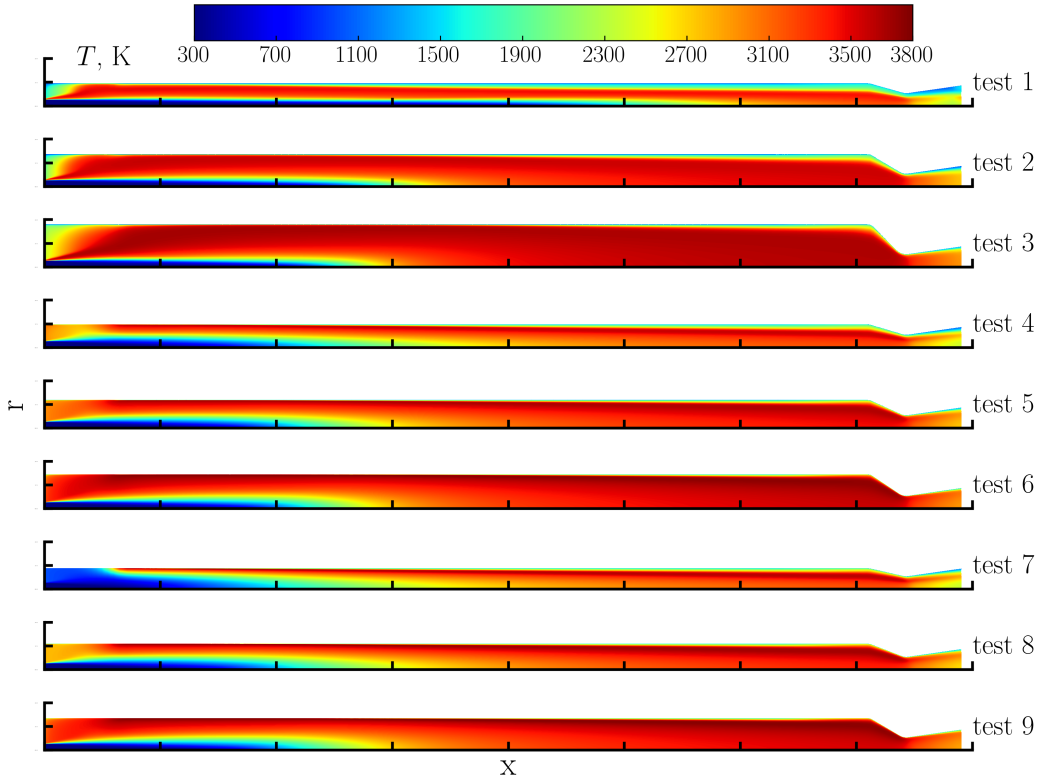

Figure 6.5. Temperature flowfields.

The average computed fuel regression rates are compared with the experimental data in Fig. 6.6. The numerical results are able to capture the main trends shown by the test data, such as the increase of regression rate with both G_{ox} and average port diameter. In particular, the latter comes from the the fact that a larger port diameter increases the size of the recirculation zone, where the convective heat flux is maximum. The average regression rate is always underestimated, with an error less than 20% for all tests except test 1 (-37%), where the very fuel rich conditions may result in significant soot radiation, which will be discussed in Sec. 6.2.2. The agreement between numerical and experimental chamber pressure is extremely good, despite the underestimation of the regression rate. This can be explained taking into consideration that $p_c = \dot{m}/(c^* A_t)$, and the computed regression influences both $\dot{m}$ and c^*, being the latter a function of the OF.

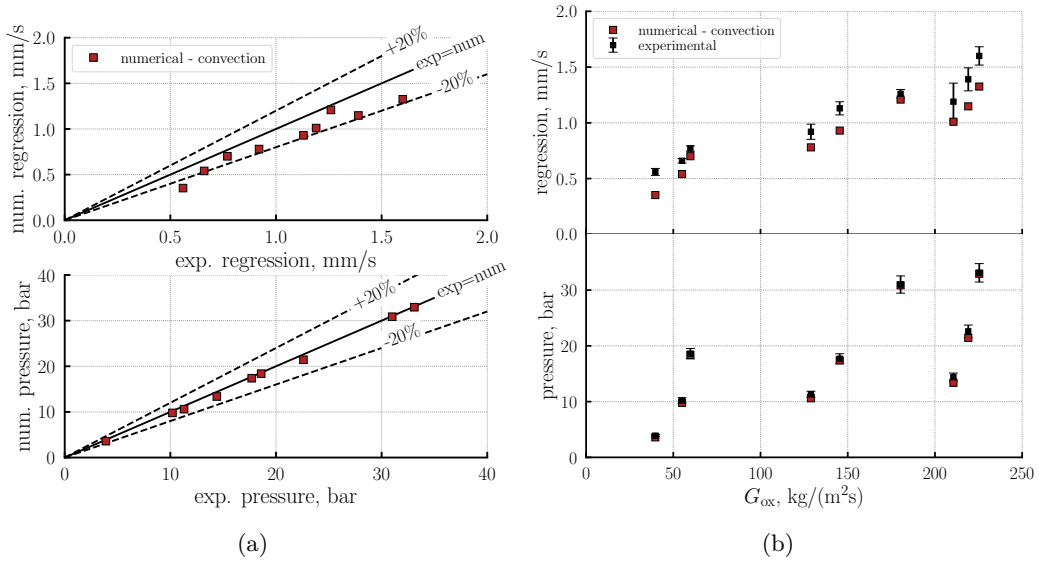

(a) (b)

Figure 6.6. Firing test rebuilding, no radiation. For chamber pressure a 5% error bar is considered.

6.2.1 Gas radiation

For each test case a simulation taking into account gas radiation has been performed. The SNBW spectral model was adopted, since it allows to easily include the soot contribution to the absorption coefficient, which is instead not possible with the WSGG models derived in Chapt. 5. Contributions from H_2O, CO_2 and CO were included. For the sake of simplicity, all walls have been considered as black. This is due to the fact that no complete dataset is available in the literature on the radiative properties of the solid fuel (HTPB). However, from the data of [138, 139], which report the reflectances of several polymers, and the measured index of refraction of HTPB at room temperature [140], it can be safely assumed that $\varepsilon_{\mathrm{HTPB}} > 0.9$. Considering the results of Sec. 5.3.2, where it has been shown how the effect of wall emissivity on the impinging radiation in small-scale engines is quite limited, the assumption of black walls should not have any relevant impact on the computations.

The effect of gas radiation is shown in Fig. 6.7 for all test cases. The average regression rate increase is around 6%, while the chamber pressure is not significantly affected. As stated in the previous section, pressure is less sensitive to changes in the wall heat flux than regression, since it depends on mass flow rate, OF, and mixing.

Figure 6.8 reports the percentage increase in regression rate due to gas radiation, which ranges from slightly above 3% (test 7) to almost 13% (test 3). The relative effect of radiation decreases with increasing G_{ox} and increases with the port diameter D. This is not only due to the fact that the average path length is proportional to D, but also that the tests with higher D have also higher pressure, and thus an higher optical thickness. For the same reasons the effect of gas radiation on test 1 does not exceed 5%, despite the low G_{ox}: the low D and p result in very optically thin conditions. Moreover, the fuel rich conditions of test 1 result in a wide cold layer above the fuel grain (see Fig. 6.5), resulting in a low radiative heat flux to the

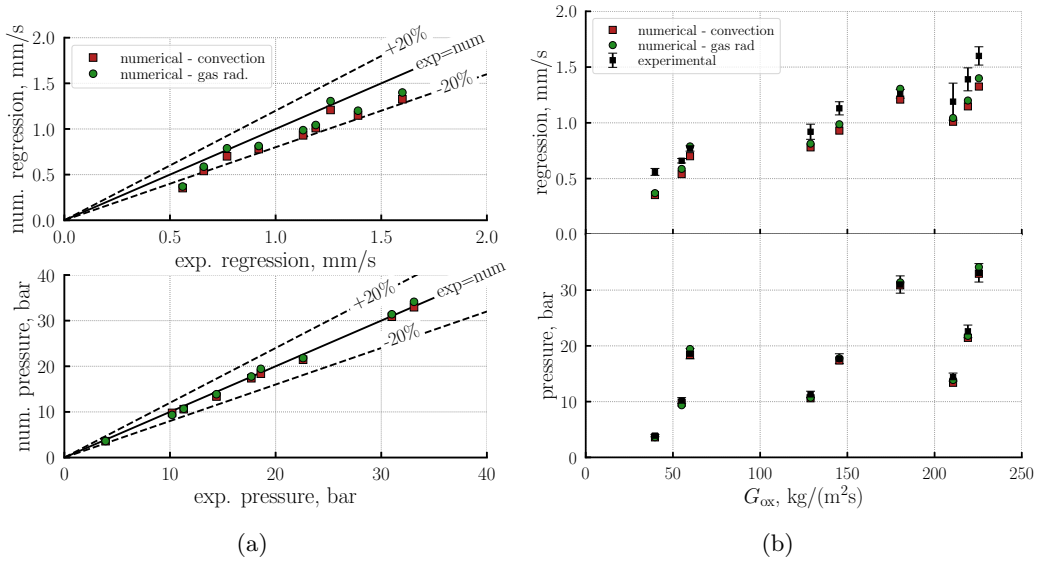

Figure 6.7. Firing test rebuilding, with gas radiation. For chamber pressure a 5% error bar is considered.

fuel grain.

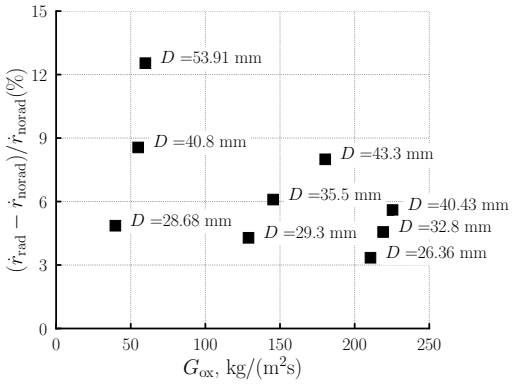

Figure 6.8. Percentage increase of average regression rate due to gas radiation.

The local radiative heat fluxes on the fuel grain are reported in Fig. 6.9 for all tests. The impinging radiation is reasonably uniform for all cases, but the profiles differ significantly from test to test, depending on the specific flowfield. The tests with highest q_{rad} are 3, 6, and 9, which are the ones with highest optical thickness. On the other hand, tests 1, 4, and 7 (low D and p), have the smallest radiative heat flux.

6.2.1.1 Effect of participating species

When performing radiative heat transfer calculation in combustion environments, one usually considers as participating species H_2O, CO_2 and CO. As also discussed in Sec. 5.2.1, H_2O and CO_2 are usually the most relevant, and it was also proved

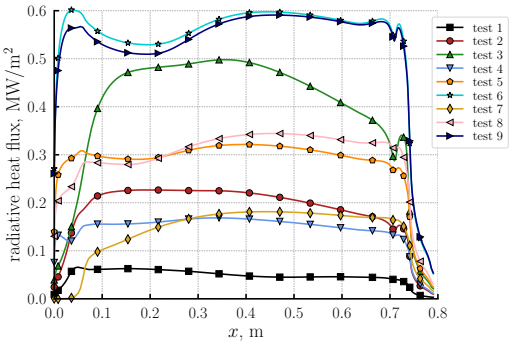

Figure 6.9. Local radiative heat flux.

how, in LRE conditions, water vapor is by far the most important molecule from the radiative transfer standpoint. A similar analysis has been performed for the HRE studied in this chapter, and the results are reported in Fig. 6.10. The effect of CO is minimal, while the main contribution comes, depending on the port diameter, either from H_2O or CO_2. In fact, for tests 1, 4, and 7 (small port diameter) the heat flux given by the sole CO_2 is higher than the one yielded by H_2O alone, and vice-versa for tests 3, 6, and 9 (large port diameter).

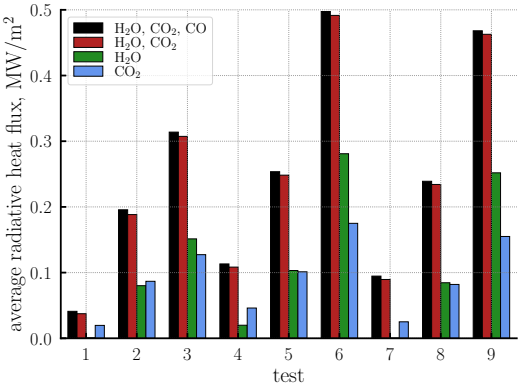

Figure 6.10. Effect of participating species on radiative heat flux.

Such effect can be explained looking at Fig. 6.11, which shows the temperature and molar fraction profiles at middle grain for tests 7 and 9. While the shape of the profiles is qualitatively similar, it can be seen that for test 7 (solid lines) the water vapor concentration is shifted towards the centerline (as is the temperature), implying that the largest radiative contribution comes from the hot carbon dioxide near the fuel grain.

6.2.1.2 Effect of radiative source term

In the previous simulations, the coupling between CFD and radiative calculations has been performed only at the boundaries, including the radiative heat flux in the gas-surface interaction, but neglecting its contribution in the energy conservation equation of the flow. Such coupling has been shown to be extremely important in

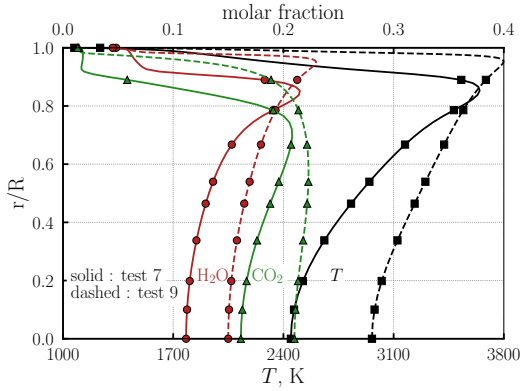

Figure 6.11. Temperature and molar fraction profiles at middle grain.

lab-scale turbulent flames, such as the Sandia D flame [141], but to be negligible in LRE conditions [31]. The goal of this section is to quantify the effect of the divergence of the radiative heat flux on the CFD-DTM coupling. For the sake of simplicity this analysis has been performed only for test 6.

The divergence of the radiative heat flux is reported in Fig. 6.12. Where the temperature is low, near the injector and the fuel grain, $\nabla \cdot q_{\text{rad}}$ is negative, since the flow is heated by radiation. In the rest of the flowfield emission predominates over absorption and $\nabla \cdot q_{\text{rad}}$ is positive.

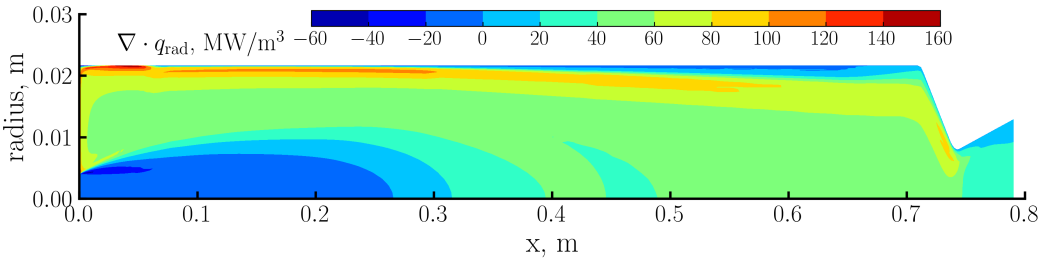

Figure 6.12. Radiative source term.

The effect of the coupling is reported in Fig. 6.13: the average regression rate is practically unaffected, with a slight decrease coming from the reduced convection (Fig. 6.13(a)). This is likely due to the fact that the boundary layer heats up and becomes slightly thicker. The flow temperature is changed by only a few tens of degrees (Fig. 6.13(b)). As expected, temperature increases where the flow is cold (absorption predominates) and decreases where the flow is hot (emission predominates).

The small effect of the source term can be confirmed performing a simplified analysis, rewriting the energy conservation equation as if the flow were 1D:

$$\rho u A dh = \nabla \cdot q_{\text{rad}} V \tag{6.1}$$

where ρ, u, A, and h are the density, velocity, cross-section, and enthalpy. Assuming that the flow is thermally and calorically perfect, and that the source term is constant,

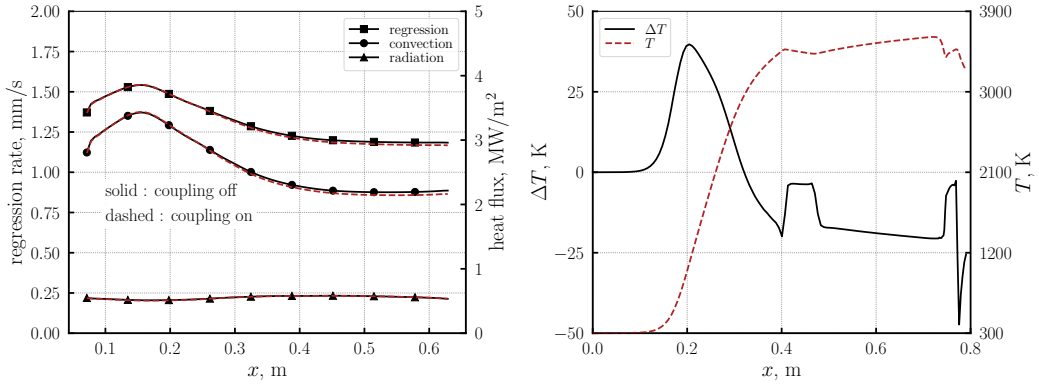

(a) Regression rate.

(b) Temperature on the centerline.

Figure 6.13. Effect of radiative source term.

the temperature change can be written as

$$\Delta T = \frac{\nabla \cdot q_{\text{rad}} L}{\rho u c_p}$$

where we have rewritten the volume as $V = A \cdot L$. For test 6 the properties of O_2-HTPB combustion products computed from CEA at $OF = 2.65$ and $p_c = 32.33$ bar (the ones resulting from the simulation) are $c_p = 8.22$ kJ/kg/K and $\rho = 2.46$ kg/m^3. The average flow velocity is $u \approx 90$ m/s. Using as length 0.5 m results in a ΔT of 24.7 K, which is comparable to the results of Fig. 6.13, and confirms that the energy equation coupling is not needed in HRE simulations.

6.2.1.3 Spectral and directional dependence of radiation

The average radiative heat flux shown in the previous sections is the result of the integration of the impinging radiation, whose angular and spectral dependence are discussed in this section. Figure 6.14 reports the impinging intensity, already integrated over the spectrum, at the middle of the fuel grain. Focusing on Fig. 6.14(a), it can be seen that: 1) the radiation is symmetrical around $\phi = 180°$, since the flowfield is axisymmetric; 2) the higher θ, the lower the variation of the impinging radiation, since for $\theta = 90°$ all rays collapse on the wall normal; 3) the peak radiation is for $\phi = 0°$ (looking towards the nozzle), with a lower peak for $\phi = 180°$ (looking towards the injector plate). This is due to the fact that the average temperature of postchamber and nozzle is larger that the one of the prechamber, since the oxidizer is injected at 300 K. Figure 6.14(b) shows instead how the radiation decreases as ϕ approaches 90°, since the average path length is smaller.

The spectral dependence of radiation is shown in Fig. 6.15 for three different directions. While the qualitative shape is the same between the three curves, quantitative differences are present, since each direction has its own temperature and species profile, which affect the final spectrum. This type of spectral-directional analysis not only clarifies how the total heat flux is obtained, but can also be highly valuable for flow diagnostics, where accurate modeling of the impinging radiation is required [142].

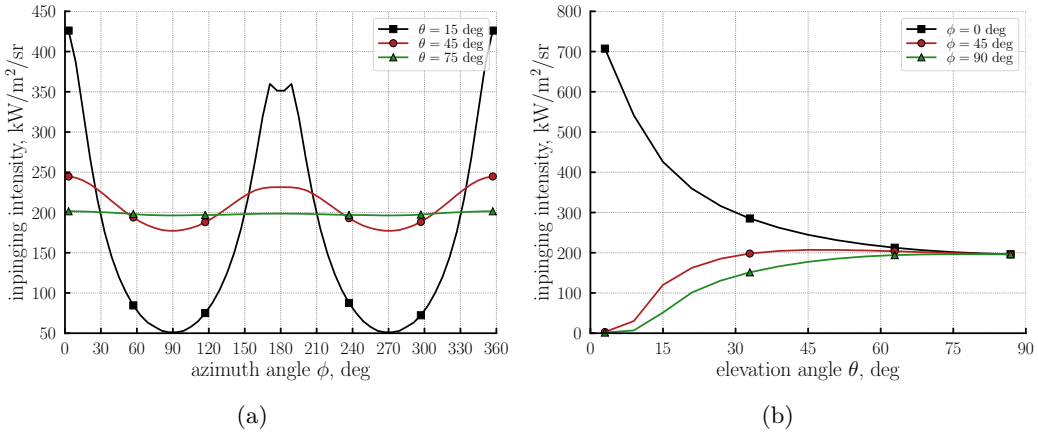

Figure 6.14. Angular dependence of impinging radiation.

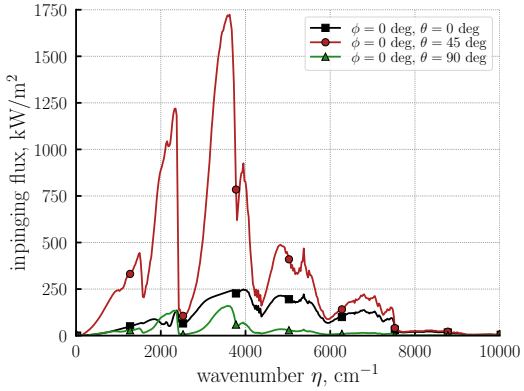

Figure 6.15. Spectral dependence of impinging radiation.

6.2.2 Soot radiation

In this section an analysis on the effect of soot radiation on the computed regression rate is performed, with the goal of assessing wether a simplified soot modeling approach, as the one described in Sec. 2.9, is able to improve the agreement with the experimental data in fuel rich conditions.

6.2.2.1 Soot model selection

The first step in such an analysis is to assess the effect of the soot generation/oxidation model. As discussed in Sec. 2.9, a global soot model based on the mixture fraction [52] and the Leung and Lindsted soot model based on C_2H_2 [93] are tested. For the sake of simplicity, only tests 1 and 6 are taken into consideration for the model selection. In fact, the first is extremely fuel rich ($OF = 0.95$) and its regression rate cannot be matched by the contributions of convection and gas radiation alone. On the other hand test 6 is the least fuel rich ($OF = 2.81$) and its regression rate compare well with the numerical results presented in previous sections. Our goal is to find a soot model which is able to increase the regression rate of test 1 while

not affecting significantly the results of test 6, where soot is not expected to play a major role.

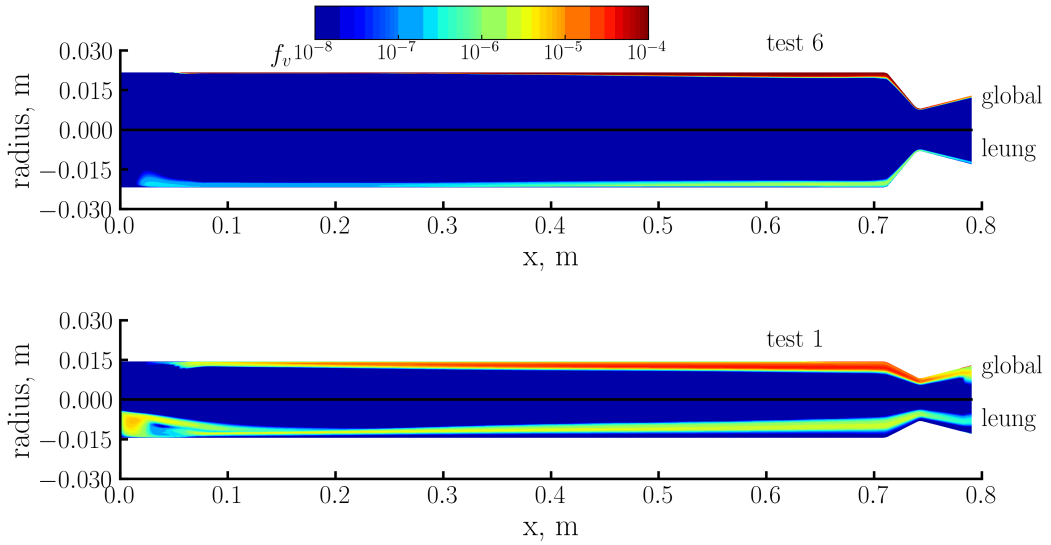

Figure 6.16. Soot flowfield for tests 1 and 6.

The soot volume fraction distributions are reported in Fig. 6.16. The global soot model predicts a higher soot volume fraction than the *Leung* model in both cases. Given that the forward reaction rate coefficient of the global model is the one for paraffin wax, and that the rates of the chemical model have been calibrated on laminar C_2H_4 flames, this difference can be expected and may result from the different conditions on which the models were calibrated. However, the global model yields a higher soot concentration for test 6 than test 1, which is unexpected, given that test 1 is the most fuel rich. This can be explained looking at Eq. (2.53), where it can be seen that the soot formation rate is proportional to ρ^2, which is significantly higher in test 6 given that the chamber pressure is 31 bar, whereas test 1 does not exceed 4 bar. The *Leung* model, instead, does not exhibit any explicit dependence on pressure, and yields an higher f_v for test 1 than test 6.

The radiative heat fluxes computed from the soot fields are shown in Fig. 6.17. For test 1, a 61% increase is obtained with the global soot model and a 85% increase with the *Leung* model with respect to the sole gas contribution. For test 6, however, the first model leads to a 84% increase in radiative heat flux, while the second model leaves it almost unchanged (+6%). Given that it is reasonable to assume that the soot contribution for test 6 ($OF = 2.81$) is limited, it can be deduced that the global soot model cannot be safely applied to test cases with a wide pressure range. For this reason it has been chosen to adopt the *Leung* model.

The results of the coupled simulations are reported in Tab. 6.3. The soot contribution increases the average regression rate by 4% on test 1, and of only 0.2% on test 6. It must be recalled that the increase of regression rate due to radiation is mitigated by the decrease of convection to the increase blowing from the surface, as reported for test 1 in Fig. 6.18.

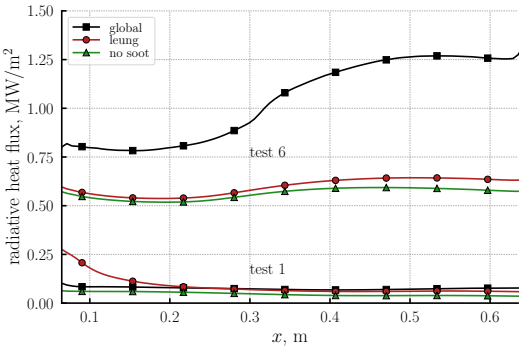

Figure 6.17. Radiative heat fluxes for tests 1 and 6.

Table 6.3. Effect of soot radiation on computed regression rate.

	exp	no rad	conv + rad gas	conv + rad gas + rad soot
			test 1	
$\dot{r}$ (mm/s)	0.56	0.352	0.363	0.385
error	-	-38.1%	-35.2%	-31%
			test 6	
$\dot{r}$ (mm/s)	1.26	1.187	1.287	1.289
error	-	-5.8%	+2.1%	+2.3%

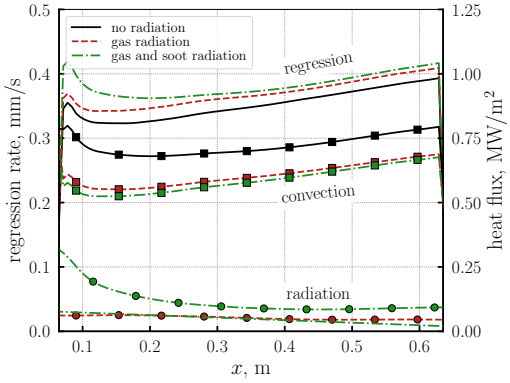

Figure 6.18. Effect of gas and soot radiation on test 1.

6.2.2.2 Firing test rebuilding

It is clear from the results reported in the previous section that the proposed soot model appears to not be able to predict the experimental regression rate in test 1. However, it has to be considered that the *Leung* model was calibrated on laboratory C_2H_4 flames, and thus may under-predict the sooting tendency of HTPB. For this reason, a parametric analysis was performed carrying out full CFD-DTM simulations on test 1, modifying the coefficients of the soot formation Arrhenius (Eq. (2.58) and (2.59)). Results showed that multiplying both coefficients by 30 a very good agreement between experimental and numerical regression rate could be achieved in test 1. To assess the performance of this updated model at different OF, all test

cases were simulated including the soot contribution, and the results are reported in Fig. 6.19. A good agreement is obtained for tests 1 and 4-9, while the regression rate of tests 2 and 3 is overestimated by more than 20%. This may be due to the fact that the model over-predicts soot concentration in mildly fuel rich conditions, such as the ones of tests 2 and 3 ($OF = 1.58$ and 1.9 respectively). It must be noted, however, that no optimization has been performed on the model coefficients. For example, multiplying both forward coefficients by a lower value would lead to an underestimation of the regression rate for test 1, but to an overall better agreement with the data. Nevertheless, considering the experimental and modeling uncertainties as well as the strong simplifying assumptions adopted, the proposed approach is regarded as a step forward in soot modeling for HRE applications.

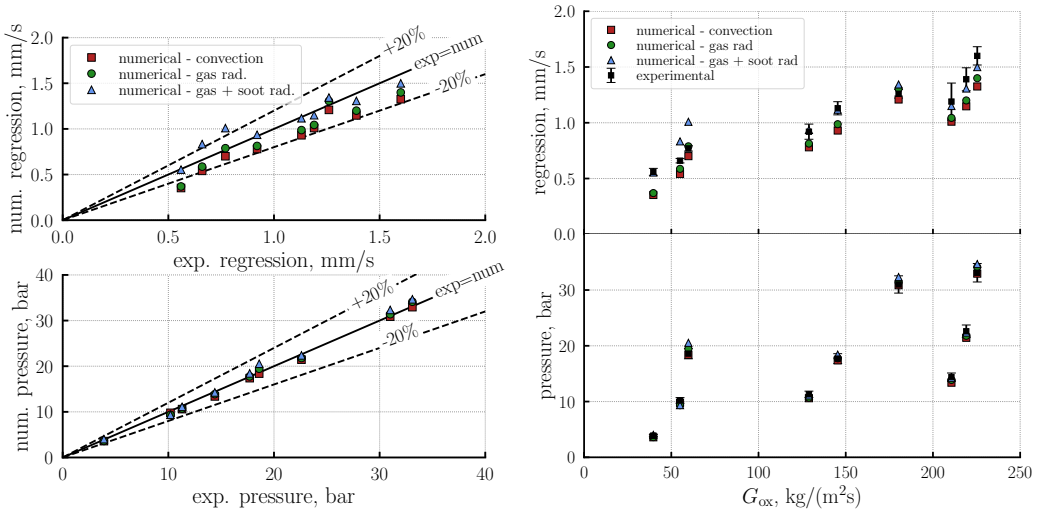

Figure 6.19. Firing test rebuilding, with gas and soot radiation. For chamber pressure a 5% error bar is considered.

6.2.2.3 Comparison with literature correlations

A final discussion on soot radiation can be performed comparing the heat flux results of the previous section with available radiative heat flux correlations for HREs. From a literature analysis two correlations have been identified, based on the data of Strand et al. [37] (GOX-HTPB slab burner with $OF \in [1.5 - 3.5]$). The first one is reported by [46]

$$q = \sigma T_g^4 \left(1 - e^{-\kappa_s}\right), \quad k_s = 0.51 - 0.113OF \tag{6.2}$$

where T_g is the gas temperature. The second correlation is directly reported in [37]

$$q = \sigma T_g^4 \left(1 - e^{-a_P N_p}\right), \quad N_p = \frac{\alpha_p p_c}{1 + OF - \alpha_p} \tag{6.3}$$

where a_P is a constant, N_p is the particle number density, α_p is the particle mass fraction, and p_c is the chamber pressure. In this analysis, we have employed for

α_p the peak soot mass fraction at $x = 0.35$ m (middle grain) and used $a_p = 0.05$. Figure 6.20 compares the average radiative heat fluxes computed by the CFD-DTM procedure and the above equations for all tests. The correlations appear to capture correctly the increase of radiation with OF in very fuel rich conditions (test 1-3), mainly due to the fact that T_g increases. However, both models significantly over-predict the heat flux for tests 4-9, despite the fact that such tests are inside the correlations OF range. Such behavior can be explained by the fact that the radiative heat flux is deeply influenced by the specific flow configuration, which depends on the injector and on the prechamber and fuel grain geometry. Therefore, simplified models based on a specific slab burner configuration may not perform well when applied to another test case.

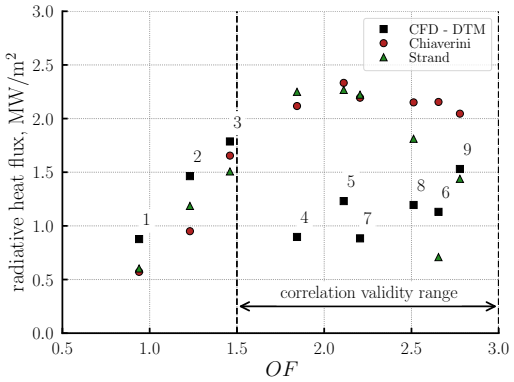

Figure 6.20. Comparison between CFD-DTM results and strand correlation.

6.3 Concluding remarks

The investigation of radiative heat transfer in hybrid rocket engines has led to the following conclusions. The analysis conducted across a wide range of operating conditions reveals that the gaseous radiative contribution accounts for up to 10% of the total heat flux. Regarding the gas-phase composition, it was found that H_2O and CO_2 are the principal species responsible for radiative emission, while the contribution of CO can be neglected without significant loss of accuracy. The role of the dispersed phase is highly dependent on the mixture ratio; for the propellant combination investigated, the soot contribution becomes relevant as the O/F ratio approaches unity. Furthermore, the results demonstrate that the soot generation model significantly influences the predicted soot distribution, concentration, and the resulting radiative flux. Although the current modeling approach shows consistency with available experimental data, the sensitivity of the results suggests that further studies are necessary to generalize these findings to a broader range of hybrid propulsion systems.

Chapter 7

Solid rocket motors

This chapter focuses on the numerical characterization of radiative heat transfer in solid rocket motors, with particular emphasis on the role of the dispersed phase. The analysis investigates the radiative properties of alumina particles, accounting for their size distribution and complex absorption and scattering patterns. Mie theory models are employed to quantify the impact of two-phase flow on the wall heat flux, comparing the radiative contribution with the convective loads.

Contents

Modern solid rocket propellants are typically composed an organic binder, aluminum powder, and an oxidizer, most commonly ammonium perchlorate (NH_4ClO_4) [1]. Such propellant formulation has profound influence on the radiative heat transfer characteristics of the combustion products. First of all, the reaction of aluminum with oxygen produces alumina (AL_2O_3), which is usually liquid at the combustion chamber temperatures and may solidify in the nozzle. Such particles are strong radiative emitters and, as will be shown in the next sections, dominate the radiation transport phenomenon. Secondly, among the gaseous combustion products of SRMs the species participating to radiative exchange are not only H_2O, CO_2 and CO, but also hydrocloric acid (HCl). For this reasons, modeling radiation heat transfer in SRMs requires specifically developed tools, and poses significant challenges. The purpose of this chapter is to provide a detailed analysis of the modeling aspects, with particular emphasis on the impact of possible simplifying assumptions on the computed heat flux (such as gray medium, isotropic scattering, etc).

Considering the need to model gas and particle radiation at the same time, the SNBW approach is adopted in this analysis, as also done in [60] and in Chapt. 6

for gas and soot radiation. For all computations the refractive index of alumina particles is computed adopting the Plastinin and Farmer correlations (see Sec. 3.4).

The structure of this chapter is briefly outlined below. In Sec. 7.1 SNBW data for HCl is obtained from line-by-line computations, and the effect of hydrocloric acid on the gas emissivity of SRM combustion products is discussed. Since the combination of spectral dependence and strong anisotropic scattering poses significant computational challenges, a simplified 1D test case is considered in Sec. 7.2, comparing heat flux results obtained with different modeling assumptions. Finally, heat flux results are obtained for a representative test case, the subscale HIPPO motor, in Sec. 7.3.

7.1 Statistical narrow band modeling of HCl

Hydrochloric acid is known to be an active radiating molecule [143] and its radiative properties have been the subject of previous studies, mainly due to its presence in SRM systems, but not with the same level of detail of other molecules such as H_2O or CO_2. The molecule is part of the HITRAN line–by–line database [144] (its data is reported as valid at high temperatures despite not being included in the hig-temperature specific database HITEMP), some narrow-band data is reported in the NASA SP 3080 (handbook of infrared radiation from combustion gases) [143], and the Planck-Mean absorption coefficient is also reported in [145]. Since the selected modeling approach for spectral radiation is the weak statistical narrow band (SNBW), there is the need to compute the band-averaged absorption coefficient (see Eq. (3.15))

$$\overline{\kappa}(T) = \frac{1}{xp} \int_{\Delta\eta} \kappa_\eta d\eta \tag{7.1}$$

where x is the molar fraction and p the pressure. The same spectral discretization adopted in [101] has been adopted, with 450 bands with a width of 25 cm^{-1} covering the range $\eta \in [0, 11250]$ cm^{-1}. The LBL calculations have been performed with a half-width truncation of 1500 cm^{-1} and a line cut off threshold of $1{\times}10^{-28}$ $\text{cm}^{-1}/(\text{molecule} \cdot \text{cm}^{-2})$ with a Voigt line profile. The band averaged coefficients are compared with their LBL counterparts in Fig. 7.1 for two values of temperature.

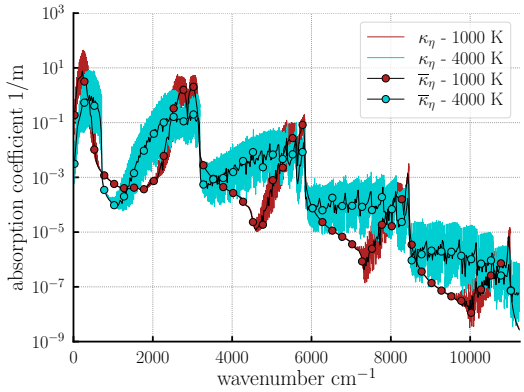

Figure 7.1. Comparison of line-by-line and SNBW emissivities absorption coefficients. Pressure is 40 bar and x_{HCl} is 0.5.

Comparison of emissivities in Fig. 7.2 shows that the effect of HCl is not negligible (although small), being 20% for a propellant composition with 15% HTPB and 20% Al. Moreover, it can be seen how the SNBW emissivities are in good agreement with the LBL results.

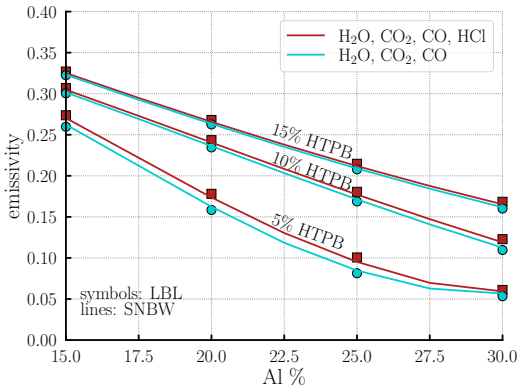

Figure 7.2. Comparison of line-by-line and SNBW emissivities for Al-NH_4ClO_4-HTPB solid propellant at 20 bar and $L = 1$ m. Temperature and molar fractions are computed from CEA.

7.2 Modeling of particle and gas radiation

Computing the radiative wall heat flux in a SRM environment requires to take into account several phenomena, including the spectral dependence of radiation, the contribution of gas and particles of different sizes, and the strong scattering characteristics of alumina. The theoretical, numerical, and computational challenges are such that all this effects cannot usually be considered in practical engineering scenarios, and simplifying assumptions have to be made. Aim of this section is to assess the effect of such assumptions.

For the sake of simplicity, a single propellant formulation is taken into consideration, taken from [146]. The propellant is composed by 18% Al, 14% HTPB, 67.5% NH_4ClO_4, and 0.5% Fe_2O_3, and the chamber and throat compositions and temperature as computed from NASA CEA [74] are reported in Tab. 7.1. This propellant formulation has been chosen because the particle volume distribution has been measured [146] and is reported in Fig. 7.3. The distribution is bimodal, with a first peak at $D = 1.44$ μm and the second for $D = 157$ μm. As discussed also in Sec. 3.3, the radiative properties of a particle cloud are weighted with number distribution f_N, which can be computed dividing the volume percentage by the particle volume. The resulting distribution, as shown in Fig. 7.3, is monomodal, and can be well approximated by a log-normal distribution [13]

$$f_N = \frac{1}{D \ln(\sigma_g)\sqrt{2\pi}} e^{-\frac{\ln\left(\frac{D}{D_m}\right)^2}{2\ln(\sigma_g)^2}}$$

with $D_m = 0.44$ μm and $\sigma_g = 1.6685$ (both parameters have been computed fitting the experimental data on a log-normal curve with a least-square algorithm). The

second peak of the volume distribution vanishes due the fact that the larger particles are quite few, despite having a considerable mass and volume, and have therefore little influence on the overall radiative properties of the medium.

Table 7.1. CEA results for the selected propellant formulation.

location	p,bar	T, K	ρ, kg/m^3	y_{H_2O}	y_{CO_2}	y_{CO}	y_{HCl}	$y_{AL_2O_3}$
chamber	32	3319.73	3.1673	0.05924	0.0142	0.2768	0.178	0.303
throat	18.483	3139.69	1.9505	0.05603	0.0137	0.2772	0.186	0.3165

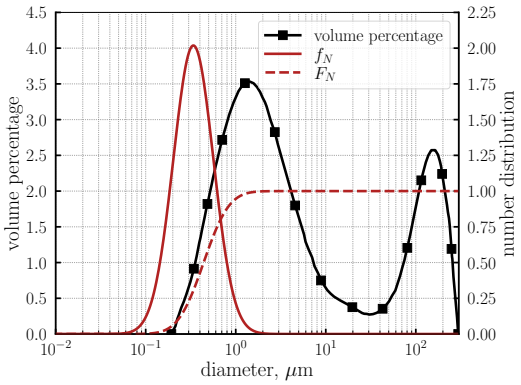

Figure 7.3. Particle distribution (f_N is the probability density function, F_N is the cumulative density function).

Once the particle number distribution is known, one can compute the absorption and scattering coefficients of the particle cloud, recalling that

$$\kappa_{\text{abs/sca}} = N_p \int_0^\infty \frac{\pi}{4} D^2 Q_{\text{abs/sca}}(D) f_N(D) d(D)$$

being N_p the particle number density and $Q_{\text{abs/sca}}$ the absorption/scattering efficiency, computed from the Mie theory. Focusing on the chamber conditions, and employing for the alumina density the following expression [111, 147]

$$\rho_p = 1980 - 1.13(T - 2327) = 1858.2151 \quad \text{kg/m}^3$$

we can compute the average volume

$$\bar{V} = \int_d \frac{\pi}{6} D^3 f_N(D) d(D) = 1.450827 \times 10^{-01} \quad \mu\text{m}^3$$

and the particle number density

$$N_p = \frac{\rho_m y_p}{\rho_p \bar{V}} = 3.55975 \times 10^{15} \quad 1/\text{m}^3$$

The resulting absorption and scattering coefficients are shown in Figs. 7.4(a) and 7.4(b), together with the ones obtained considering monodisperse distributions at several diameters between 0.1 and 0.9 μm. From this comparison we can deduce that:

1. The coefficients computed from the polydisperse distribution are approximately one order of magnitude lower than the ones obtained from a monodisperse distribution employing the mean diameter D_m. This results from the fact that the absorption and scattering efficiencies have a strong dependency on the particle diameter and that the particle density of the polydisperse distribution is smaller than the one computed at D_m, since the average volume is larger than $V(D_m) = \pi/6 D_m^3 = 0.0446\ \mu\text{m}^3$.

2. The polydisperse curve is smoother than the monodisperse ones. In fact, integrating over the number distribution averages out the oscillations of the monodisperse results.

3. The scattering coefficient is significantly larger than the absorption one, confirming how radiation in SRMs is a scattering-driven problem.

4. Both optical coefficients are not constant along the spectrum, but rather decrease quite sharply for increasing λ. This suggests that the gray medium assumption may not be always applicable, despite its common use in the literature.

For what concerns the scattering function, a comparison is performed in Fig. 7.4(c) at three wavelengths. At 10 μm the two functions are identical, whereas some differences can be appreciated at lower wavelengths. Since there is no dependence from the particle density, the difference between monodisperse and polydisperse results is smaller than for the optical coefficients.

It can be of interest to analyze wether including the gas contribution in the absorption coefficient has any effect. Figure 7.5(b) shows the absorption coefficient of gas and particles, which are of the same order of magnitude. In particular, the gas absorption coefficient is larger than the particle one for $\lambda > 2$ μm. However, we have to recall that in RTE the absorption coefficient appears always summed to the scattering coefficient (their sum is the extinction coefficient $\kappa_{\text{ext}} = \kappa_{\text{abs}} + \kappa_{\text{sca}}$), which is reported in Fig. 7.5(a). The particle scattering coefficient is so large that the gas contribution is appreciable only at large wavelengths (4-6 μm), which however do not cover a significant share of the energy emitted by the medium, which is in the 0-4 μm range. We can therefore conclude that, in the present case, gas radiation is negligible, but that a small effect may be present in other scenarios. For example, the gas contribution was quantified to be around 10% in [60].

To analyze how the wall heat flux is influenced by the different modeling assumptions discussed above, a simplified test case is employed, consisting of an homogeneous plane slab of length L filled by the combustion products. In fact, spectral and non-isotropically scattering simulations are too computationally intensive to be performed on full SRMs with the current DTM tool. For the sake of simplicity, only particles are taken into consideration, since it has been shown in Fig. 7.5 that the gas absorption coefficient has little effect on the overall extinction. One could argue that after the throat, if a particle free zone is present, gas could have a more prominent role. However, since the temperature drops quickly in the nozzle, the overall importance of radiation is small. The walls are considered black and at a fixed temperature of 2500 K, which is compatible with wall temperatures of

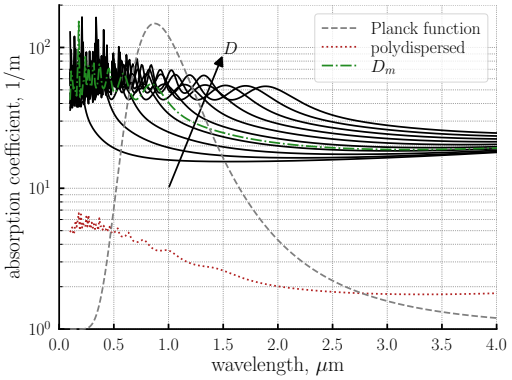

(a) Absorption coefficient.

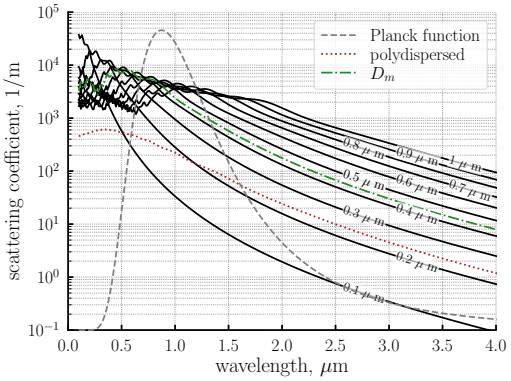

(b) Scattering coefficient.

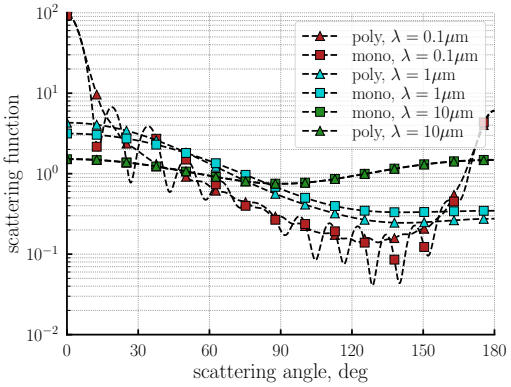

(c) Scattering function.

Figure 7.4. Comparison of optical properties of monodisperse and polydisperse particle clouds.

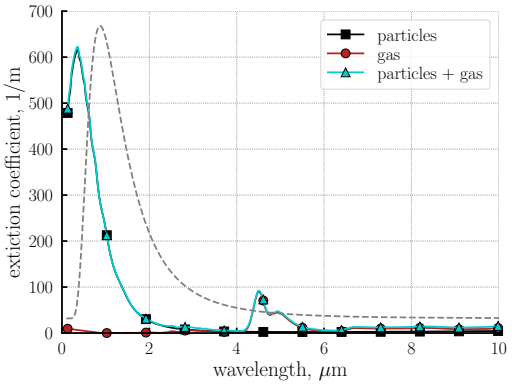

(a) Extiction.

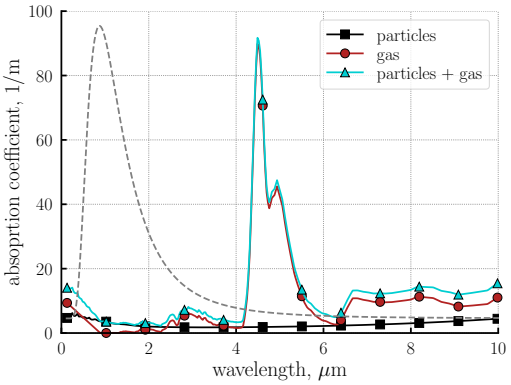

(b) Absorption.

Figure 7.5. Effect of gas absorption coefficient.

SRM thermal protection systems. Since taking into account anisotropic scattering with the DTM algorithm is cumbersome, a 1D discrete ordinates code has been

employed for this analysis (see Appendix A4 for its description and verification). The results are reported in Fig. 7.6. As expected, the monodisperse approximation (red) leads to large errors, especially at low L. On the other hand, computations without scattering (green) are in agreement with the reference (black) at low L, but have a significant overestimation at $L = 1$ m. This is due to the fact that without scattering the heat flux is able to reach the black-body limit (dashed line), while with scattering the effective emissivity of the medium is reduced. The assumption of isotropic scattering (pale blue) and gray medium (orange) do not induce significant errors if considered separately.

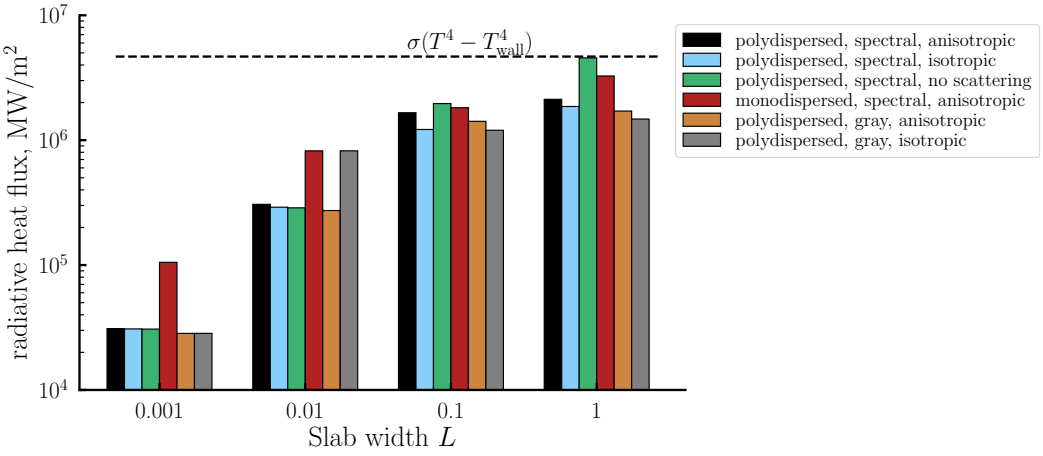

Figure 7.6. Wall heat flux for 1D slab.

7.3 Radiative heat transfer in HIPPO rocket motor

The goal of this section is to evaluate the radiative heat flux on a real SRM test case, comparing it to the convective heat flux and assessing its impact on the thermal protection system. The test case considered here is a firing test of the HIPPO motor [148], which was a sub-scale Space Shuttle solid propellant booster with a carbon-phenolic nozzle (6.35 cm of throat diameter). All computations performed in this section are based on the CFD results of [88], where a comprehensive analysis on the effect of multi-phase flow on convective heat flux and throat erosion was carried out. We employ here the same computational setup and simulations, focusing instead on the evaluation of the radiative heat flux. For the sake of simplicity no coupling between CFD and radiation have been performed.

7.3.1 Numerical setup

The numerical setup is reported in Fig. 7.7. It consists of the sole nozzle of the motor, since the details of the grain geometry are not available. Moreover, given that the optical coefficients of the particles are very large, it is expected that only the radiation emitted close to the wall has a real impact on the wall heat flux; therefore including the combustion chamber in the radiative simulations is not important. A

more detailed analysis on the effect of the adopted setup on the flowfield is presented in [88].

The computational grid is structured and composed of 150 × 80 control volumes. On the left-hand side particles and gases are injected at equilibrium conditions. For the propellant under consideration, composed of 70% ammonium perchlorate, 16% aluminum, 12% PBAN and curing agents, the combustion product composition as computed form CEA is reported in Tab. 7.2. On the right-hand side, since the flow is supersonic, an extrapolation boundary condition is employed. The nozzle wall is simulated as a non-reflective boundary for particles and as an ablative wall for the gas phase, employing the model reported in Sec. 2.7.2. On the axis and lateral faces symmetry conditions are enforced.

Table 7.2. Inflow mass fractions at average chamber pressure conditions.

Phase	y_{AlOH}	$y_{Al_2O_3}$	y_{CO}	y_{CO_2}	y_{Cl}	y_{H}	y_{H_2}	y_{HCl}	y_{H_2O}	y_{N_2}	y_{OH}	sum
Gas	0.008	-	0.247	0.025	0.018	0.002	0.020	0.199	0.094	0.088	0.006	0.707
Condensed	-	0.293	-	-	-	-	-	-	-	-	-	0.293

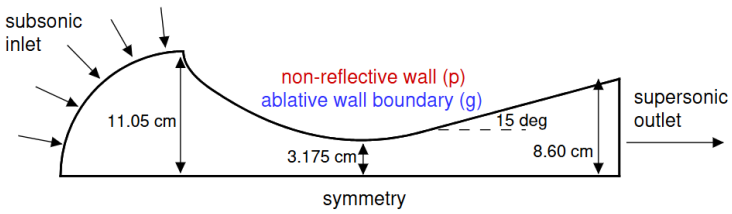

(a) Computational setup.

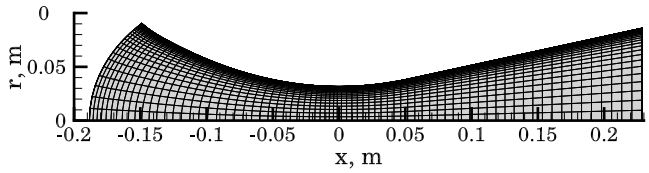

(b) Computational grid (only one every two cells is shown for clarity).

Figure 7.7. HIPPO test case.

7.3.2 Results

Simulations have been carried out for several particle diameters, ranging from 1 μm to 50 μm, employing a monodisperse distribution. Figure 7.8 reports the temperature, particle number density and optical coefficients fields, computed with the gray medium assumption, for the case $D = 1$ μm. For what concerns the radiative properties, it can be seen that, as expected, the particle absorption coefficient is significantly larger than the particle absorption coefficient, which is larger than the gas one. Both the scattering and absorption coefficients of the condensed phase show the same qualitative behavior of the particle number density.

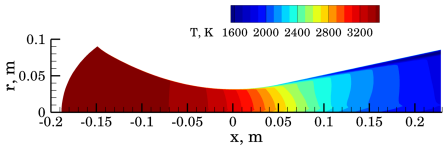

(a) Temperature.

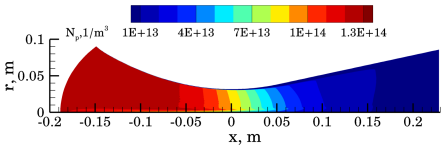

(b) Particle number density.

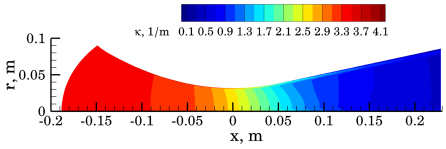

(c) Gas absorption coefficient.

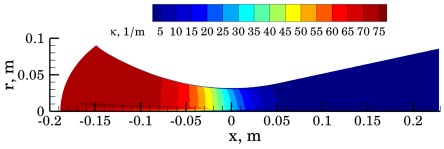

(d) Particle absorption coefficient.

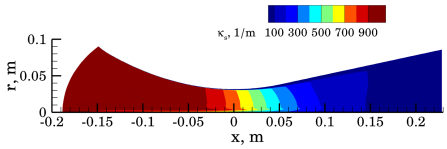

(e) Particle scattering coefficient.

Figure 7.8. Gas and particle radiative properties for $D_p = 1$ μm.

Figure 7.9 reports the convective and radiative wall heat fluxes. Due to the large computational cost of radiative calculations involving scattering, radiation is computed under the simplifying assumptions of gray medium and isotropic scattering. Despite the fact that these simplifying assumptions introduce discrepancies relative to the fully spectral and anisotropic treatment, they still provide the correct order of magnitude of the results.

It can be seen that radiation is comparable to convection at the start of the nozzle, and contributes to approximately 15% of the overall heat flux at the throat. Radiation becomes negative at $x = 0.05$ m, since the wall temperature remains high, while the flow cools during the expansion process.

While convection shows little dependence on the particle diameter above 2 μm, this is not the case for radiation, which shows a complex dependence on D. The peak q_{rad} increases by 75% increasing the particle diameter from 1 to 10 μm, and then decreases if the particle diameter is increased to 20 and 50 μm. This can be explained looking at the variation of the particle Planck-mean optical coefficients with particle diameter, reported in Fig. 7.10(a). Both coefficients show a non-monotonic behavior, resulting from the variation with diameter of N and Q (Fig. 7.10(b)). For small particles (roughly $D < 1$ μm) the increase of the optical efficiency Q with D is higher than the decrease of the particle number density with particle size, and both the scattering and absorption coefficients increase. For larger particles, instead, Q does not exhibit a strong dependency with D, and the particle number density becomes the driving factor. From this analysis two considerations can be made:

1. Thermal radiation may account for a large fraction of the overall wall heat

flux in SRM nozzles

2. The particle diameter has a huge influence on the computed radiation, since the optical coefficients vary significantly with D

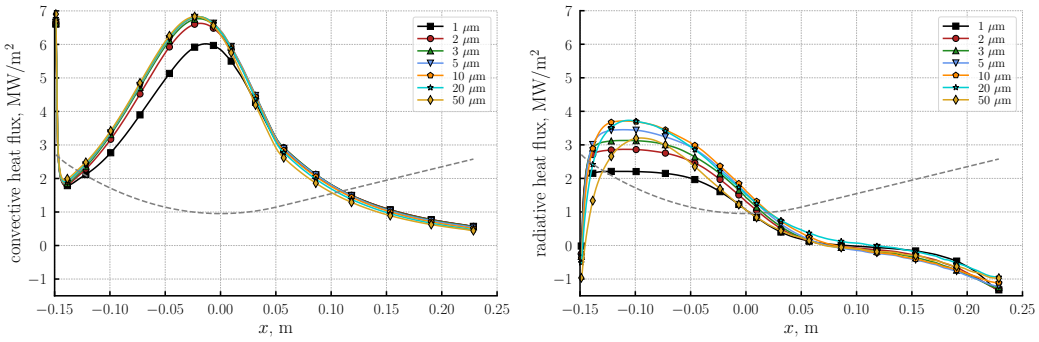

(a) Convection. (b) Radiation.

Figure 7.9. Wall heat flux.

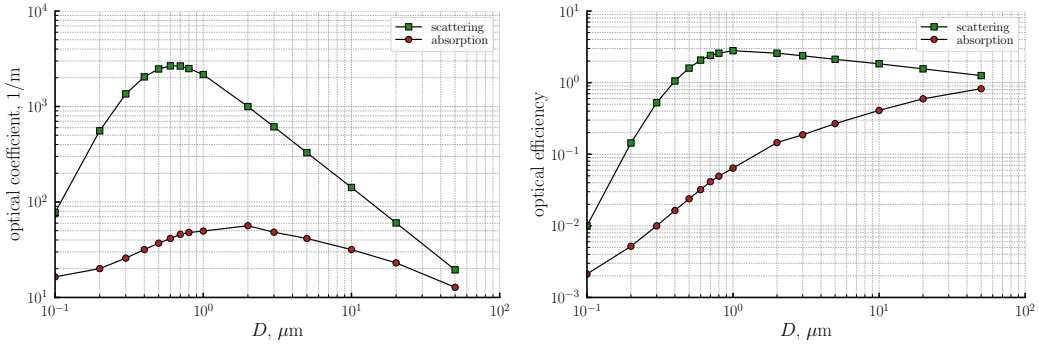

(a) Optical coefficient. (b) Optical efficiency.

Figure 7.10. Variation of optical properties with particle diameter.

All simulations presented in this section have been performed without coupling the CFD and radiative computations. While this modeling choice has been driven by computational cost considerations, it is important to assess its effect on the presented results. Concerning the erosion rate, it was shown in [67] how including radiation has only a minor effect. This is consistent with the fact that thermochemical erosion is a diffusion-limited phenomenon and that thermal radiation does not influence the concentration of oxidizing species at the wall. The larger wall heat flux should therefore result in a larger wall temperature, but without any relevant effect on the ablation rate. This means that, while radiation affects significantly the temperature distribution of the thermal protection system, an exact quantification of the impinging heat flux is not necessary for the evaluation of the ablation rate. To assess instead the effect of the coupling of radiation and flow energy equation one has to quantify the radiative heat flux divergence, reported in Fig. 7.11 for the

case $D = 1$ μm. Except near the boundaries, where temperature gradients are large, $\nabla \cdot q$ is relatively small, with an average value on the centerline in the convergent part of the nozzle of -5×10^{-7} W/m^3. To assess its effect on the energy equation, the same simplified analysis of Sec. 6.2.1.2 can be performed, employing a 1D approach

$$\Delta T = \frac{\nabla \cdot q_{\text{rad}} L}{\rho u c_p}$$

Considering for ρ, u, and c_p the values at the nozzle inlet, and a constant value of $\nabla \cdot q = -5 \times 10^7$ W/m^3, one gets a -4 K temperature decrease for a 0.1 m length, meaning that radiation is not expected to alter the flowfield far from the boundaries. However, the steep temperature (and optical properties) gradients in the boundary layer lead to a sharp increase of $\nabla \cdot q$, up to 10^9 W/m^3, meaning that coupling between radiation and CFD flowfield may impact the boundary layer structure. This is consistent with the results shown in [65], where it was shown that CFD-radiation coupling significantly impacted the convective wall heat flux.

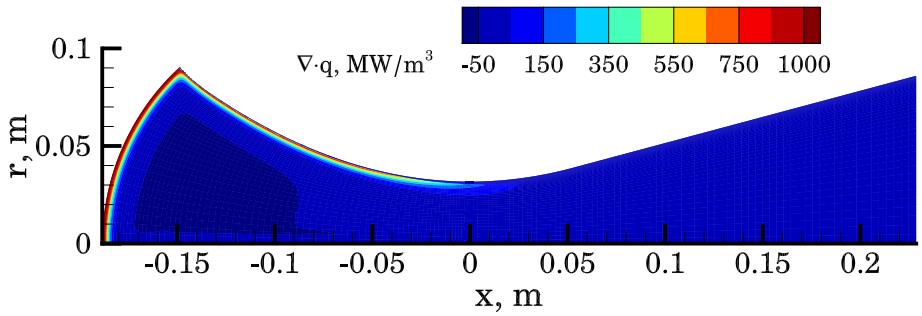

Figure 7.11. Radiative source term field for $D_p = 1$ μm.

7.4 Concluding remarks

The numerical investigation has demonstrated that the dispersed phase is the dominant factor in the determination of the radiative heat flux in SRMs. A key finding of this study is that radiation transport is primarily driven by scattering processes rather than absorption. Moreover, analysis performed on simplified test cases indicates that accounting for the polydisperse particle distribution distribution and including anisotropic scattering effects is essential for physical accuracy, despite the significant computational cost required by these models.

Furthermore, simulations conducted on a solid rocket motor nozzle show that in the convergent section the radiative heat flux can be equal to or even exceed the convective load. This result highlights that radiative transport is not a secondary effect in solid propulsion, but a primary component of the thermal environment.

Chapter 8

Conclusions

This thesis presented a unified computational framework for the analysis of radiative heat transfer in chemical rocket engines, encompassing liquid, hybrid, and solid propulsion systems. The main objective was to quantify the contribution of radiation to the overall thermal balance and to assess the accuracy of different modeling approaches under representative operating conditions. The developed methodology combined detailed spectroscopic descriptions of gas and particle radiation with a discrete transfer solution of the radiative transfer equation, integrated into a CFD solver for compressible, turbulent, and reactive flows.

Liquid rocket engines

For liquid rocket engines, radiation was examined in oxygen–hydrogen and oxygen–methane systems, covering a wide range of pressures and equivalence ratios. The comparison among spectral models demonstrated the need for approaches specifically validated for LRE conditions. Line-by-Line and Statistical Narrow Band calculations were used as reference, and two WSGGs for LOX-LH2 and LOX-LCH4 combustion products were developed to reduce the computational cost associated with spectral calculations. A 1D model was developed to perform fast radiative calculations, without the need for complex CFD simulations. The model, employing chemical equilibrium calculations, the aforementioned WSGGs, and semi-analytical models for the radiative heat flux in plane and cylindrical enclosures, showed excellent agreement with full CFD-DTM results.

Hybrid rocket engines

Radiation modeling can play a critical role in hybrid rocket engines, where heat transfer directly controls the regression rate of the solid fuel. The numerical reconstruction of several oxygen–HTPB firing tests demonstrated that neglecting radiation leads to an underestimation of the regression rate, particularly at low oxidizer mass fluxes. The inclusion of gas and soot radiation improved the agreement with experiments, indicating that the radiative contribution to the total surface heat flux can reach 20–30% under typical conditions.

Among the various radiation sources, soot was found to dominate due to its

strong absorption and emission characteristics. The formation and oxidation of soot were modeled using simplified transport–reaction equations, which allowed efficient coupling with CFD without prohibitive computational cost. The results emphasize the importance of soot modeling in the prediction of hybrid rocket performance and support the use of radiation-inclusive models in future design studies.

Solid rocket motors

The investigation of solid rocket motors focused on alumina particle radiation within the nozzle. The modeling approach accounted for absorption, emission, and anisotropic scattering through Mie theory, and was applied to both simplified one-dimensional test cases and a reference nozzle geometry. The simulations confirmed that particle radiation is the dominant radiative mechanism, while gas radiation plays a secondary role.

The optical behavior of the particle cloud was shown to depend strongly on the assumed particle size distribution. In particular, taking into account a polydisperse distribution leads to absorption and scattering coefficients which are one order of magnitude lower than the ones yielded by monodisperse distributions. The computed radiative heat fluxes were found to be comparable to, or even exceed, the convective ones in the convergent section of the nozzle. These findings underline the need for accurate particle property models and for experimental data on radiative fluxes under SRM operating conditions.

General Remarks

Across all engine types, the study confirmed that radiative heat transfer is a non-negligible contributor to the thermal load, particularly under high-temperature and particle-laden conditions. Despite the inherent complexity of the radiative transfer equation, the discrete transfer method proved capable of resolving multidimensional radiation fields with acceptable computational effort. The use of reduced-order models offers a practical pathway for integrating radiation into routine propulsion simulations. The lack of comprehensive experimental data remains a major limitation for model validation, especially regarding high-pressure gas radiation and soot or alumina optical properties. Nonetheless, the comparisons with available measurements and literature data demonstrated the physical consistency of the proposed framework.

Moreover, the findings of this research can improve future propulsion design practices, acting on two levels. On one hand, the study identifies the most appropriate computational and modeling tools for an accurate thermal loads estimation, offering designers a methodology for including radiation in multi-physics simulations. On the other hand, the analysis provides a quantitative assessment of radiative heat fluxes in representative test cases, giving a reliable benchmark for the expected thermal loads under realistic operating conditions.

In conclusion, this work provides a rigorous numerical foundation for incorporating radiation into rocket engine design and analysis. These models and findings enhance the understanding of thermal processes in propulsion systems and support the advancement of predictive tools for rocket engine design.

Appendix A1: DTM verification

This appendix reports several verification cases, designed to check the algorithm implementation.

A1.1 Test 1: homogeneous cube

The first test case consists of an homogeneous cube with $L = 1$ m, filled with a medium at 1000 K and fixed κ_{abs}. All walls are considered as cold and black. The cylinder is discretized with a $50 \times 50 \times 50$ grid. A reference analytical solution is computed for the wall heat flux and source term performing a numerical integration of the RTE over the solid angle. Three different values of κ_{abs} are considered: 0.1, 1, and 10 m^{-1}. The results are reported in Fig. A4.1, showing how a good agreement is obtained for all three cases.

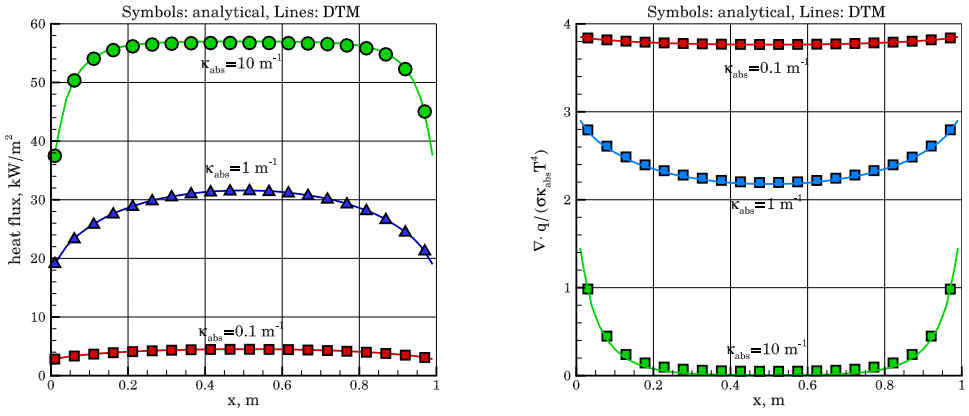

(a) Heat flux on the middle of the lateral wall. (b) Divergence of the heat flux for y=z=0.5 m.

Figure A1.1. DTM verification in a homogeneous cube.

Figure A1.2 reports a grid convergence analysis for the $\kappa_{\text{abs}} = 1$ m^{-1}, showing how 256 rays are more than enough to obtain an extremely good agreement with the experimental data (in the next test cases, whenever not specified, the number of rays is assumed to be equal to 256).

The cube test case has been employed also to check the implementation of the specular boundary condition. Two sub-domains have been selected, representative

of half and $1/8^{th}$ of the cube (Fig. A1.3). Comparison of the heat flux and its divergence between the three cases shows a perfect agreement (Fig. A1.4).

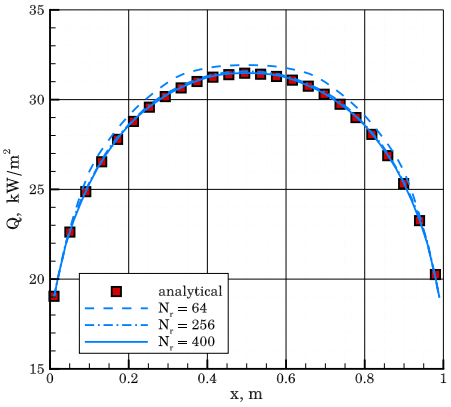

Figure A1.2. Grid convergence on the heat flux.

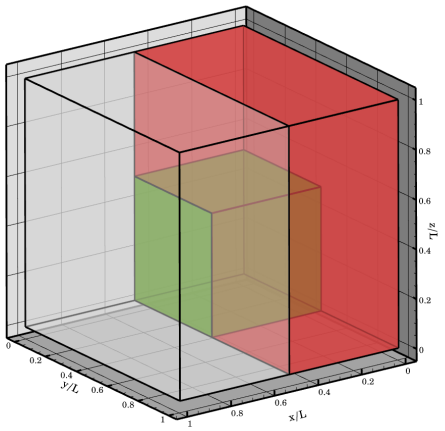

Figure A1.3. Setup for specular boundary condition verification.

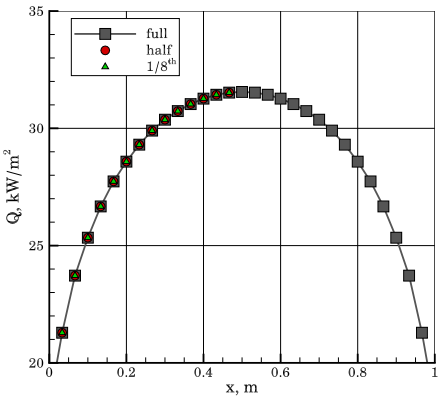

(a) Heat flux on the middle of the lateral wall.

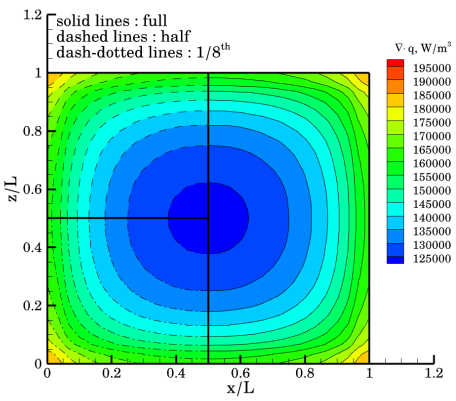

(b) Divergence of the heat flux for y=0.5 m.

Figure A1.4. DTM verification in a homogeneous cube with symmetry boundary condition.

A1.2 Test 2: furnace

The second test case is taken from [149]. It consists of a box-shaped enclosure with prescribed temperature field (Fig. A1.5) and uniform absorption coefficient $\kappa_{\text{abs}} = 0.3472\ \text{m}^{-1}$. The furnace is 5.76 m long and has a square cross section with a side of 0.96 m. A $100 \times 30 \times 30$ uniform grid is employed. This test allows to verify the code for non-homogeneous conditions. A reference solution, also taken from [149], is available, and is compared with the DTM results in Fig. A1.6, showing good results for both the heat flux and source terms.

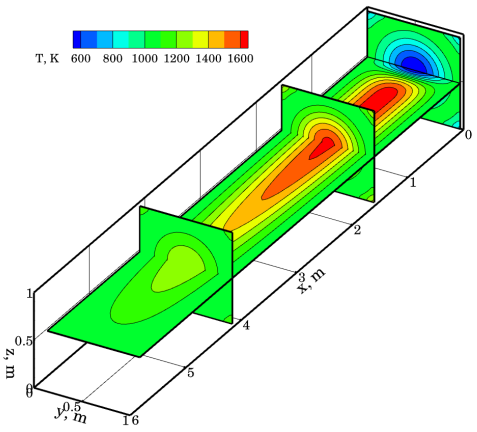

Figure A1.5. Box-shaped furnace.

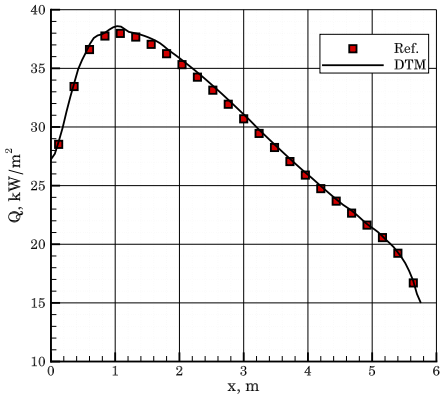

(a) Heat flux on the side wall (y = 0.6 m, z = 0 m).

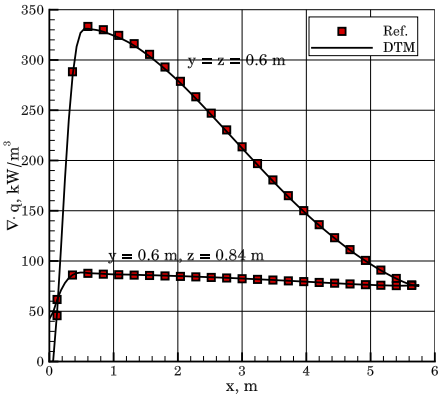

(b) Divergence of the heat flux.

Figure A1.6. DTM verification in a box-shaped furnace.

A1.3 Test 3: cylinder

The third test case consists of a cylinder of length 2 m and 1 m of radius. The cylinder is homogeneous with T= 3500 K and all walls are considered as cold and black. The test case is employed to verify the implementation of the wedge boundary condition, comparing the DTM results obtained with different cylinder apertures to analytical results. In particular, two cylinders are simulated, one with 45° aperture and one with 1° aperture (Fig. A1.7). Both cases adopt a uniform grid, consisting of $100 \times 50 \times 25$ cells in the 3D case and $100 \times 50 \times 1$ cells in the axisymmetric one. As shown in Fig. A1.8 the heat flux on the lateral wall is in perfect agreement in both cases with the exact solution.

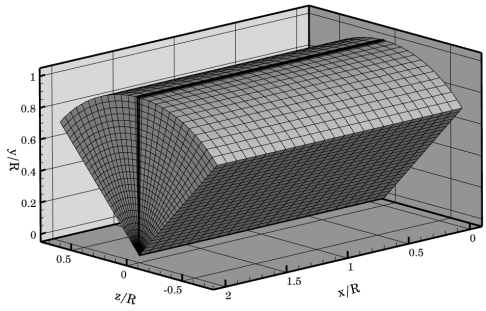

Figure A1.7. Cylinder computational setup.

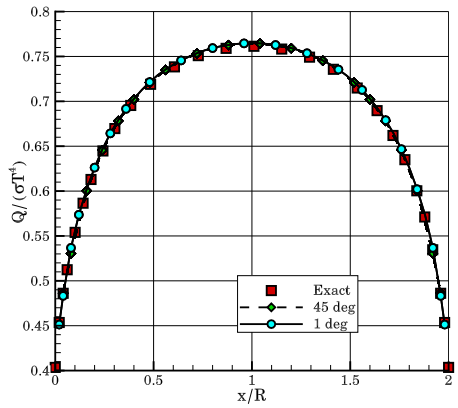

Figure A1.8. Heat flux on the lateral wall.

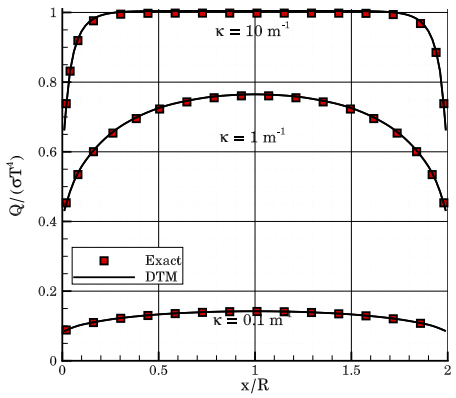

(a) Heat flux on the side wall.

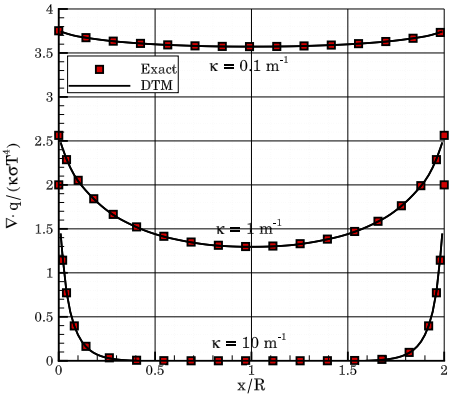

(b) Divergence of the heat flux on the cylinder axis.

Figure A1.9. DTM verification in a finite cylinder.

Given the importance of axisymmetric setups in the present work, a comparison is performed with the analytical solution for different values of the absorption coefficient in Fig. A1.9, with excellent results.

Finally, a grid convergence is performed on the heat flux at the middle of the cylinder, reported in Fig. A1.10. Results show how the error decreases as $1/N_r$.

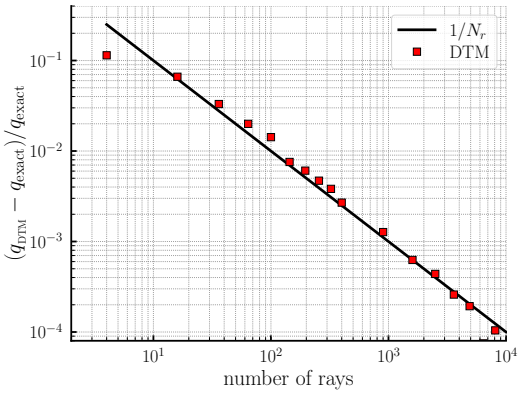

Figure A1.10. Grid convergence for the finite cylinder.

A1.4 Test 4: scattering medium

Test 4 is devised to check the DTM implementation for scattering medium, and is taken from [150]. In consists of a plane quadrilateral enclosure with sides of length 1 and a 60° inclination, divided into 30×30 cells. The medium is cold (0 K) and has an extinction coefficient $\beta = 1\ \mathrm{m}^{-1}$. All walls are black and also cold, with the exception of the bottom one, which is maintained at 1000 K. Figure A1.11 reports the non-dimensional heat flux on the right wall for two values of the scattering albedo $\omega = \kappa_{\mathrm{sca}}/\beta$ for isotropic scattering. The agreement with the reference data is excellent.

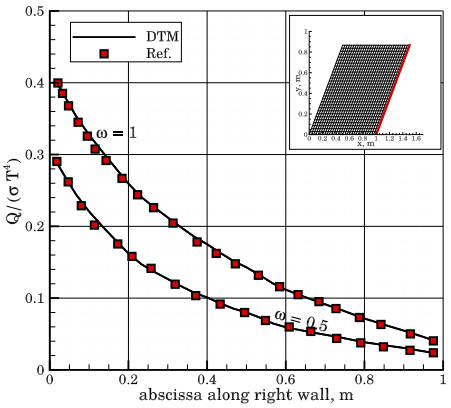

Figure A1.11. DTM verification for isotropic scattering.

A1.5 Test 5: non-cartesian grids

Test 5 aims at veryfing the code implementation for non-cartesian grids. It consists of an axisymmetric nozzle, discretized with two different grids, reported in Fig. A1.12(a). The first grid has the cell aligned with the x-y axes (H mesh), while the second is elliptic and is normal to the nozzle wall. Both consists of 100×30 cells. The medium is at 1000 K and has an absorption coefficient of 0.1 m^{-1}. All walls are cold and black. The heat flux computed with the two grids is reported in Fig. A1.12(b) and shows how the DTM results are independent of the grid choice.

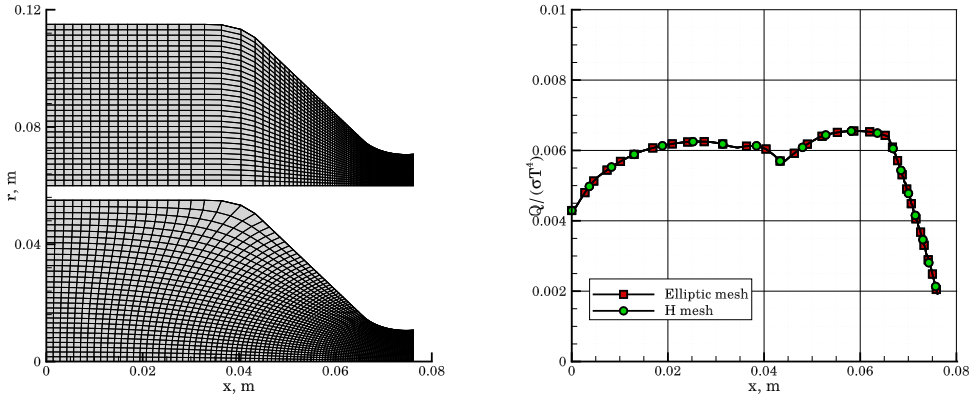

(a) Computational grids.

(b) Heat flux on the nozzle wall.

Figure A1.12. DTM verification for non-cartesian grids.

Appendix A2: WSGG coefficients

The model coefficients have been determined minimizing the difference between the emissivity computed with the proposed WSGG and the reference SNB model. The optimization procedure has been performed with a MATLAB software employing a nonlinear least squares algorithm. The procedure is briefly outlined below for the water vapor WSGG (Eq. (5.4)):

1. Reference emissivities have been generated with the SNB model for temperatures (1500 - 4000 K), pressures (1 - 300 bar), path lengths ($1\times10^{-4} - 1$ m), and molar fractions (0.1 - 1).

2. $N_g = 4$ and $T_{\text{ref}} = 2400$ K were selected according to the relevant literature [116, 117].

3. The SNB emissivity was fitted according to the proposed WSGG model (Eq. (5.4)), obtaining the c_{j,i_g} and κ_{i_g} coefficients for $i_g = 1, 2, 3, 4$.

4. For all temperatures in the specified range it was checked that the gray gas weight corresponding to the transparency window $a_0 = 1 - \sum_{i_g=1}^{N_g} a_{i_g}$ was non-negative [103].

For the H_2O-CO_2 WSGG (Eq. (5.5)) the same approach was followed, but the procedure was repeated for each value of Mr.

The values of the WSGG coefficients are reported below for H_2O (Eq. (5.4), in Table A2.1) and H_2O-CO_2 mixtures (Eq. (5.5), Tables A2.2 and A2.3). Moreover, a more extensive quantification of the errors produced in the estimation of the emissivity by the proposed WSGGs is performed comparing the predicted emissivities with the one predicted by the SNB approach in Fig. A2.1. It can be seen that the error is lower than 10% for $L \cdot x_{H_2O} \cdot p >$ 1 bar$\cdot$ m and for T between 1500 K and 4000 K, with most values below 4%. Use of the model at lower pressure path lengths is possible, but higher errors are introduced.

For what concerns the WSGG for H_2O-CO_2 mixtures, the emissivities are compared with SNB values in Fig. A2.2. The tested Mr values range from 0.125 to 8. It can be seen that the error remains consistently below 5% for almost all temperatures of interest and less than 10% for all pressure path lengths above 1 m$\cdot$ bar. In all the results presented in this work, whenever the value of Mr was not among those for which the coefficients have been explicitly calculated, the WSGG

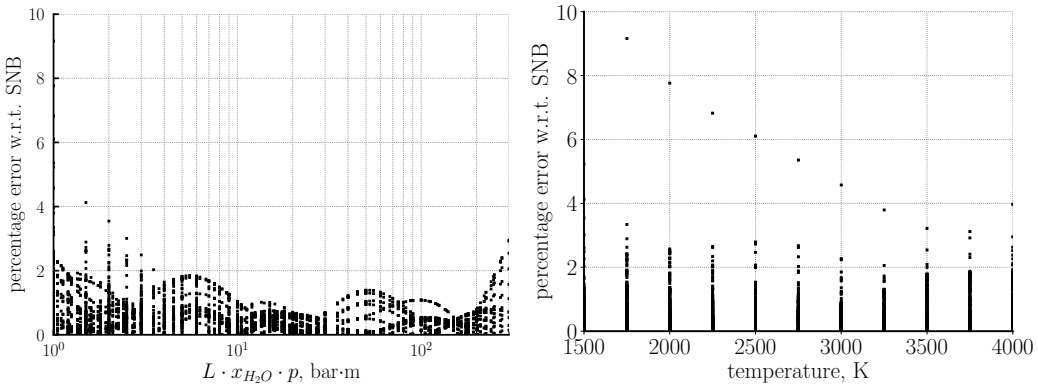

Figure A2.1. Error of the WSGG for H_2O for all points of the test matrix.

parameters corresponding to the closest value of Mr have been used, similarly to [116].

Care must be employed when applying the proposed WSGGs to CFD calculations, since temperature and pressure may fall outside the model calibration range. While it is recommended to limit both p and T so that they remain strictly inside the range listed in Sec. 5.1.2 and 5.2.2, the boundary values should be employed if there is a need to extend the original range.

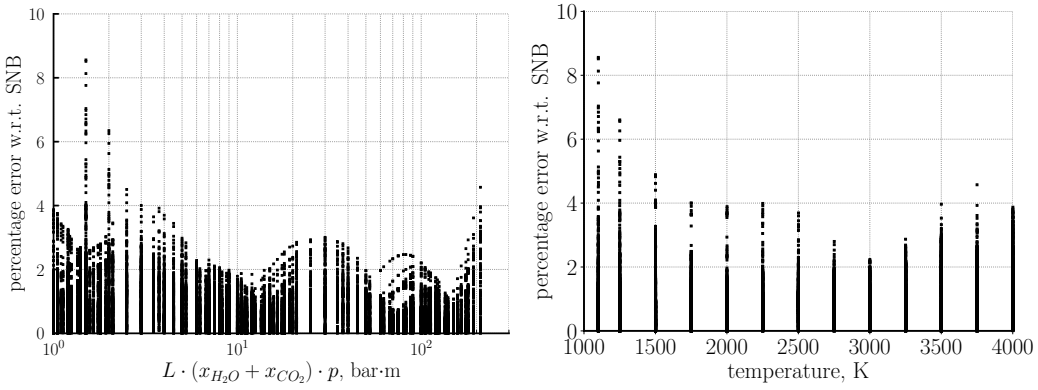

Figure A2.2. Error of the WSGG for H_2O-CO_2 for all points of the test matrix.

Table A2.1. WSGG coefficients for water vapor.

i_g	1	2	3	4
κ_{i_g}	0.014594	0.156390	0.967803	6.310879
c_{0,i_g}	0.120045	-0.306869	-0.080801	1.009603
c_{1,i_g}	0.126245	1.640970	1.163064	-1.917783
c_{2,i_g}	0.027891	-1.278695	-1.160097	1.244422
c_{3,i_g}	-0.040793	0.292618	0.314726	-0.274227

Table A2.2. WSGG coefficients for water vapor - carbon dioxide mixtures for $Mr = 0.125 - 1$.

i_g	1	2	3	4
		$Mr = 0.125$		
κ_{i_g}	0.018921	0.201355	2.177752	83.681211
c_{0,i_g}	-0.532591	0.338670	0.582898	0.198925
c_{1,i_g}	2.300377	0.126308	-0.935571	-0.301228
c_{2,i_g}	-1.761992	-0.373209	0.565397	0.165138
c_{3,i_g}	0.402114	0.123367	-0.120346	-0.031874
		$Mr = 0.250$		
κ_{i_g}	0.019695	0.176943	1.927536	68.107015
c_{0,i_g}	-0.396877	0.013091	0.728348	0.252767
c_{1,i_g}	1.790107	0.948018	-1.080919	-0.430343
c_{2,i_g}	-1.318230	-0.939157	0.581898	0.267167
c_{3,i_g}	0.291051	0.244841	-0.108590	-0.058113
		$Mr = 0.500$		
κ_{i_g}	0.018473	0.167276	1.952047	52.441380
c_{0,i_g}	-0.236388	-0.206884	0.725780	0.335381
c_{1,i_g}	1.262742	1.486154	-0.884108	-0.627902
c_{2,i_g}	-0.904787	-1.253509	0.345353	0.419616
c_{3,i_g}	0.195389	0.298121	-0.036283	-0.096346
		$Mr = 0.750$		
κ_{i_g}	0.017736	0.169308	1.969425	42.244993
c_{0,i_g}	-0.159840	-0.277568	0.670017	0.401490
c_{1,i_g}	1.029515	1.632683	-0.660894	-0.778331
c_{2,i_g}	-0.728327	-1.308007	0.137143	0.531477
c_{3,i_g}	0.155358	0.298863	0.020843	-0.123635
		$Mr = 1.000$		
κ_{i_g}	0.017628	0.174844	1.995313	36.680098
c_{0,i_g}	-0.120589	-0.302002	0.617410	0.450271
c_{1,i_g}	0.914228	1.667088	-0.486243	-0.887988
c_{2,i_g}	-0.640886	-1.300099	-0.015639	0.611855
c_{3,i_g}	0.135256	0.289894	0.061352	-0.142996

Table A2.3. WSGG coefficients for water vapor - carbon dioxide mixtures for $Mr = 2 - 8$.

i_g	1	2	3	4
		$Mr = 2.000$		
κ_{i_g}	0.017696	0.186016	1.950971	25.467792
c_{0,i_g}	-0.056075	-0.320818	0.458295	0.584577
c_{1,i_g}	0.724775	1.637206	-0.017773	-1.174975
c_{2,i_g}	-0.497380	-1.207716	-0.401982	0.814065
c_{3,i_g}	0.102112	0.254019	0.160087	-0.190224
		$Mr = 2.500$		
κ_{i_g}	0.017814	0.189185	1.928168	23.112324
c_{0,i_g}	-0.043536	-0.318111	0.406785	0.625255
c_{1,i_g}	0.687196	1.608209	0.124317	-1.259805
c_{2,i_g}	-0.468620	-1.169021	-0.514596	0.872198
c_{3,i_g}	0.095378	0.241602	0.188062	-0.203453
		$Mr = 3.000$		
κ_{i_g}	0.017914	0.191435	1.908193	21.511787
c_{0,i_g}	-0.035419	-0.314168	0.366303	0.656536
c_{1,i_g}	0.662399	1.581880	0.234028	-1.324673
c_{2,i_g}	-0.449544	-1.137337	-0.600378	0.916222
c_{3,i_g}	0.090890	0.231845	0.209141	-0.213366
		$Mr = 4.000$		
κ_{i_g}	0.018078	0.194536	1.878634	19.480684
c_{0,i_g}	-0.026015	-0.305586	0.306826	0.701315
c_{1,i_g}	0.632872	1.538113	0.392967	-1.417862
c_{2,i_g}	-0.426646	-1.089016	-0.723220	0.979208
c_{3,i_g}	0.085466	0.217523	0.239031	-0.227454
		$Mr = 6.000$		
κ_{i_g}	0.018294	0.198014	1.842568	17.336022
c_{0,i_g}	-0.018249	-0.290310	0.232303	0.755432
c_{1,i_g}	0.606954	1.475621	0.590153	-1.533041
c_{2,i_g}	-0.406312	-1.025942	-0.874267	1.057727
c_{3,i_g}	0.080618	0.199634	0.275481	-0.245063
		$Mr = 8.000$		
κ_{i_g}	0.018416	0.199856	1.820514	16.157754
c_{0,i_g}	-0.015392	-0.278339	0.185639	0.788192
c_{1,i_g}	0.596299	1.432731	0.713984	-1.605694
c_{2,i_g}	-0.397852	-0.985239	-0.969253	1.108504
c_{3,i_g}	0.078594	0.188458	0.298410	-0.256651

Appendix A3: Analytical solution for the radiative heat flux in a finite cylinder

In this appendix the analytical expressions for the radiative wall heat flux in an homogeneous cylinder with cold, black walls are obtained. The derivation is similar to the work of [151], but given that some differences in the angles and lengths are introduced, it is reported here for the sake of clarity and completeness.

Let us consider a finite cylinder of length $2L$ and radius R, with a cartesian reference frame (x, y, z) anchored to the middle point of the cylinder (see Fig. A3.1). Assuming that the medium can be treated as gray, and has a uniform intensity $\mathcal{I}_b$, and absorption coefficient κ, the wall heat flux impinging on a generic point $P_w = [x_0, R, 0]^T$ of the lateral wall can be written as

$$q = \int_\Omega \mathcal{I}_b \left(1 - e^{-\kappa t}\right) (\hat{\mathrm{s}} \cdot \hat{\mathrm{n}}) d\Omega \tag{A3.1}$$

where $\hat{\mathrm{s}}$ the direction versor, $\hat{\mathrm{n}}$ the normal to the wall, and t is the path length. To perform the integration we define a polar coordinate system (θ, ϕ), with θ taken from the x axis and ϕ taken anticlockwise around x. The generic ray $\vec{s}$ originating

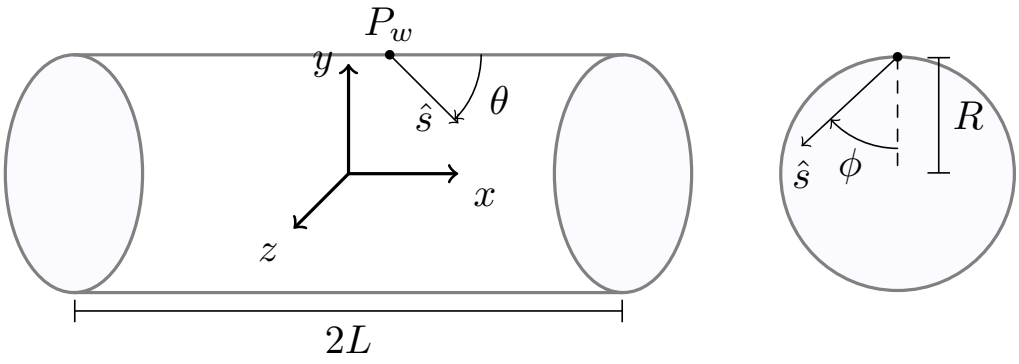

Figure A3.1. Finite cylinder and reference frames.

from P_w can therefore be expressed as

$$\vec{s} = \begin{bmatrix} x_0 \\ R \\ 0 \end{bmatrix} + \begin{bmatrix} \cos(\theta) \\ \sin(\theta)\cos(\phi) \\ \sin(\theta)\sin(\phi) \end{bmatrix} t \tag{A3.2}$$

The integration of the heat flux can be divided into three parts, separating those rays that intercept the front base, the rear base, and the lateral wall of the cylinder. To find the rays that intercept the front base we impose that $x = L$ and $y^2 + z^2 \leq R^2$, obtaining

$$t = \frac{+L - x_0}{\cos\theta} \tag{A3.3}$$

$$\theta \in \left[0, \theta_{\min} = \tan^{-1}\left(\frac{2R\cos\phi}{L - x_0}\right)\right] \tag{A3.4}$$

To find the rays that intercept the rear base we impose instead that $x = -L$ and $y^2 + z^2 \leq R^2$, obtaining

$$t = \frac{-L - x_0}{\cos\theta} \tag{A3.5}$$

$$\theta \in \left[\theta_{\max} = \pi - \tan^{-1}\left(\frac{2R\cos\phi}{L + x_0}\right), \pi\right] \tag{A3.6}$$

The rays that intercept the lateral wall of the cylinder are instead characterized by

$$t = \frac{2R\cos(\phi)}{\sin(\theta} \tag{A3.7}$$

$$\theta \in [\theta_{\min}, \theta_{\max}] \tag{A3.8}$$

The heat flux integration can thus be rewritten as

$$\begin{aligned} q = \mathcal{I}_b \int_0^{2\pi} \int_0^{\theta_{\min}} \left(1 - e^{-\kappa \frac{(L - x_0)}{\cos(\theta)}}\right) \sin^2(\theta)\cos(\phi) d\theta d\phi + \\ \mathcal{I}_b \int_0^{2\pi} \int_{\theta_{\min}}^{\theta_{\max}} \left(1 - e^{-\kappa \frac{2R\cos(\phi)}{\sin(\theta}}\right) \sin^2(\theta)\cos(\phi) d\theta d\phi + \\ \mathcal{I}_b \int_0^{2\pi} \int_{\theta_{\max}}^{\pi} \left(1 - e^{-\kappa \frac{(-L - x_0)}{\cos(\theta)}}\right) \sin^2(\theta)\cos(\phi) d\theta d\phi \end{aligned} \tag{A3.9}$$

where we have employed the fact that $\hat{\mathrm{s}} \cdot \hat{\mathrm{n}}$, being $\hat{\mathrm{n}}$ the normal to the wall, is equal to $\sin(\theta)\cos(\phi)$.

Appendix A4: Discrete ordinates code for plane medium

A4.1 Governing equations

The one-dimensional, plane-parallel radiative transfer equation for a non-gray, scattering medium is written as

$$\mu \frac{d\mathcal{I}_\lambda(x,\mu)}{dx} = -\beta_\lambda(x)\,\mathcal{I}_\lambda(x,\mu) + \kappa_{\mathrm{abs},\lambda}(x)\,\mathcal{I}_{b,\lambda}(T) + \frac{\kappa_{\mathrm{sca},\lambda}(x)}{2}\int_{-1}^{1} \Phi_\lambda(\mu,\mu')\,\mathcal{I}_\lambda(x,\mu')\,d\mu', \tag{A4.1}$$

where $\mathcal{I}_\lambda(x,\mu)$ is the spectral radiance, $\mu = \cos\theta$ is the direction cosine with respect to the slab normal, and the extinction coefficient is $\beta_\lambda = \kappa_{\mathrm{abs},\lambda} + \kappa_{\mathrm{sca},\lambda}$. The last term in Eq. (A4.1) accounts for in-scattering from all directions through the phase function $\Phi_\lambda(\mu,\mu')$, while $\mathcal{I}_{b,\lambda}(T)$ is the Planck spectral intensity.

Diffuse–gray boundary conditions are imposed at the two walls located at $x = 0$ and $x = L$:

$$\mathcal{I}_\lambda(0,\mu>0) = \varepsilon_1\,\mathcal{I}_{b,\lambda}(T_{w,1}) + (1-\varepsilon_1)\int_{-1}^{0} \mathcal{I}_\lambda(0,\mu')\,|\mu'|\,d\mu', \tag{A4.2}$$

$$\mathcal{I}_\lambda(L,\mu<0) = \varepsilon_2\,\mathcal{I}_{b,\lambda}(T_{w,2}) + (1-\varepsilon_2)\int_{0}^{1} \mathcal{I}_\lambda(L,\mu')\,\mu'\,d\mu', \tag{A4.3}$$

where ε_1 and ε_2 denote the wall emissivities, and $T_{\mathrm{wall},1}$ and $T_{\mathrm{wall},2}$ are the corresponding wall temperatures.

A4.2 Angular discretization: the discrete ordinates (S_N) method

The integral over solid angle in Eq. (A4.1) is approximated by a quadrature sum over a discrete set of ordinates $\{\mu_n, w_n\}$:

$$\int_{-1}^{1} f(\mu')\,d\mu' \;\approx\; \sum_{n=1}^{N} w_n\, f(\mu_n), \tag{A4.4}$$

where μ_n are the Gauss–Legendre abscissae and w_n are the associated weights. This converts Eq. (A4.1) into a system of N coupled first-order differential equations,

$$\mu_n \frac{d\mathcal{I}_{\lambda,n}(x)}{dx} = -\beta_\lambda \, \mathcal{I}_{\lambda,n}(x) + \kappa_{\mathrm{abs},\lambda} \, \mathcal{I}_{b,\lambda}(T) + \frac{\kappa_{\mathrm{sca},\lambda}}{2} \sum_{m=1}^{N} w_m \, \Phi_\lambda(\mu_n, \mu_m) \, \mathcal{I}_{\lambda,m}(x). \tag{A4.5}$$

The coupling among ordinates arises from the scattering source term.

A4.3 Representation of the scattering phase function

The azimuthally averaged phase function is expanded in a series of Legendre polynomials:

$$\Phi_\lambda(\mu, \mu') = \sum_{\ell=0}^{L_{\max}} \frac{2\ell + 1}{2} \, \beta_{\ell,\lambda} \, P_\ell(\mu) \, P_\ell(\mu'), \tag{A4.6}$$

where the coefficients $\beta_{\ell,\lambda}$ are the normalized Legendre moments of the phase function,

$$\beta_{\ell,\lambda} = \frac{1}{2} \int_0^\pi \Phi_\lambda(\theta) \, P_\ell(\cos\theta) \, \sin\theta \, d\theta. \tag{A4.7}$$

The coefficients $\beta_{\ell,\lambda}$ are computed from tabulated Mie-scattering data for each wavelength, after normalization such that $\int_0^\pi \Phi_\lambda(\theta) \sin\theta \, d\theta = 2$.

A4.4 Spatial discretization and numerical scheme

The spatial domain $[0, L]$ is divided into N_x uniform control volumes. Equation (A4.5) is solved for each ordinate μ_n using a first-order step scheme, which integrates the RTE analytically over each cell:

$$\mathcal{I}^{i+1}_{\lambda,n} = \mathcal{I}^{i}_{\lambda,n} \, e^{-\Delta\tau/|\mu_n|} + S^{i}_{\lambda,n} \left(1 - e^{-\Delta\tau/|\mu_n|}\right), \tag{A4.8}$$

where $\Delta\tau = \beta_\lambda \, \Delta x$ is the optical thickness of the cell, and $S^i_{\lambda,n}$ is the total source term,

$$S_{\lambda,n} = \frac{\kappa_{\mathrm{abs},\lambda}}{\beta_\lambda} \, \mathcal{I}_{b,\lambda}(T) + \frac{\kappa_{\mathrm{sca},\lambda}}{\beta_\lambda} \sum_{\ell=0}^{L_{\max}} \frac{2\ell + 1}{2} \, \beta_{\ell,\lambda} \, P_\ell(\mu_n) \, \phi_\ell(x) \tag{A4.9}$$

$$\phi_\ell(x) = \sum_{m=1}^{N} w_m \, P_\ell(\mu_m) \, \mathcal{I}_{\lambda,m}(x)$$

The source iteration continues until the intensity field converges below a prescribed tolerance.

A4.5 Spectral integration and radiative flux

The total radiative heat flux is obtained by integrating the spectral flux over all wavelengths,

$$q(x) = \int_0^\infty q_\lambda(x) \, d\lambda, \qquad q_\lambda(x) = 2\pi \sum_{n=1}^{N} w_n \, \mu_n \, \mathcal{I}_{\lambda,n}(x). \tag{A4.10}$$

Spectral quantities are evaluated on a user-defined wavelength grid, and the integration is performed numerically using the trapezoidal rule.

A4.6 Implementation details

The numerical algorithm was implemented in Python using `NumPy` for vectorized operations and `SciPy` for numerical integration and interpolation. Spectral absorption and scattering coefficients, $\kappa_{\mathrm{abs},\lambda}$ and $\kappa_{\mathrm{sca},\lambda}$, are read from tabulated data and interpolated onto the selected wavelength grid. The phase function is likewise obtained from Mie-scattering data, normalized, and projected onto Legendre polynomials to compute the coefficients $\beta_{\ell,\lambda}$. The solver supports both gray and non-gray calculations, isotropic or anisotropic scattering, and diffuse–gray boundaries with arbitrary wall temperatures. Convergence acceleration is optionally achieved through a simple Ng-type extrapolation applied to the Legendre moments during source iteration.

A4.7 Verification

To verify the code implementation two test cases are set up, representative of solid rocket motor conditions. Both consists of a gray medium with $T = 3500$ K and $T_{\mathrm{wall}} = 3000$ K, discretized 500 points and 256 angular ordinates. The first case cosists of a gray non-scattering medium. The DOM results are compared in Fig. A4.1(a) with the analytical solution (for further details the reader is referred to Chapter 13 of [7]), showing a good agreement. The second test case consists of a gray linear-anisotropically scattering medium, namely a medium whose phase function can be expressed as $\Phi = \frac{1}{2}(1 + a\cos(\theta))$. For three different values of a (-1,0,1), the DOM results are in excellent agreement with the exact solution, taken from [152], and are reported in Fig. A4.1(b).

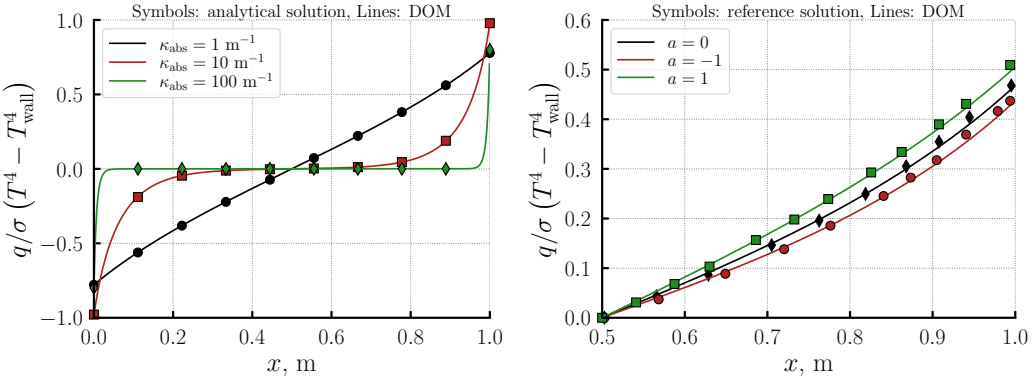

(a) Non-scattering case.

(b) Scattering case.

Figure A4.1. DOM verification.

Bibliography

[1] Sutton, G. P., and Biblarz, O., *Rocket Propulsion Elements*, 9th ed., John Wiley and Sons, Inc., New York, 2017.

[2] Sutton, G. P., *History of Liquid Propellant Rocket Engines*, AIAA, 2006. https://doi.org/10.2514/4.868870.

[3] Niederstrasser, C. G., "The small launch vehicle survey a 2021 update (The rockets are flying)," *Journal of Space Safety Engineering*, Vol. 9, No. 3, 2022, pp. 341–354. https://doi.org/10.1016/j.jsse.2022.07.003.

[4] Knab, O., Riedmann, H., Ivancic, B., Höglauer, C., Frey, M., and Aichner, T., "Consequences of modeling demands on numerical rocket thrust chamber flow simulation tools," *Progress in Propulsion Physics*, Vol. 11, 2019, pp. 317–346. https://doi.org/10.1051/eucass/201911317.

[5] Pizzarelli, M., and Battista, F., "Oxygen–methane rocket thrust chambers: Review of heat transfer experimental studies," *Acta Astronautica*, Vol. 209, 2023, pp. 48–66. https://doi.org/10.1016/j.actaastro.2023.04.028.

[6] Preclik, D., Knab, O., Gorgen, J., and Hagemann, G., "Simulation and Analysis of Thrust Chamber Flowfields: Cryogenic Propellant Rockets," *Liquid Rocket Thrust Chambers*, Progress in Astronautics and Aeronautics, Vol. 200, edited by V. Y. Michael Popp, James Hulka and M. Habiballah, AIAA, Reston, VA, 2004, pp. 527–551. https://doi.org/10.2514/5.9781600866760.0527.0551.

[7] Modest, M. F., and Mazumder, S., *Radiative Heat Transfer*, 4th ed., Academic Press, London, 2022. https://doi.org/10.1016/B978-0-12-818143-0.00005-5.

[8] Tien, C., "Thermal Radiation Properties of Gases," *Advances in Heat Transfer*, Vol. 5, 1969, pp. 253–324. https://doi.org/10.1016/S0065-2717(08)70131-X.

[9] Tucker, P., Menon, S., Merkle, C., Oefelein, J., and Yang, V., "Validation of High-Fidelity CFD Simulations for Rocket Injector Design," *44th AIAA/ASME/SAE/ASEE Joint Propulsion Conference & Exhibit*, 2008. https://doi.org/10.2514/6.2008-5226.

[10] Bartz, D., "Turbulent Boundary-Layer Heat Transfer from Rapidly Accelerating Flow of Rocket Combustion Gases and of Heated Air," Elsevier, 1965, pp. 1–108. https://doi.org/10.1016/S0065-2717(08)70261-2.

[11] Gulczyński, M. T., Vennitti, A., Scarlatella, G., Calabuig, G. J. D., Blondel-Canepari, L., Weber, F., Sarritzu, A., Bach, C., Deeken, J., Schmiel, T., Bianchi, D., and Pasini, A., "RLV applications: challenges and benefits of novel technologies for sustainable main stages," *72nd International Astronautical Congress (IAC-21), Dubai, Emirates*, 2021, pp. 1–20. IAC-21, D6, 2-D2.9,4, x64293.

[12] Brown, C. D., "Solid Rocket Systems," *Spacecraft Propulsion*, Education Series, AIAA, Reston, VA, 1996, pp. 135–166. https://doi.org/10.2514/5.9781600862441.0135.0166.

[13] Shimada, T., Daimon, Y., and Sekino, N., "Computational Fluid Dynamics of Multiphase Flows in Solid Rocket Motors," Tech. rep., Japan Aerospace Exploration Agency, 2006.

[14] Thakre, P., and Yang, V., "Chemical Erosion of Carbon-Carbon/Graphite Nozzles in Solid-Propellant Rocket Motors," *Journal of Propulsion and Power*, Vol. 24, No. 4, 2008, pp. 822–833. https://doi.org/10.2514/1.34946.

[15] Altman, D., and Holzman, A., "Overview and History of Hybrid Rocket Propulsion," *Fundamentals of Hybrid Rocket Combustion and Propulsion*, Progress in Astronautics and Aeronautics, Vol. 218, edited by K. K. Kuo and M. J. Chiaverini, AIAA, Reston, VA, 2007, pp. 1–36. https://doi.org/10.2514/5.9781600866876.0001.0036.

[16] Marxman, G. A., and Gilbert, M., "Turbulent Boundary Layer Combustion in the Hybrid Rocket," *Proceedings of the Ninth Symposium (International) on Combustion*, Academic Press, New York, USA, 1963, pp. 371–383. https://doi.org/10.1016/S0082-0784(63)80046-6.

[17] Glaser, C., Hijlkema, J., and Anthoine, J., "Evaluation of Regression Rate Enhancing Concepts and Techniques for Hybrid Rocket Engines," *Aerotecnica Missili & Spazio*, Vol. 101, 2022, pp. 267–292. https://doi.org/10.1007/s42496-022-00119-4.

[18] Gallo, G., Miyahara, Y., Kamps, L., and Nagata, H., "Regenerative cooling in hybrid rocket engines based on Self-Pressurized liquid nitrous oxide," *Applied Thermal Engineering*, Vol. 254, 2024, p. 123928. https://doi.org/10.1016/j.applthermaleng.2024.123928.

[19] Kanda, T., and Sato, M., "Radiative Heating in Combustion Chamber of Liquid Propellant Rocket Engines," *Transactions of the Japanese Society for Aeronautical and Space Sciences*, Vol. 59, No. 6, 2016, p. 332–339. https://doi.org/10.2322/tjsass.59.332.

[20] Consalvi, J., Andre, F., Coelho, F., Franca, F., Nmira, F., Galtier, M., Solovjov, V., and Webb, B., "Assessment of Engineering Gas Radiative Property Models in High Pressure Turbulent Jet Diffusion Flames," *Journal of Quantitative Spectroscopy and Radiative Transfer*, Vol. 253, 2020, p. 107169. https://doi.org/10.1016/j.jqsrt.2020.107169.

[21] Leccese, G., Bianchi, D., and Nasuti, F., "Numerical Investigation on Radiative Heat Loads in Liquid Rocket Thrust Chambers," *Journal of Propulsion and Power*, Vol. 35, No. 5, 2019, pp. 930–943. https://doi.org/10.2514/1.B37536.

[22] Wang, T.-S., "Multidimensional Unstructured-Grid Liquid Rocket-Engine Nozzle Performance and Heat Transfer Analysis," *Journal of Propulsion and Power*, Vol. 22, No. 1, 2006. https://doi.org/10.2514/1.14699.

[23] Thellmann, A., "Impact of Gas Radiation on Viscous Flows, in Particular on Wall Heat Loads, in Hydrogen–Oxygen vs. Methane– Oxygen Systems, Based on the SSME Main Combustion Chamber," Ph.D. thesis, Bundeswehr Universität Munich, Neubiberg, Germany, 2010.

[24] Naraghi, M., Dunn, S., and Coats, D., "Modeling of Radiation Heat Transfer in Liquid Rocket Engines," AIAA Paper 2005-3935, July 2005. https://doi.org/10.2514/6.2005-3935.

[25] Denison, M. K., and Webb, B. W., "A Spectral Line-Based Weighted-Sum-of-Gray-Gases Model for Arbitrary RTE Solvers," *Journal of Heat Transfer*, Vol. 115, No. 4, 1993, pp. 1004–1012. https://doi.org/10.1115/1.2911354.

[26] Reardon, J. E., and Lee, Y. C., "A Computer Program for Thermal Radiation from Gaseous Rocket Exhaust Plumes (GASRAD)," Tech. rep., NASA CR 161496, December 1979.

[27] Denison, M., and Webb, B., "An Absorption-Line Blackbody Distribution Function for Efficient Calculation of Total Gas Radiative Transfer," *Journal of Quantitative Spectroscopy and Radiative Transfer*, Vol. 50, No. 5, 1993, pp. 499–510. https://doi.org/10.1016/0022-4073(93)90043-H.

[28] Smith, T. F., Shen, Z. F., and Friedman, J. N., "Evaluation of Coefficients for the Weighted Sum of Gray Gases Model ." *Journal of Heat Transfer*, Vol. 104, No. 4, 1982, pp. 602–608. https://doi.org/10.1115/1.3245174.

[29] Bo Li, W. Y., and Fan, X., "Evaluation of the influence of radiation on a GH2/GO2 rocket combustor," *AIAA Propulsion and Energy Forum*, 2020. https://doi.org/10.2514/6.2020-3724.

[30] Badinand, T., and Fransson, T. H., "Radiative Heat Transfer in Film-Cooled Liquid Rocket Engine Nozzles," *Journal of Thermophysics and Heat Transfer*, Vol. 17, No. 1, 2003. https://doi.org/10.2514/2.6748.

[31] Goebel, F., Kniesner, B., Frey, M., Knab, O., and Mundt, C., "Radiative Heat Transfer Analysis in Modern Rocket Combustion Chambers," *CEAS Space Journal*, Vol. 6, 2014, pp. 79–98. https://doi.org/10.1007/s12567-014-0060-2.

[32] Harvazinski, M. E., Mehta, R., and Venugopalan, V., "Liquid Rocket Engine Combustion Simulations with Radiation Heat Transfer," *AIAA SCITECH 2024 Forum*, 2024. https://doi.org/10.2514/6.2024-0149.

[33] Xu, X., Chen, Y. L., and Wang, H. F., "Detailed numerical simulation of thermal radiation influence in Sandia Flame D," *International Journal of Heat and Mass Transfer*, Vol. 49, No. 11–12, 2006, pp. 2347–2355. https://doi.org/10.1016/j.ijheatmasstransfer.2005.07.032.

[34] De Flora, M. G., and Bruno, C., "Analysis of Soot and of Its Radiative Power in Supercritical LOX/LHC Rocket Combustion Chambers," *41st AIAA/ASME/SAE/ASEE Joint Propulsion Conference & Exhibit*, 2005. https://doi.org/10.2514/6.2005-4439.

[35] Byun, D., and Baek, S. W., "Numerical Investigation of Combustion with Non-Gray Thermal Radiation and Soot Formation Effect in a Liquid Rocket Engine," *International Journal of Heat and Mass Transfer*, Vol. 50, 2007, pp. 412–422. https://doi.org/10.1016/j.ijheatmasstransfer.2006.09.020.

[36] Kuo, K. K., Lu, Y.-C., Chiaverini, M. J., Johnson, D. K., Serin, N., Risha, G. A., Merkle, C. L., and Venkateswaran, S., "Fundamental Phenomena of Fuel Decomposition and Boundar-Layer Combustion Processes with Applications to Hybrid Rocket Motors," Tech. rep., Propulsion Engineering Research Center Penn State University, 1996.

[37] Strand, L., Jones, M., Ray, R., and Cohen, N., "Characterization of hybrid rocket internal heat flux and HTPB fuel pyrolysis," *30th Joint Propulsion Conference and Exhibit*, 1994. https://doi.org/10.2514/6.1994-2876.

[38] Farbar, E., Louwers, J., and Kaya, T., "Investigation of Metallized and Nonmetallized Hydroxyl Terminated Polybutadiene/Hydrogen Peroxide Hybrid Rockets," *Journal of Propulsion and Power*, Vol. 23, No. 2, 2007, pp. 476–486. https://doi.org/10.2514/1.22091.

[39] Migliorino, M. T., Bianchi, D., and Nasuti, F., "Numerical Analysis of Paraffin-Wax/Oxygen Hybrid Rocket Engines," *Journal of Propulsion and Power*, Vol. 36, No. 6, 2020, pp. 806–819. https://doi.org/10.2514/1.B37914.

[40] Bianchi, D., Leccese, G., Nasuti, F., Onofri, M., and Carmicino, C., "Modeling of High Density Polyethylene Regression Rate in the Simulation of Hybrid Rocket Flowfields," *Aerospace*, Vol. 6, No. 8, 2019. https://doi.org/10.3390/aerospace6080088.

[41] Funami, Y., and Shimada, T., "Numerical Evaluation of Hybrid Rocket Internal Ballistics with Thermal Radiation Effect," *Transactions of the Japan Society for Aeronautical and Space Sciences, Aerospace Technology Japan*, Vol. 12, No. ists29, 2014, pp. 21–0. https://doi.org/10.2322/tastj.12.Pa_21.

[42] Sankaran, V., "Computational Fluid Dynamics Modeling of Hybrid Rocket Flowfields," *Fundamentals of Hybrid Rocket Combustion and Propulsion*, Progress in Astronautics and Aeronautics, Vol. 218, edited by K. K. Kuo and M. J. Chiaverini, AIAA, Reston, VA, 2007, p. 323–350. https://doi.org/10.2514/5.9781600866876.0323.0350.

[43] Serin, N., and Gogus, Y., "Navier-Stokes Investigation on Reacting Flow Field of HTPB/O2 Hybrid Motor and Regression Rate Evaluation," *39th AIAA/ASME/SAE/ASEE Joint Propulsion Conference and Exhibit*, 2003. https://doi.org/10.2514/6.2003-4462.

[44] Naka, G., Carmicino, C., Messineo, J., Kitagawa, K., and Shimada, T., "Evaluation of Radiative Heat-Transfer Effect on Paraffin-Wax Regression Rate in Hybrid Rocket," *Journal of Propulsion and Power*, Vol. 39, No. 2, 2023, pp. 258–273. https://doi.org/10.2514/1.B38728.

[45] Chen, Y.-S., Chou, T., Gu, B., Wu, J., Wu, B., Lian, Y., and Yang, L., "Multiphysics simulations of rocket engine combustion," *Computers & Fluids*, Vol. 45, No. 1, 2011, pp. 29–36. https://doi.org/10.1016/j.compfluid.2010.09.010.

[46] Chiaverini, M. J., Kuo, K. K., Peretz, A., and Harting, G. C., "Regression-Rate and Heat-Transfer Correlations for Hybrid Rocket Combustion," *Journal of Propulsion and Power*, Vol. 17, No. 1, 2001. https://doi.org/10.2514/2.5714.

[47] Whitmore, S. A., and Merkley, S., "Radiation Heating Effects on Oxidizer-to-Fuel Ratio of Additively Manufactured Hybrid Rocket Fuels," *Journal of Propulsion and Power*, Vol. 35, No. 4, 2019, pp. 863–878. https://doi.org/10.2514/1.B37037.

[48] Kim, H.-J., and Kim, Y.-M., "Numerical modeling for combustion processes of hybrid rocket engine," *37th Joint Propulsion Conference and Exhibit*, 2001. https://doi.org/10.2514/6.2001-4504.

[49] Budzinski, K., Aphale, S. S., Ismael, E. K., Surina, G., and DesJardin, P. E., "Radiation heat transfer in ablating boundary layer combustion theory used for hybrid rocket motor analysis," *Combustion and Flame*, Vol. 217, 2020, pp. 248–261. https://doi.org/10.1016/j.combustflame.2020.04.011.

[50] Migliorino, M. T., Gubernari, G., Bianchi, D., Nasuti, F., Cardillo, D., and Battista, F., "Numerical Simulations of Fuel Shape Change in Paraffin-Oxygen Hybrid Rocket Engines," *Journal of Propulsion and Power*, Vol. 39, No. 6, 2023, pp. 785–799. https://doi.org/10.2514/1.B39086.

[51] Durand, J.-E., Raynaud, F., Lamet, J.-M., Tessé, L., Lestrade, J.-Y., and Anthoine, J., "Numerical Study of Fuel Regression in Hybrid Rocket Engine," *Joint Propulsion Conference*, 2018. https://doi.org/10.2514/6.2018-4593.

[52] Naka, G., Carmicino, C., Messineo, J., Kitagawa, K., and Shimada, T., "Evaluation of Radiative Heat-Transfer Effect on Paraffin-Wax Regression Rate in Hybrid Rocket," *Journal of Propulsion and Power*, Vol. 39, No. 2, 2023, pp. 258–273. https://doi.org/10.2514/1.B38728.

[53] Watson, G. H., and Lee, A. L., "Solid Rocket Booster Thermal Radiation Model," Tech. Rep. NASA CR-144300, NASA, 1976.

[54] Farmer, R. C., Smith, S. D., and Myruski, B. L., "Radiation from Advanced Solid Rocket Motor Plumes," Tech. Rep. NASA CR-196554, NASA, 1994.

[55] Baek, S. W., and Kim, M. Y., "Analysis of Radiative Heating of a Rocket Plume Base with the Finite-Volume Method," *International Journal of Heat and Mass Transfer*, Vol. 40, No. 7, 1997, pp. 1501–1508. https://doi.org/10.1016/S0017-9310(96)00257-8.

[56] Burt, J. M., and Boyd, I. D., "Monte Carlo Simulation of Particle Radiation in High Altitude Solid Rocket Plumes," *43rd AIAA/ASME/SAE/ASEE Joint Propulsion Conference & Exhibit*, 2007. https://doi.org/10.2514/6.2007-5703.

[57] Pearce, B. E., "Radiative Heat Transfer Within a Solid-Propellant Rocket Motor," *Journal of Spacecraft and Rockets*, Vol. 15, No. 2, 1978, pp. 125–128. https://doi.org/10.2514/3.28003.

[58] Der, J. J., and Nelson, D. A., "Internal Radiative Heating from Aluminum Oxide Particles in Solid Propellant Rocket Motors," *21st Joint Propulsion Conference*, 1985. https://doi.org/10.2514/6.1985-1397.

[59] Dombrovskii, L. A., "A Theoretical Investigation of Heat Transfer by Radiation Under Conditions of Two-Phase Flow in a Supersonic Nozzle," *High Temperature*, Vol. 34, No. 2, 1996, pp. 255–262.

[60] Duval, R., Soufiani, A., and Taine, J., "Coupled Radiation and Turbulent Multiphase Flow in an Aluminised Solid Propellant Rocket Engine," *Journal of Quantitative Spectroscopy and Radiative Transfer*, Vol. 84, No. 4, 2004, pp. 513–526. https://doi.org/10.1016/S0022-4073(03)00268-1.

[61] Jung, J.-Y., and Brewster, M. Q., "Radiative Heat Transfer Analysis with Molten Al_2O_3 Dispersion in Solid Rocket Motors," *Journal of Spacecraft and Rockets*, Vol. 45, No. 5, 2008, pp. 1021–1030. https://doi.org/10.2514/1.30018.

[62] Turchi, A., Bianchi, D., Thakre, P., Nasuti, F., and Yang, V., "Radiation and Roughness Effects on Nozzle Thermochemical Erosion in Solid Rocket Motors," *Journal of Propulsion and Power*, Vol. 30, No. 2, 2014, pp. 314–324. https://doi.org/10.2514/1.B34997.

[63] Bianchi, D., and Neri, A., "Numerical Simulation of Chemical Erosion in Vega Solid-Rocket-Motor Nozzles," *Journal of Propulsion and Power*, Vol. 34, No. 2, 2018, pp. 482–498. https://doi.org/10.2514/1.B36388.

[64] Dombrovsky, L. A., *Radiation Heat Transfer in Disperse Systems*, Begell House, New York, 1996.

[65] Cross, P. G., "Radiative Heat Transfer in Solid Rocket Nozzles," *Journal of Spacecraft and Rockets*, Vol. 57, No. 2, 2020, pp. 247–260. https://doi.org/10.2514/1.A34598.

[66] Hao, X., Zhang, H., Hou, X., and Tang, G., "Radiative properties of alumina/aluminum particles and influence on radiative heat transfer in solid

rocket motor," *Chinese Journal of Aeronautics*, Vol. 35, No. 2, 2022, pp. 98–116. https://doi.org/10.1016/j.cja.2021.05.024.

[67] Hao, X., Yan, Y., Cao, T., Li, W., and Zhang, H., "Numerical prediction of the two-phase flow and radiation effects on the thermal environment and ablation of solid rocket nozzle," *International Journal of Thermal Sciences*, Vol. 197, 2024, p. 108794. https://doi.org/10.1016/j.ijthermalsci.2023.108794.

[68] Geisler, R., Beckman, C., and Kinkhead, S., "The relationship between solid propellant formulation variables and motor performance," *11th Propulsion Conference*, 1975. https://doi.org/10.2514/6.1975-1199.

[69] Bityukov, V., and Petrov, V., "Absorption Coefficient of Molten Aluminum Oxide in Semitransparent Spectral Range," *Applied Physics Research*, Vol. 5, No. 1, 2013, pp. 51–62. https://doi.org/10.5539/apr.v5n1p51.

[70] Harrison, J., and Brewster, M. Q., "Simple model of thermal emission from burning aluminum in solid propellants," *Journal of Thermophysics and Heat Transfer*, Vol. 23, No. 3, 2009, pp. 630–634. https://doi.org/10.2514/1.39143.

[71] Allport, J. J., "Results of a Measurement of the Emissivity and Temperature of the Combustion Products in the Throat of a TM-3 End-Burning Motor," Tech. Rep. TM-33-61-U1, United Technology Corp., Sunnyvale, CA, 1961.

[72] Martin, H. T., Houim, R. W., Ferrara, P. J., Degges, M. J., Cortopassi, A. C., Boyer, J. E., and Kuo, K. K., "A Novel Radiative Heat Flux Measurement Technique for Combustion Products Flowing in Solid Rocket Nozzles," *International Journal of Energetic Materials and Chemical Propulsion*, Vol. 12, No. 3, 2013, pp. 183–196. https://doi.org/10.1615/IntJEnergeticMaterialsChemProp.v12.i3.

[73] Martin, H. T., Cortopassi, A. C., and Kuo, K. K., "Assessment of the Performance of Ablative Insulators Under Realistic Solid Rocket Motor Operating Conditions," *International Journal of Energetic Materials and Chemical Propulsion*, Vol. 16, No. 1, 2017, pp. 1–22. https://doi.org/10.1615/IntJEnergeticMaterialsChemProp.v16.i1.

[74] Gordon, S., and McBride, B. J., "Computer Program for Calculation of Complex Chemical Equilibrium Compositions and Applications," NASA RP-1311, Oct. 1994.

[75] Anderson, J. D., *Hypersonic and high–temperature gas dynamics*, 2nd ed., AIAA Education series, Reston, 2006.

[76] Spalart, P., and Allmaras, S., "A One-Equation Turbulence Model for Aerodynamic Flows," *AIAA*, Vol. 439, 1992. https://doi.org/10.2514/6.1992-439.

[77] Menter, F. R., "Two-Equation Eddy-Viscosity Turbulence Models for Engineering Applications," *AIAA Journal*, Vol. 32, No. 8, 1994, pp. 1598–1605. https://doi.org/10.2514/3.12149.

[78] Godunov, S. K., Zabrodin, A. V., Ivanov, M. I., Kraiko, A. N., and Prokopov, G. P., *Numerical solution of multidimensional problems of gas dynamics*, Izdatel'stvo Nauka, Moscow, 1976.

[79] Toro, E., "The HLLC Riemann solver," *Shock Waves*, Vol. 29, 2019, pp. 1065–1082. https://doi.org/10.1007/s00193-019-00912-4.

[80] Strang, G., "On the Construction and Comparison of Difference Schemes," *SIAM Journal on Numerical Analysis*, Vol. 5, No. 3, 1968, pp. 506–517. https://doi.org/10.1137/0705041.

[81] Brown, P. N., Byrne, G. D., and Hindmarsh, A. C., "VODE: A Variable-Coefficient ODE Solver," *SIAM J. Sci. Stat. Comput.*, Vol. 10, No. 5, 1989, p. 1038–1051.

[82] Betti, B., Pizzarelli, M., and Nasuti, F., "Coupled Heat Transfer Analysis in Regeneratively Cooled Thrust Chambers," *Journal of Propulsion and Power*, Vol. 30, No. 2, 2014, pp. 360–367. https://doi.org/10.2514/1.B34855.

[83] Bianchi, D., Nasuti, F., and Carmicino, C., "Hybrid Rockets with Axial Injector: Port Diameter Effect on Fuel Regression Rate," *Journal of Propulsion and Power*, Vol. 32, No. 4, 2016, pp. 984–996. https://doi.org/10.2514/1.B36000.

[84] Betti, B., Bianchi, D., Nasuti, F., and Martelli, E., "Chemical Reaction Effects on Heat Loads of CH_4/O_2 and H_2/O_2 Rockets," *AIAA Journal*, Vol. 54, No. 5, 2016, pp. 1693–1703. https://doi.org/10.2514/1.J054606.

[85] Leccese, G., Bianchi, D., Betti, B., Lentini, D., and Nasuti, F., "Convective and Radiative Wall Heat Transfer in Liquid Rocket Thrust Chambers," *Journal of Propulsion and Power*, Vol. 34, No. 2, 2018, pp. 318–326. https://doi.org/10.2514/1.B36589.

[86] Chiaverini, M. J., Harting, G. C., Lu, Y.-C., Kuo, K. K., Peretz, A., Jones, H. S., Wygle, B. S., and Arves, J. P., "Pyrolysis Behavior of Hybrid-Rocket Solid Fuels Under Rapid Heating Conditions," *Journal of Propulsion and Power*, Vol. 15, No. 6, 1999, pp. 888–895. https://doi.org/10.2514/2.5512.

[87] Bradley, D., Dixon-Lewis, G., din Habik, S. E., and Mushi, E., "The oxidation of graphite powder in flame reaction zones," *Symposium (International) on Combustion*, Vol. 20, No. 1, 1985, pp. 931 – 940. https://doi.org/https://doi.org/10.1016/S0082-0784(85)80582-8.

[88] Rotondi, M., Grossi, M., Migliorino, M. T., and Bianchi, D., "Role of Multi-phase Modeling on Nozzle Thermochemical Erosion in Solid Rocket Motors," *AIAA SCITECH Forum*, 2023. https://doi.org/10.2514/6.2023-0392.

[89] Marble, F. E., "Dynamics of a Gas Containing Small Solid Particles," *Combustion and Propulsion (5th AGARDograph Colloquium)*, 1963, pp. 175–213.

[90] Henderson, C. B., "Drag Coefficients of Spheres in Continuum and Rarefied Flows," *AIAA Journal*, Vol. 14, No. 6, 1976, pp. 707–708. https://doi.org/10.2514/3.61409.

[91] Kavanau, L. L., and Drake Jr, R., "Heat Transfer from Spheres to a Rarefied Gas in Subsonic Flow," Tech. rep., California University of Berkley, Institute of Engineering Research, 1953.

[92] Beji, T., Zhang, J. P., and and, M. D., "Determination of Soot Formation Rate from Laminar Smoke Point Measurements," *Combustion Science and Technology*, Vol. 180, No. 5, 2008, pp. 927–940. https://doi.org/10.1080/00102200801894398.

[93] Leung, K., Lindstedt, R., and Jones, W., "A simplified reaction mechanism for soot formation in nonpremixed flames," *Combustion and Flame*, Vol. 87, No. 3, 1991, pp. 289–305. https://doi.org/10.1016/0010-2180(91)90114-Q.

[94] Leccese, G., "Gas–Surface Interaction, Radiative Heat Transfer and Termochemistry Modeling in the Simulation of Paraffin–Based Hybrid Rocket Engines," *Ph.D Thesis in Aeronautics and Space Engineering*, Sapienza Università di Roma, 2017.

[95] Mazzoni, C. M., "Modelling of Thermal Radiation and Soot Emissions in Aerospace Applications," *Ph.D Thesis in Aeronautics and Space Technology*, Sapienza Università di Roma, 2011.

[96] Rothman, L., Gordon, I., Barber, R., Dothe, H., Gamache, R., Goldman, A., Perevalov, V., Tashkun, S., and Tennyson, J., "HITEMP, the High-Temperature Molecular Spectroscopic Database," *Journal of Quantitative Spectroscopy and Radiative Transfer*, Vol. 111, No. 15, 2010, pp. 2139–2150. https://doi.org/10.1016/j.jqsrt.2010.05.001.

[97] Alberti, M., Weber, R., and Mancini, M., "Re-creating Hottel's emissivity charts for carbon dioxide and extending them to 40bar pressure using HITEMP-2010 data base," *Combustion and Flame*, Vol. 162, No. 3, 2015, pp. 597–612. https://doi.org/10.1016/j.combustflame.2014.09.005.

[98] Tashkun, S., and Perevalov, V., "CDSD-4000: High-Resolution, High-Temperature Carbon Dioxide Spectroscopic Databank," *Journal of Quantitative Spectroscopy and Radiative Transfer*, Vol. 112, No. 9, 2011, pp. 1403–1410. https://doi.org/10.1016/j.jqsrt.2011.03.005.

[99] Ren, T., Han, Y., Modest, M. F., Fateev, A., and Clausen, S., "Evaluation of Spectral Line Mixing Models and the Effects on High Pressure Radiative Heat Transfer Calculations," *Journal of Quantitative Spectroscopy and Radiative Transfer*, Vol. 302, 2023. https://doi.org/10.1016/j.jqsrt.2023.108555.

[100] Pannier, E., and Laux, C., "RADIS: A Nonequilibrium Line-by-Line Radiative Code for CO2 and HITRAN-like Database Species," *Journal of Quantitative Spectroscopy and Radiative Transfer*, Vol. 222-223, 2019, pp. 12–25. https://doi.org/10.1016/j.jqsrt.2018.09.027.

[101] Rivière, P., and Soufiani, A., "Updated Band Model Parameters for H_2O, CO_2, CH_4 and CO Radiation at High Temperature," *International Journal*

of Heat and Mass Transfer, Vol. 55, No. 13, 2012, pp. 3349–3358. https://doi.org/10.1016/j.ijheatmasstransfer.2012.03.019.

[102] Krakow, B., Babrov, H. J., Maclay, G. J., and Shabott, A. L., "Use of the Curtis-Godson Approximation in Calculations of Radiant Heating by Inhomogeneous Hot Gases," *Applied Optics*, Vol. 5, No. 11, 1966. https://doi.org/10.1364/AO.5.001791.

[103] Modest, M. F., "The Weighted-Sum-of-Gray-Gases Model for Arbitrary Solution Methods in Radiative Transfer," *Journal of Heat Transfer*, Vol. 113, No. 3, 1991, pp. 650–656. https://doi.org/10.1115/1.2910614.

[104] Brent W. Webb, V. P. S., and André, F., "The Spectral Line Weighted-Sum-of-Gray-Gases (SLW) Model for Prediction of Radiative Transfer in Molecular Gases," *Advances in Heat Transfer*, Vol. 51, 2019, pp. 207–298. https://doi.org/10.1016/bs.aiht.2019.08.003.

[105] Pearson, J. T., Webb, B. W., Solovjov, V. P., and Ma, J., "Efficient Representation of the Absorption Line Blackbody Distribution Function for H2O, CO2, and CO at Variable Temperature, Mole Fraction, and Total Pressure," *Journal of Quantitative Spectroscopy and Radiative Transfer*, Vol. 138, 2014, pp. 82–96. https://doi.org/10.1016/j.jqsrt.2014.01.019.

[106] Edwards, D., "Molecular Gas Band Radiation," *Advances in Heat Transfer*, Vol. 12, 1976, pp. 115–193. https://doi.org/10.1016/S0065-2717(08)70163-1.

[107] Tien, C. L., and Drolen, B. L., "Thermal radiation in particulate media with dependent and independent scattering," *Annual Review of Numerical Fluid Mechanics and Heat Transfer*, Vol. 1, Hemisphere, New York, 1987, pp. 1–32.

[108] Dombrovsky, L. A., *Radiation Heat Transfer in Disperse Systems*, Begell House, New York, 1996.

[109] Bohren, C. F., and Huffman, D. R., *Absorption and Scattering of Light by Small Particles*, John Wiley & Sons, Ltd, New York, 1998.

[110] Ko, J. Y., Lee, E., and Kwon, S., "Influence of optical properties of alumina particles on the radiative base heating from solid rocket plume," *Advances in Space Research*, Vol. 64, No. 2, 2019, pp. 514–526. https://doi.org/10.1016/j.asr.2019.04.024.

[111] Reed, R., and Calia, V., "Review of Aluminum Oxide Rocket Exhaust Particles," AIAA Paper 1993-2819, 28th AIAA Thermophysics Conference, 1993.

[112] Liu, L., and Mishchenko, M. I., "Scattering and radiative properties of complex soot and soot-containing aggregate particles," *Journal of Quantitative Spectroscopy and Radiative Transfer*, Vol. 106, 2007, pp. 262–273.

[113] Sorensen, C. M., "Light scattering and absorption by fractal aggregates," *Journal of Quantitative Spectroscopy and Radiative Transfer*, Vol. 218, 2018, pp. 371–380. https://doi.org/10.1016/j.jqsrt.2018.06.015.

[114] Hsueh-chia, C., and T., C. T., "Determination of the wavelength dependence of refractive indices of flame soot," *Proc. R. Soc. Lond.*, 1990. https://doi.org/10.1098/rspa.1990.0107.

[115] Lockwood, F., and Shah, N., "A New Radiation Solution Method for Incorporation in General Combustion Prediction Procedures," *Symposium (International) on Combustion*, Vol. 18, No. 1, 1981, pp. 1405–1414. https://doi.org/10.1016/S0082-0784(81)80144-0.

[116] Shan, S., Qian, B., Zhou, Z., Wang, Z., and Cen, K., "New Pressurized WSGG Model and the Effect of Pressure on the Radiation Heat Transfer of H2O/CO2 Gas Mixtures," *International Journal of Heat and Mass Transfer*, Vol. 121, 2018, pp. 999–1010. https://doi.org/10.1016/j.ijheatmasstransfer.2018.01.079.

[117] Bordbar, H., Fraga, G. C., and Hostikka, S., "An Extended Weighted-Sum-of-Gray-Gases Model to Account for All CO2 - H2O Molar Fraction Ratios in Thermal Radiation," *International Communications in Heat and Mass Transfer*, Vol. 110, 2020. https://doi.org/10.1016/j.icheatmasstransfer.2019.104400.

[118] "User Manual of the ESPSS EcosimPro Libraries 3.6.0," ESA Study Contract Report, 2022.

[119] Ponomarenko, A., "RPA: Tool for Rocket Propulsion Analysis. Thermal Analysis of Thrust Chambers," Tech. rep., Rocket Propulsion Software+Engineering UG, 2012.

[120] Fiala, T., Sattelmayer, T., Gröning, S., Hardi, J., Stützer, R., Webster, S., and Oschwald, M., "Comparison Between Excited Hydroxyl Radical and Blue Radiation from Hydrogen Rocket Combustion," *Journal of Propulsion and Power*, Vol. 33, No. 2, 2017, pp. 490–500. https://doi.org/10.2514/1.B36280.

[121] Alberti, M., Weber, R., and Mancini, M., "Re-creating Hottel's emissivity charts for water vapor and extending them to 40 bar pressure using HITEMP-2010 data base," *Combustion and Flame*, Vol. 169, 2016, pp. 141–153. https://doi.org/10.1016/j.combustflame.2016.04.013.

[122] Barrere, M., Jaumotte, A., de Veubeke, B. F., and Vandenkerckhove, J., *Rocket Propulsion*, Elsevier Publishing Company, Amsterdam, The Netherlands, 1960.

[123] Höglauer, C., Kniesner, B., Knab, O., Kirchberger, C., Schlieben, G., and Kau, H.-P., "Simulation of a GOX–Kerosene Subscale Rocket Combustion Chamber," *CEAS Space Journal*, Vol. 2, 2011, pp. 31–40. https://doi.org/10.1007/s12567-011-0017-7.

[124] Arnold, R., Suslov, D. I., and Haidn, O. J., "Film Cooling in a High-Pressure Subscale Combustion Chamber," *Journal of Propulsion and Power*, Vol. 26, No. 3, 2010, pp. 428–438. https://doi.org/10.2514/1.47148.

[125] Leccese, G., Bianchi, D., Betti, B., Lentini, D., and Nasuti, F., "Convective and Radiative Wall Heat Transfer in Liquid Rocket Thrust Chambers," *Journal of Propulsion and Power*, Vol. 34, 2018, pp. 318–326. https://doi.org/10.2514/1.B36589.

[126] Concio, P., Migliorino, M. T., Bianchi, D., and Nasuti, F., "Numerical Estimation of Nozzle Throat Heat Flux in Oxygen-Methane Rocket Engines," *Journal of Propulsion and Power*, Vol. 39, No. 1, 2023, pp. 71–83. https://doi.org/10.2514/1.B38811.

[127] Migliorino, M. T., Cocirla, G., Fabiani, M., Grossi, M., Bianchi, D., and Nasuti, F., "Convective and Radiative Wall Heat Transfer Evaluation in Film-Cooled Liquid Rocket Thrust Chambers," *Proceedings of the 74th International Astronautical Congress*, Baku, Azerbaijan, 2023.

[128] Burkhardt, H., Sippel, M., Herbertz, A., and Klevanski, J., "Kerosene vs. Methane: A Propellant Tradeoff for Reusable Liquid Booster Stages," *Journal of Spacecraft and Rockets*, Vol. 41, No. 5, 2004, pp. 762–769. https://doi.org/10.2514/1.2672.

[129] Neill, T., Judd, D., Veith, E., and Rousar, D., "Practical Uses of Liquid Methane in Rocket Engine Applications," *Acta Astronautica*, Vol. 65, No. 5, 2009, pp. 696–705. https://doi.org/10.1016/j.actaastro.2009.01.052.

[130] Rudnykh, M., Carapellese, S., Liuzzi, D., Arione, L., Caggiano, G., Bellomi, P., D'Aversa, E., Pellegrini, R., Lobov, S., Gurtovoy, A., and Rachuk, V., "Development of LM10-MIRA LOX/LNG Expander Cycle Demonstrator Engine," *Acta Astronautica*, Vol. 126, 2016, pp. 364–374. https://doi.org/10.1016/j.actaastro.2016.04.018.

[131] Grossi, M., Sereno, A., Bianchi, D., and Nasuti, F., "Numerical Analysis of Methane-Oxygen Liquid Rocket Engine Nozzle Performance with Finite-Rate Chemical Kinetics," *Proceedings of the 9th Space Propulsion Conference*, Glasgow, Scotland, 2024.

[132] Silvestri, S., Celano, M. P., Schlieben, G., and Haidn, O. J., "Characterization of a Multi-Injector GOX/CH4 Combustion Chamber," *52nd AIAA/SAE/ASEE Joint Propulsion Conference*, 2016. https://doi.org/10.2514/6.2016-4992.

[133] Yu, K., Zhang, H., Liu, Y., and Liu, Y., "Study of normal spectral emissivity of copper during thermal oxidation at different temperatures and heating times," *International Journal of Heat and Mass Transfer*, Vol. 129, 2019, pp. 1066–1074. https://doi.org/10.1016/j.ijheatmasstransfer.2018.09.116.

[134] González-Fernández, L., del Campo, L., Pérez-Sáez, R., and Tello, M., "Normal spectral emittance of Inconel 718 aeronautical alloy coated with yttria stabilized zirconia films," *Journal of Alloys and Compounds*, Vol. 513, 2012, pp. 101–106. https://doi.org/10.1016/j.jallcom.2011.09.097.

[135] Carmicino, C., and Russo Sorge, A., "Experimental Investigation into the Effect of Solid-Fuel Additives on Hybrid Rocket Performance," *Journal of Propulsion and Power*, Vol. 31, No. 2, 2015, pp. 699–713. https://doi.org/10.2514/1.B35383.

[136] Ciottoli, P. P., Malpica Galassi, R., Lapenna, P. E., Leccese, G., Bianchi, D., Nasuti, F., Creta, F., and Valorani, M., "CSP-based chemical kinetics mechanisms simplification strategy for non-premixed combustion: An application to hybrid rocket propulsion," *Combustion and Flame*, Vol. 186, 2017, pp. 83–93. https://doi.org/j.combustflame.2017.07.035.

[137] Curran, H., Gaffuri, P., Pitz, W., and Westbrook, C., "A Comprehensive Modeling Study of n-Heptane Oxidation," *Combustion and Flame*, Vol. 114, No. 1, 1998, pp. 149–177. https://doi.org/10.1016/S0010-2180(97)00282-4.

[138] Linteris, G., Zammarano, M., Wilthan, B., and Hanssen, L., "Absorption and reflection of infrared radiation by polymers in fire-like environments," *Fire and Materials*, Vol. 36, No. 7, 2012, pp. 537–553. https://doi.org/10.1002/fam.1113.

[139] Lyon, R. E., and Janssens, M. L., "Polymer Flammabiliy," Tech. rep., U.S. Department of Transportation Federal Aviation Administration, 2005.

[140] Isbell, R. A., and Brewster, M. Q., "Optical Properties of Energetic Materials: RDX, HMX, AP, NC/NG, and HTPB," *Propellants, Explosives, Pyrotechnics*, Vol. 23, 1998, pp. 218–224.

[141] Ge, W., David, C., Modest, M. F., Sankaran, R., and Roy, S. P., "Comparison of spherical harmonics method and discrete ordinates method for radiative transfer in a turbulent jet flame," *Journal of Quantitative Spectroscopy and Radiative Transfer*, Vol. 296, 2023, p. 108459. https://doi.org/10.1016/j.jqsrt.2022.108459.

[142] Bendana, F. A., Sanders, I. C., Castillo, J. J., Hagström, C. G., Pineda, D. I., and Spearrin, R. M., "In-situ thermochemical analysis of hybrid rocket fuel oxidation via laser absorption tomography of CO, CO_2, and H_2O," *Experiments in Fluids*, Vol. 61, No. 9, 2020. https://doi.org/10.1007/s00348-020-03004-7.

[143] Ludwig, C. B., Malkmus, W., Reardon, J. E., Thomson, J. A. L., and Goulard, R., "Handbook of infrared radiation from combustion gases," Tech. rep., NASA SP 3080, 1973.

[144] Gordon, I. E., Rothman, L. S., Hargreaves, R. J., Hashemi, R., Karlovets, E. V., Skinner, F. M., Conway, E. K., Hill, C., Kochanov, R. V., Tan, Y., Wcisło, P., Finenko, A. A., Nelson, K., Bernath, P. F., Birk, M., Boudon, V., Campargue, A., Chance, K. V., Coustenis, A., Drouin, B. J., Flaud, J. M., Gamache, R. R., Hodges, J. T., Jacquemart, D., Mlawer, E. J., Nikitin, A. V., Perevalov, V. I., Rotger, M., Tennyson, J., Toon, G. C., Tran, H., Tyuterev, V. G., Adkins, E. M., Baker, A., Barbe, A., Canè, E., Császár, A. G., Dudaryonok, A., Egorov, O., Fleisher, A. J., Fleurbaey, H., Foltynowicz, A., Furtenbacher, T., Harrison, J. J., Hartmann, J. M., Horneman, V. M., Huang, X., Karman, T., Karns, J., Kassi, S., Kleiner, I., Kofman, V., Kwabia-Tchana, F., Lavrentieva, N. N., Lee, T. J., Long, D. A., Lukashevskaya, A. A., Lyulin, O. M., Makhnev, V. Y., Matt, W., Massie, S. T., Melosso, M., Mikhailenko, S. N., Mondelain, D., Müller, H. S., Naumenko, O. V., Perrin, A., Polyansky, O. L., Raddaoui, E., Raston, P. L., Reed, Z. D., Rey, M., Richard, C., Tóbiás, R., Sadiek, I., Schwenke,

D. W., Starikova, E., Sung, K., Tamassia, F., Tashkun, S. A., Auwera, J. V., Vasilenko, I. A., Vigasin, A. A., Villanueva, G. L., Vispoel, B., Wagner, G., Yachmenev, A., and Yurchenko, S. N., "The HITRAN2020 molecular spectroscopic database," *Journal of Quantitative Spectroscopy and Radiative Transfer*, Vol. 277, 2022. https://doi.org/10.1016/j.jqsrt.2021.107949.

[145] Fuss, S. P., and Hamins, A., "Determination of Planck Mean Absorption Coefficients for HBr, HCl, and HF," *Journal of Heat Transfer*, Vol. 124, No. 1, 2001, pp. 26–29. https://doi.org/10.1115/1.1416689.

[146] Carlotti, S., and Maggi, F., "Experimental techniques for characterization of particles in plumes of sub-scale solid rocket motors," *Acta Astronautica*, Vol. 186, 2021, pp. 496–507. https://doi.org/10.1016/j.actaastro.2021.06.011.

[147] Kirshenbaum, A., and Cahill, J., "The density of liquid aluminium oxide," *Journal of Inorganic and Nuclear Chemistry*, Vol. 14, No. 3, 1960, pp. 283–287. https://doi.org/10.1016/0022-1902(60)80272-2.

[148] Arnold, J., Dodson, J., and Laub, B., "Subscale Solid Motor Nozzle Tests (Phase IV), and Nozzle Materials Screening and Thermal Characterization (Phase V)," Tech. rep., NASA CR 161254, 1979.

[149] Selçuk, N., "Exact Solutions for Radiative Heat Transfer in Box-Shaped Furnaces," *ASME Journal of Heat Transfer*, Vol. 107, No. 3, 1985, pp. 648–655. https://doi.org/10.1115/1.3247473.

[150] Chai, J., Parthasarathy, G., Lee, H. S., and Patankar, S. V., "Finite volume radiative heat transfer procedure for irregular geometries," *Journal of Thermophysics and Heat Transfer*, Vol. 9, No. 3, 1995, pp. 410–415. https://doi.org/10.2514/3.682.

[151] Dua, S. S., and Ping, C., "Multi-Dimensional Radiative Transfer in Non-Isothermal Cylindrical Media with Non-Isothermal Bounding Walls," *International Journal of Heat and Mass Transfer*, Vol. 18, No. 2, 1975, pp. 245–259. https://doi.org/10.1016/0017-9310(75)90157-X.

[152] Modest, M. F., and Azad, F. H., "The Differential Approximation for Radiative Transfer in an Emitting, Absorbing and Anisotropically Scattering Medium," *Journal of Quantitative Spectroscopy and Radiative Transfer*, Vol. 23, No. 1, 1980, pp. 117–120. https://doi.org/10.1016/S0022-4073(80)80010-0.